2014

# Toward Polymer Coating with Easy Ice Release

Chenyu Wang
*Virginia Commonwealth University*

# Toward Polymer Coatings with Easy Ice Release

A dissertation submitted in partial fulfillment of the requirements for the degree of
Doctor of Philosophy at Virginia Commonwealth University.

by

Chenyu Wang

B.S. (2008), Nanjing University of Science and Technology, China.

M.S. (2011). Virginia Commonwealth University, USA

Director: Dr. Kenneth J. Wynne

Professor, Department of Chemical and Life Science Engineering

Virginia Commonwealth University

Richmond, Virginia

August 2014

# ACKNOWLEDGEMENT

I would like to express my deepest gratitude and thanks to my advisor, Dr. Kenneth J. Wynne, for his guidance, support and patience. His wisdom, encouragement and enthusiasm have deeply changed my future. I would like to thank Dr. Wei Zhang, who gave me the trainings on experiments and instruments hand by hand. His suggestions and comments are important and valuable for this project. I would also like to thank my committee members for their time and valuable suggestions.

This project would never have been possible without the support from my family. I would like to thank my parents and grandparent for their unconditional love and support. Finally, to my loving and supportive wife, Qian: my deepest gratitude. Your encouragement helped me to persevere through the tough phase of my life.

# TABLE OF CONTENTS

**Chapter 1.** General Instroduction: Toward Polymer Coatings with Easy Ice Release

**Chapter 2.** Rigid Adherent-Resistant Elastomer (RARE) and Epoxied Cylinder (EC) test

**Chapter 3.** A laboratory test for ice adhesion strength using commercial instrumentation

**Chapter 4.** Thickness dependence and modeling of ice removal stress for a polydimethysiloxane nanocomposite: Sylgard 184

**Chapter 5.** Conclusions

**Chapter 6.** Further Exploration

# LIST OF FIGURES

# LIST OF SCHEMES

# LIST OF TABLES

# ABSTRACT

Toward Polymer Coatings with Easy Ice Release

By Chenyu Wang, Ph.D.

A dissertation submitted in partial fulfillment of the requirement for the degree of Doctor of Philosophy, Engineering at Virginia Commonwealth University

Virginia Commonwealth University, 2014

Major Director: Dr. Kenneth J. Wynne, Professor, Department of Chemical and Life Science Engineering

Minimizing adhesion of ice has been the subject of extensive studies for applications such aircraft wings, wind turbine blades spacecraft, power transmission wires, while a growing interest concerns coatings for aerospace applications. The work described here describes progress for coatings and ice release test method development over the last few years. Major achievements include: (1) New Rigid Adherent-Resistant Elastomers (RARE), (2) A new Epoxied Cylinder (EC) adhesion test, (3) Validation of an ice release test, and (4) Study of ice adhesion strength on coating thickness for a PDMS elastomer.

Rigid Adhesion-Resistance Elastomers (RARE) are comprised of 3F **1** terminated with triethoxysilane moieties and linear 3F polyurethane (U-3F). Hybrid compositions U-3F-x are designated by polyurethane weight percent “x”. Interestingly, RARE coatings spontaneously “self-stratify” during coating deposition and cure. Cured RARE coatings are comprised of (1) a nanoscale surface layer with low work of adhesion, (2) a low modulus mesoscale and (3) a tough U-3F bulk, where “Mesoscale” is defined as a near surface region with a depth ~ 1000 nm.

An EC adhesion test was developed to evaluate the fouling release characteristics of RARE. EC adhesion testing was devised by using the commercially available instrument, TA RSA-3. The TA RSA-3 is well suited for these tests as the 3.5 kg load cell facilitates accurate measurements. This test gives *peak* force ($P_s$) for EC removal. A striking compositional dependence was found for EC adhesion. A U-3F-50 hybrid coating had the lowest adhesion ($P_s$ = 0.078 MPa) with good toughness (6.2 MPa). Bulk and surface characterization together with adhesion measurements established U-3F-x hybrid coatings, and U-3F-50 in particular, as new fluorous rigid adherent-resistant elastomers (RARE) that are tough, oil resistant, and optically transparent.

Inspired by the Epoxied Cylinder (EC) adhesion test, a laboratory method for ice adhesion measurement with a commercially available instrument was established in the Wynne Laboratory. This is the first laboratory ice adhesion test that does not require a custom built apparatus. The temperature controlled chamber on TA RSA-3 is an enabling feature that is essential for the test. The method involves removal of an ice cylinder from a polymer coating with a probe and the determination of peak removal force ($P_s$). To validate the test method, the strength of ice adhesion was determined for a prototypical glassy polymer, poly(methyl methacrylate). The distance of the probe from the PMMA surface has been identified as a critical variable for $P_s$. The new test provides a readily available platform for investigating fundamental surface characteristics affecting ice adhesion. In addition to the ice release test, PMMA coatings were characterized using DSC, DCA and TM-AFM.

This new laboratory ice release test was then employed to obtain the thickness dependence of ice adhesion for Sylgard 184, a filled polydimethylsiloxane elastomer. A correlation between ice adhesion and coating thickness (t) was found, that follows a relationship developed by Kendall over 40 years ago for removal of a rigid object from an elastomer. In particular, a nearly linear relationship between peak removal stress ($P_s$) and $1/t^{1/2}$ was found, with $P_s$ decreasing from 550 kPa to 100 kPa with coating thickness increasing from 12 μm to 800 μm. While work of adhesion, which is related to surface free energy, is recognized as an important factor that can affect ice release, the results reported herein show that coating thickness can override this single parameter for elastomeric substrates. Base on the result, a general model is proposed for the removal of ice from low modulus elastomers (~10 MPa).

# CHAPTER 1

# General Introduction: Toward Polymer Coatings with Easy Ice Release

## 1.1. Overall statement

Minimizing adhesion of ice has been the subject of studies for applications such as aircraft wings, wind turbine blades, spacecraft and power transmission wires. The major purpose of this investigation is 1) to develop polymer coatings with low work of adhesion and strong mechanical property, and 2) to validate an ice release test using a commercially available instrument.

A stumbling block to development of ice release coatings has been the absence of a straightforward laboratory based test for easily measuring the removal force for ice release. Inspired by the Epoxied Cylinder (EC) test development for Rigid Adherent-Resistant Elastomer (RARE) work, a laboratory method for ice adhesion measurement with a commercially available instrument was established in the Wynne Laboratory. A TA Instruments TA RSA-3, which is customarily used for dynamic mechanical analysis (DMA), has been adapted for ice release testing. This new test provides a readily available platform for investigating fundamental surface characteristics affecting ice adhesion. To validate the new method further, investigations were proposed for the glassy polymer, poly(methyl methacrylate) (PMMA) and a commercially available polydimethylsiloxane (PDMS) elastomer, Sylgard 184. Exploration of the following variables on ice adhesion was proposed: temperature, probe distance, coating thickness and roughness.

## 1.2. Scope of study.

### *1.2.1. Rigid Adherent-Resistant Elastomers (RARE) and Epoxied Cylinder (EC) Adhesion test*

An EC adhesion test was developed to evaluate the fouling release characteristics of Rigid Adhesion-Resistance Elastomers (RARE).[2] RARE coatings are comprised of 3F **1** terminated with triethoxysilane moieties and linear 3F polyurethane (U-3F). Hybrid compositions U-3F-x are designated by polyurethane weight percent "x". Interestingly, RARE coatings spontaneously "self-stratify" during coating deposition and cure. Cured RARE coatings are comprised of (1) a nanoscale surface layer with low work of adhesion, (2) a low modulus mesoscale and (3) a tough U-3F bulk, where "Mesoscale" is defined as a near surface region with a depth ~ 1000 nm.[2]

EC adhesion testing was devised by using the commercially available instrument, TA RSA-3. The TA RSA-3 is well suited for these tests as the 3.5 kg load cell facilitates accurate measurements. This test gives *peak* force ($P_s$) for EC removal. To our knowledge, $P_s$ measurements with the TA RSA-3 are the first utilizing a commercial instrument. Prior measurements have been obtained with manual gauges[3] or custom built devices.[4-6] A striking compositional dependence was found for EC adhesion. A U-3F-50 hybrid coating had the lowest adhesion ($P_s$ = 0.078 MPa) with good toughness (6.2 MPa). Bulk and surface characterization together with adhesion measurements established U-3F-x hybrid coatings, and U-3F-50 in particular, as new fluorous rigid adherent-resistant elastomers (RARE) that are tough, oil resistant, and optically transparent.

### *1.2.2. Ice release test*

A laboratory test method for evaluating ice adhesion was developed employing TA RSA-3 for the Epoxied Cylinder (EC) Adhesion test,. This is the first laboratory ice adhesion test that does not require a custom built apparatus. The temperature controlled chamber is an enabling feature essential for the test. The method involves removal of an ice cylinder from a polymer coating with a probe and the determination of peak removal force ($P_s$). To validate the test method, the strength of ice adhesion was determined for a prototypical glassy polymer, poly(methyl methacrylate) and a commercially available elastomeric silicone, Sylgard 184. For PMMA, the distance of the probe from the PMMA surface and surface roughness have been identified as two critical variables. In contrast, coating thickness has been found as the most significant parameter in the ice release test for Sylgard 184. The new test provides a readily available platform for investigating fundamental surface characteristics affecting ice adhesion.

# CHAPTER 2

# Rigid Adherent-Resistant Elastomers (RARE) and Epoxied Cylinder (EC) test

## 2.1. Introduction

Minimizing adhesion of unwanted adherents has been the subject of a great deal of research and development because “self-cleaning” is of great value for architectural, biomedical, marine, aerospace, aquaculture, and energy-intense applications. Adherents run the gamut from soft species such as proteins,[7] bacteria,[8] and human cells[9] to those of high rigidity such as marine organisms (e. g. barnacles, oysters) and ice. The focus of this paper is *rigid* adherents on elastomeric coatings, and specifically on coatings that resist adhesion by rigid adhesives and / or objects. Such coatings are designated RARE, for *rigid adherent-resistant elastomers*. The noun “adherent” is used to avoid confusion with the separate matter of the coating itself adhering to a substrate.

RARE coatings provide easy release provided that geometric constraints such as mechanical locking are absent. The designation foul release has been used in reference to unwanted marine fouling,[10-13] but this term is broadly applied to soft and hard adhering organisms and does not specify the physical state of the adherent. RARE coatings are narrowly defined and include the remarkable hybrid coatings described herein.

Silicone coatings, that is, those based on polydimethylsiloxane (PDMS) are arguably archetypical RAREs. Owen has published several articles addressing the surface properties of PDMS coatings that facilitate release of bonded objects,[14-16] including “Why Silicones Behave

Funny".[17] PDMS coatings have intrinsic shortcomings that have driven continued RARE research. Similar solubility parameters for PDMS and hydrocarbons result in swelling by oil and fuels. Weak interchain interactions give rise to poor mechanical properties that include poor abrasion and tear resistance.[18]

Fluoropolymers are both oleophobic and hydrophobic but often require special processing.[19] Fluoropolymers with $C_8F$ and $C_{10}F$ side chains confer resistance to adhesion due to formation of ordered domains with $–CF_3$ groups at the outermost surface.[20] However, coatings containing $C_8F$ and $C_{10}F$ inevitably degrade to perfluorooctanoic acid (PFOA) which is bioaccumulative.[21-22] As a result, there is virtually no possibility for translation to applications for polymers and materials containing $C_8F$ and $C_{10}F$ moieties.[23-24]

The development of alternative environmentally responsible RAREs has recently focused on structures employing short fluorous side chains such as fluorous polyoxetanes[25-27] or fluoroalkyl-aromatic acrylates and methacrylates.[28] Coatings based on acrylate copolymer networks incorporating acrylate perfluoropolyether (PFPE) side chains are interesting and effective alternatives, although costly.[29]

Surfaces having six or less perfluorinated moieties [$-CF_3$, ($C_1F$), $-C_2F_5$ ($C_2F$), etc.] have sessile drop contact angles of ~ 110° suggesting low surface energies similar to $C_8F$ and $C_{10}F$ analogs. However, Chaudhury has noted that adhesion does not correlate with advancing contact angles, but follows contact angle hysteresis, $\theta_{\Delta} = \theta_{adv} - \theta_{rec}$.[30-31] That is, adhesion increases as $\theta_{rec}$ decreases. Receding contact angles reflect the tendency of a wetted surface to reconstruct in response to interfacial forces.[32] Similar enthalpically driven surface reorganizations are expected to increase the strength of interfacial bonding for polar adherents. Receding contact angles for polymers containing shorter fluorous side chains are typically

~60°.[33-34] Thus, generating fluorous side-chain polymers for RARE coatings based on relatively economical alcohols with $C_nF$, $n \leq 6$) presents a challenge for minimizing interfacial interactions.

In addition to physical and chemical bonding, mechanical properties have an important role in fracture of adhesive bonds to elastomers. These contributions have been summarized by Kim.[35] A relationship developed by Kendall (Eq 1) relates elastomer modulus and thickness to adhesion, where $P_c$ is the critical pull off force normal to the substrate, a is the radius of the circular adhesive bond, t is thickness, $w_a$ is work of adhesion, and $K$ is elastomer modulus.[36]

$$P_c = \pi a^2 \left( \frac{2 w_a K}{t} \right)^{1/2} \qquad \text{Eq. 1}$$

If $w_a$ is constant, the Kendall criteria for detachment of a rigid cylinder bonded to an elastomeric substrate provides a qualitative sense for the importance of modulus. If two coatings differ only by one having twice the modulus of the other, Eq 1 predicts that $P_c$ increases by 1.4 when the coating modulus doubles.[37] Considering only thickness, $P_c$ decreases by 0.7 when coating thickness doubles. In short, adhesion by a rigid object to a RARE coating is minimized by increasing thickness and decreasing modulus.

The relationship of increasing adhesion strength with decreasing thickness was demonstrated by Singer for PDMS coatings.[38-39] Based on prior studies,[38-39] the interrelationship of adhesion to both modulus and surface energy was addressed by Brady and Singer.[10] A plot of relative adhesion versus $(\gamma K)^{-1/2}$, where $\gamma$ is surface energy, resulted in a linear relationship in accord with Eq 1. Emphasizing the importance of mechanical properties in a different way for a model silicone coating, Kim found that as crosslink density (modulus) increased, more force was required to detach a rigid object (constant thickness).[35]

From the above, mechanical properties, coating thickness and surface energy contribute to minimizing adhesion of rigid objects. Herein, a novel hybrid blend is described using precursors for a fluorous hybrid siliceous *chemical network* (CN) and a linear fluorous polyurethane that forms a *physical network* (PN). Scheme 2.1 describes blends that are prepared from **3**, trialkoxysilyl end capped 3F, BTESE **4**, and linear polyurethane **6** (U-3F). The preparation of U-3F-$SiO_{1.5}$ hybrid elastomers (Scheme 2.1) is related to polymer-$SiO_2$ hybrids reported by Saegusa and Chujo 20 years ago.[40] More recently, using a double miniemulsion polymerization, Zhang prepared hybrid hollow/bowl-type $SiO_2$/PMMA microparticles.[41] Li described the reaction of 3-aminopropyltriethoxysilane (APS) with isocyanates as a facile route to simultaneously introduce components into epoxies that improved thermal stability (siliceous domain) and toughness (second polymer).[42-43] Thus, there is an interesting range of novel hybrids that combine antipodal siliceous and organic components in a way that results in novel compositions and morphologies.

Bulk characterization of the new U-3F-$SiO_{1.5}$ hybrid elastomers provides a relationship of toughness to blend composition. Surface characterization by ATR-IR spectroscopy reveals near surface compositional enrichment for the hybrid blend component. Evidence suggests that near surface depletion of the U-3F polyurethane contributes to low adhesion strength for a rigid adherent, viz., an epoxied aluminum cylinder (EC). To describe the length scale for near surface enrichment, the term *mesosurface* is introduced, which in this context is a depth of ~1000 nm. Mesosurface is distinguished from *nanosurface*, the outermost layer ≤ 1 nm.

The work described herein is the first to suggest a mesosurface contribution to adhesion of rigid objects. The combination of nanosurface, mesosurface and bulk characteristics for hybrid blends provides insight into relationships determining force and energy required for removing a rigid object from the surface. Finally, although EC adhesion tests have been widely reported in the context of marine biofouling with custom built devices,[3,35,44-46] broadened and more basic possibilities are provided by an innovative test method using a commercially available instrument.

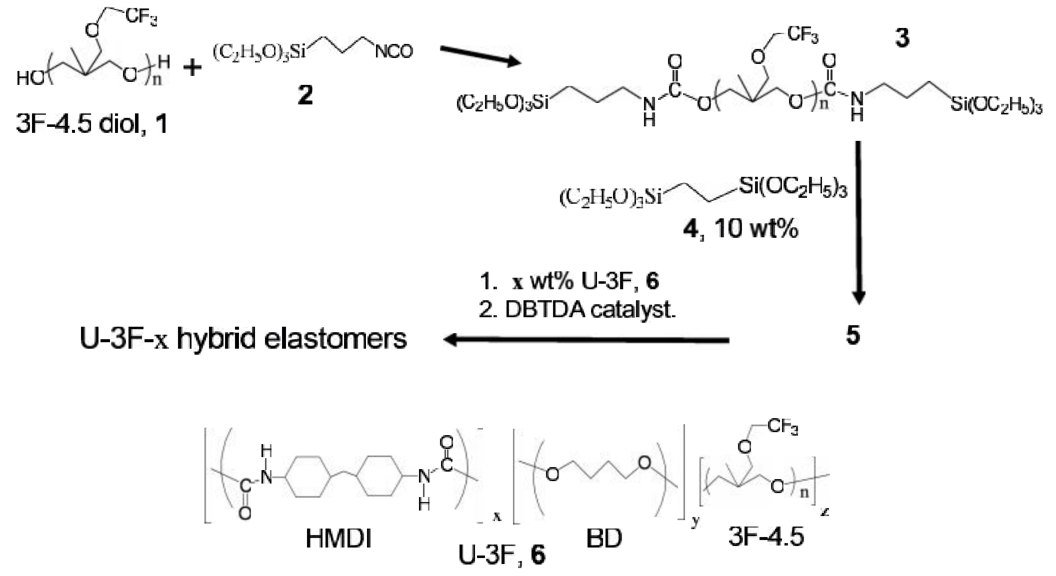

**Scheme 2.1.** Preparation of U-3F-x hybrid elastomers, where x = wt % U-3F.

## 2.2. Experimental

**2.2.1. Materials**. PolyFOx, PF 6320, that is, poly(3-(2,2,2-trifluoroethoxymethyl)-3-methyloxetane) that is designated herein as “3F diol” was a generous gift from OMNOVA Solutions, Akron OH. 3-Isocyanatopropyltriethoxysilane (SII 6456) and bis(triethoxysilyl)ethane, SIB1817, “BTESE” were purchased from Gelest, Inc. Dibutyltin diacetate (DBTDA) and 4,4’-methylenebis-(cyclohexylisocyanate), HMDI, were purchased from Aldrich. 1,4-Butanediol, 99+% and tetrahydrofuran, 99.6%, (for analysis ACS, stabilized with BHT) were from Acros.

### 2.2.2. Preparative procedures.

As received PolyFOx, PF 6320 was purified by liquid-liquid extraction according to a recently published method.[47] In brief, as received as received PF 6320 diol was extracted 8-10 times with hexane to yield 3F-4.5 (concentrated in bottom layer); GPC (THF), $M_n$ = 4.5 kD, PDI = 1.26.

*2.2.2.1. 3F precursor **3**.* 3F-4.5 diol **1** is end capped with 3-isocyanatopropyl triethoxysilane **2** (Scheme 2.1). In a typical reaction, 10 g THF and 0.2 g 3-isocyanatopropyl triethoxysilane **2** were combined in a 250 mL reaction vessel with DBTDA catalyst (0.5 wt%). 3F polyol **1** (2 g) was added slowly under a dry nitrogen purge. The reactants were held at 40 ºC for ~1-2 d. Completion was signaled by disappearance of the isocyanate IR absorption at 2200 $cm^{-1}$. To generate precursor solution **5**, BTESE **4** (10 wt%, ~ 1.0 ml) was added. Addition of **4** served to increase the volume fraction of siliceous domain in the hybrid elastomers (*vida infra*).

<u>*2.2.2.2. U-3F-x Hybrids.*</u> A THF solution of U-3F **6** was added to aliquots of precursor solution **5** to generate hybrid compositions with increasing U-3F wt %. After U-3F addition, stirring was continued for 30 min to obtain a homogenous solution and to achieve simultaneously an increase in viscosity from hydrolysis / condensation polymerization. Reactant masses for **3**, **4** and **6** are listed in Table 2.1. Compositions are shown based on feed wt% U-3F and wt% U-3F in the cured hybrid elastomer. Designations are based on the latter. The preparation of U-3F-50 is described in Supplemental Information.

### 2.2.3. Instrumentation and Testing.

<u>*2.2.3.1. Mechanical testing.*</u> For tensile testing, rectangular samples were stamped from cast plaques. After thickness, width and gauge (mm) measurements, samples were clamped into the holder of a TA Instruments RSA-3. The sample elongation rate was 0.05 mm/sec with a data acquisition rate of 1 Hz (24 °C). The modulus of elasticity was determined from the initial portion of the stress strain curve. Strain to break was noted, provided that sample extension did not exceed the instrument limits.

Dynamical mechanical and tensile mechanical properties were determined using a TA instruments RSA-3 employing the dynamic mechanical analyzer (DMA) mode. During analysis temperature was ramped from -90 to 150 $^{o}$C at 5 $^{o}$C/min while tension cycles were 1 Hz with maximum strain of 0.05%. Maximum autotension and autotension rate were 2 mm and 0.01 mm/s, respectively.

<u>*2.2.3.2. Differential Scanning Calorimetry*</u>**.** Modulated DSC (MDSC) utilized a TA-Q 1000 Series$^{TM}$ instrument (TA Instruments) with modulation amplitude of ± 0.5 °C, modulation period of 20 sec. Standard samples of zinc, tin and lead were used for energy and

temperature calibration. Samples (5-15 mg) were equilibrated at -90 °C followed by a heating ramp of 6 °C/min to 150 °C followed by a cooling ramp of 10 °C/min back to -90 °C and second heating cycle of 6 °C/min to 150 °C. Two consecutive heating cycles were also followed to observe any changes with heat treatment. A pre-run sample was also heated at 100 °C to mimic the curing conditions for 24 hr and then kept at ambient for another 24 hr. The same heating-cooling-heating cycles were followed to study thermal transitions.

*2.2.3.3. Infrared spectroscopy.* A Nicolet 400 spectrometer equipped with a Thunderdome accessory (Ge crystal) was used for acquiring carbonyl peak areas. Spectra were analyzed using Omnic software.

A Thermo Scientific Nicolet iS10 spectrometer equipped with a Smart iTR attachment was used for ATR-IR spectra with a diamond crystal. Spectra were analyzed using Omnic software. Difficulties associated with acquisition of spectra are described in the Supplemental Information. In brief, the crystal in the Nicolet iS10-iTR attachment is positioned beneath the plane of the crystal holder. For compositions having ≤ 40 wt% U-3F, the area in contact with the crystal was white after the coated slide was removed (Figure S2.1). The white appearance is attributed to compressive microfracturing that resulted from stress on the sample imposed by the pressure screw. Peak areas for ≤ 40 wt% U-3F are uncertain and reported as open squares, while peak those for compositions with ≥ 50 wt% U-3F are reported as filled circles in Figure 2.10.

*2.2.3.4. Tapping Mode Atomic Force Microscopy (AFM).* A Dimension Nanoscope V (Veeco, CA) atomic force microscope was used for topological and morphological analysis in tapping mode using silicon crystal cantilevers (40 N/m). Imaging was done at soft and hard tapping by changing the setpoint ratio $r_{sp}$ or $A_{exp}/A_o$ from 0.95 to 0.8, where $A_o$ is free oscillation amplitude and $A_{exp}$ is the experimental oscillation amplitude. Images with 50, 10 and 2 μm scans were taken to probe microscale and nanoscale morphology.

*2.2.3.5. Wetting Behavior***.** Wetting characteristics were determined by dynamic contact angle measurements (DCA, Wilhelmy plate) with a Cahn model 312 instrument. Deionised water was used as the probe liquid with an immersion/withdrawal rate of 100 μm/s. Reported contact angles are averages (typically ± 2°) of several force-distance cycles.

Static contact angles and image profiles were obtained by using a Ramé-Hart goniometer equipped with a camera. Contact angles were calculated using Drop Image software (version 1.4.11). The reported value is an average of 3 drops and 5 readings per drop.

*2.2.3.6. Swelling.* Oleophobicity was investigated by immersing a microscope slide with two representative U-3F-x coatings in hexadecane for 24 hr. To determine mass uptake, each slide was weighed before and after immersion. For comparison, a condensation cured PDMS coating was prepared from polydimethylsiloxane diol (4.2 kDa) cured with bis(triethoxysilyl)ethane (10 wt%).

*2.2.3.7. Adhesion testing.* An adhesion test was devised paralleling that developed by Swain,[44] used by Gatenholm[45] and refined by Chisholm[46]. This test is done by a probe that is parallel to the coating surface and is related to a test where a tensile removal force is applied perpendicular to the surface[4,38-39]

An aluminum cylinder (d =10 mm, h = 20 mm) was bonded to a fully cured, coated glass slide with an epoxy resin adhesive (Loctite Epoxy, marine, white, Henke Corporation, Rocky Hill, CT, USA). This adhesive, recommended by the manufacturer for marine applications, suggests a working time of 5 min and a complete cure time of 24 hr. After spreading a thin epoxy coating on the end of the cylinder, it was placed upright on a coated slide and lightly pressed into place. In less than 1 min, three such cylinders were put in place on a single coated glass slide. The epoxy was allowed to cure for a minimum of 24 hr at ambient temperature.

A holder for glass microscope slides (1 x 25 x 75 mm) was fabricated and installed in a TA RSA-3 Dynamic Mechanical Analyzer (TA instruments) as shown in Figure 2.1. Care was taken to insure that the microscope slide position was parallel to the force probe. The TA RSA-3 has a load cell with a 3.5 kg maximum. Consequently, this adhesion test is not applicable to strongly bonded objects. Coated slides with epoxied aluminum cylinders, designated ECs, were clamped into the fixture and the probe speed (shear rate) was set to 3 mm/min (50 µm/sec). Peak removal stress ($P_{C\text{-}S}$) was determined along with removal energy (RE), which is the area under the curve.

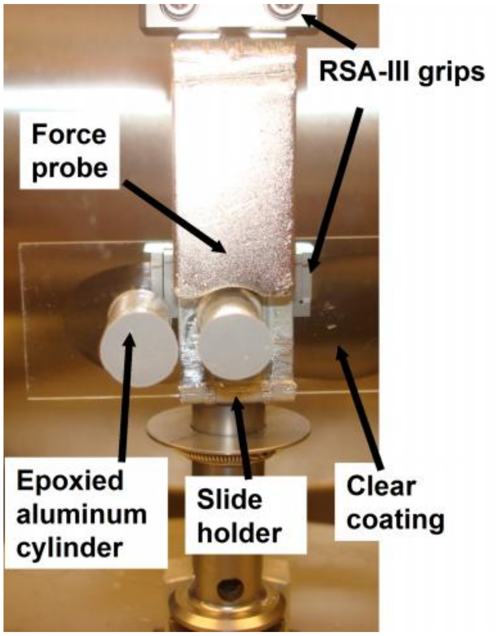

**Figure 2.1.** Coated slide with two epoxied aluminum cylinders for TA RSA-3 adhesion test.

## 2.3. Results

The procedure for generating hybrid elastomeric coatings is summarized followed by characterization of bulk mechanical properties. Surface characterization includes ATR-IR spectroscopy utilizing Ge and diamond crystals, AFM imaging, and contact angle measurements. Results from adhesion tests are correlated with nanosurface, mesosurface and bulk characterization.

### 2.3.1. Hybrid elastomer preparation

Scheme 2.1 describes the preparative route for U-3F-x hybrid elastomers, where “x” is the weight percent linear polyurethane U-3F. The components are (1) a fluorous polyoxetane end-capped with -$Si(OCH_2CH_5)_3$ combined with bis(triethoxysilyl)ethane (BTESE), both of which undergo hydrolysis / condensation cure and (2) linear fluorous polyurethane **6**. Feed and compositions for U-3F hybrid blends are provided in Table 2.1.

*2.3.1.1. 3F-End capping.* Following an approach described by Saegusa and Chujo,[48-49] reactive precursor **3** was prepared from 3F diol **1** and isocyanate **2** at ~50 °C in THF (Scheme 2.1). Common to all hybrid coatings, the reaction of 3F diol **1** and isocyanate **2** is carried out under nitrogen purge to prevent premature alkoxide hydrolysis.

Urethane end capping was monitored by IR spectroscopy (Figure S2.2).[50-51] The spectrum for **1** (Figure S2.2B) has a broad peak at 3500 $cm^{-1}$ characteristic of terminal O-H for the 3F diol. The spectrum for end capper **2** has a peak at 2200 $cm^{-1}$ confirming the presence of isocyanate (Figure S2.2A).[52] The spectrum at time (t = 0) after mixing **1** and **2** has the expected OH and NCO peaks (Figure S2.2C). The IR spectrum after 24 hr (Figure S2.2D) shows the absence of NCO and OH and the presence of amide NH (3300 $cm^{-1}$) expected for **3**.[50-51]

*2.3.1.2. U-3F.* The preparation of HMDI/BD(30)-3F-4.5 (30 wt% hard block) designated U-3F, used a conventional soft-block-first method described previously.[47] Briefly, 3F diol was purified by liquid-liquid extraction with hexane to remove cyclics and low molar mass species,[47] thereby ensuring high molecular weight for maximum mechanical properties and removing contaminants that confound contact angle determinations.[53] GPC $M_w$ for U-3F is 110 kDa; tensile strength and strain at break are 10.5 MPa and 1245 %, respectively (Table 2.2). U-3F dip-coated coverslips were used for dynamic contact angle (DCA) measurements (DCA, Wilhelmy plate). Contact angles were stable for 4 cycles with no water contamination in a post-DCA water check (Table 2.2).[47,53]

*2.3.1.3. Hybrid coatings.* Preliminary experiments demonstrated that the siliceous weight fraction from hydrolysis / condensation of -$Si(OC_2H_5)_3$ end caps was insufficient to stabilize wetting behavior for the 3F nanosurface. That is, contact angles changed ~10º over the course of 60 sec. Introducing 10 wt% 1,2-bis(hexaethoxysilyl)ethane, BTESE, **4** to generate precursor solution **5** (Scheme 2.1) increased the wt% siliceous domain and provided stable contact angles (*vida infra*). BTESE has been used in the preparation of porous oxycarbosilane spin-on low dielectric thin films[54-56] but not as a precursor for hybrids. The choice of BTESE for increasing the wt% CN was based on experiments that demonstrated negligible volatilization during cure (b.p. 119 °C) and adequate hydrolysis / condensation reactivity. For BTESE, $Si_2(CH_2)_2O_3$ is the nominal composition after hydrolysis / condensation (Eq 3). For brevity, the hydrolysis / condensation cure composition, which includes the contribution from 3F chain ends, is designated “siliceous” and represented as “-$SiO_{1.5}$”.

$$Si_2(CH_2)_2(OEt)_6 + 3H_2O \rightarrow Si_2(CH_2)_2O_3 + 6\ C_2H_5OH \qquad \text{Eq 3.}$$

After end group functionalization to form **5**, co-hydrolysis / co-condensation polymerization was initiated by terminating the nitrogen purge. Polyurethane **6**, U-3F, was added to aliquots of precursor solution **5**. Solutions were stirred for 30 min to initiate crosslinking and build viscosity prior to dip or drip coating and casting. As a control, a crosslinked hybrid coating was made without addition of polyurethane U-3F. This composition is designated 3F-$SiO_{1.5}$.

After cure in air (25 /100 ºC), U-3F-x hybrid coatings formed with x = 10, 30, 40, 50, 60, 75 and 90 wt% **6** (Table 2.1). The designations are based on the U-3F wt% in the coating after hydrolysis / condensation cure of 3F-$SiO_{1.5}$ precursors. Coating appearance ranged from clear to slightly hazy; an image for U-3F-50 is shown in Figure 2.2. Coatings on microscope slides were immersed in water for several days without delaminating. Good adhesion to glass and aluminum is attributed to bonding of intermediates in the hydrolysis / condensation of silicon alkoxides with surface –OH groups.

**Table 2.1.** Feed and composition for U-3F hybrid blends.

| Designation | Feed (g)[a] | | | U-3F wt%[b] | U-3F wt%[c] | $3F\text{-}SiO_{1.5}$ hybrid constituents (wt%) | | |
|---|---|---|---|---|---|---|---|---|
| | **3** | **4** | U-3F **6** (g)[a] | | | 3F | End group[d] | $Si_2C_2H_4O_3$ |
| $3F\text{-}SiO_{1.5}$ | | | 0 | | 0 | 91 | 5.5 | 3.6 |
| U-3F-10 | 2 | 0.2 | 0.22 | 9 | 10 | 82 | 4.9 | 3.2 |
| U-3F-30 | 2.2 | 0.22 | 0.94 | 28 | 30.1 | 64 | 3.8 | 2.5 |
| U-3F-40 | 2.2 | 0.22 | 1.46 | 38 | 40.1 | 54 | 3.3 | 2.1 |
| U-3F-50 | 2.2 | 0.22 | 2.2 | 48 | 50.2 | 45 | 2.7 | 1.8 |
| U-3F-60 | 2.2 | 0.22 | 3.3 | 58 | 60.2 | 36 | 2.2 | 1.4 |
| U-3F-75 | 2 | 0.2 | 6 | 73 | 75.1 | 23 | 1.4 | 0.9 |
| U-3F-90 | 2.2 | 0.22 | 19.8 | 89 | 90.1 | 9.1 | 0.5 | 0.4 |
| U-3F | - | - | - | 100 | 100 | 0 | 0 | 0 |

a. Sufficient THF for solution.
b. Based on feed.
c. Based on mass of U-3F in coating
d. End group = $(O\text{-}C(O)NH(CH_2)_3SiO_{1.5}$
e. From BTESE

**Figure 2.2.** Image of a U-3F-50 coating on a microscope slide.

### 2.3.2. Bulk Characterization

*2.3.2.1. Mechanical Properties.* 3F-$SiO_{1.5}$ and U-3F-10 samples were easily fractured precluding tensile mechanical property measurements. The threshold for obtaining measurements was U-3F-30, which had a strain-to-break of ~ 47% (Figure 2.3, Table 2.2). Increasing U-3F to U-3F-40 resulted in a jump to 235%. A steady increase in strain-to-break was found for hybrid compositions with increasing wt% U-3F (Figure 2.4). A lower limit for strain-at- break is shown for U-3F-75 and U-3F-90 because, for the initial gap distance selected, an instrument strain limit was reached.

The high strain-at-break for U-3F-75 and U-3F-90 may be compared to neat U-3F,[47] which did not break up to the TA RSA-3 limit >1200 % (Table 2.2). The U-3F-90 modulus (9.8 MPa) is only slightly reduced compared to U-3F (10.5 MPa), but a drop in modulus to 2.3 MPa is seen for U-3F-75. The modulus for U-3F-40 to U-3F-60 is in the 2-4 MPa range, but strain-to-break decreases with decreasing U-3F content.

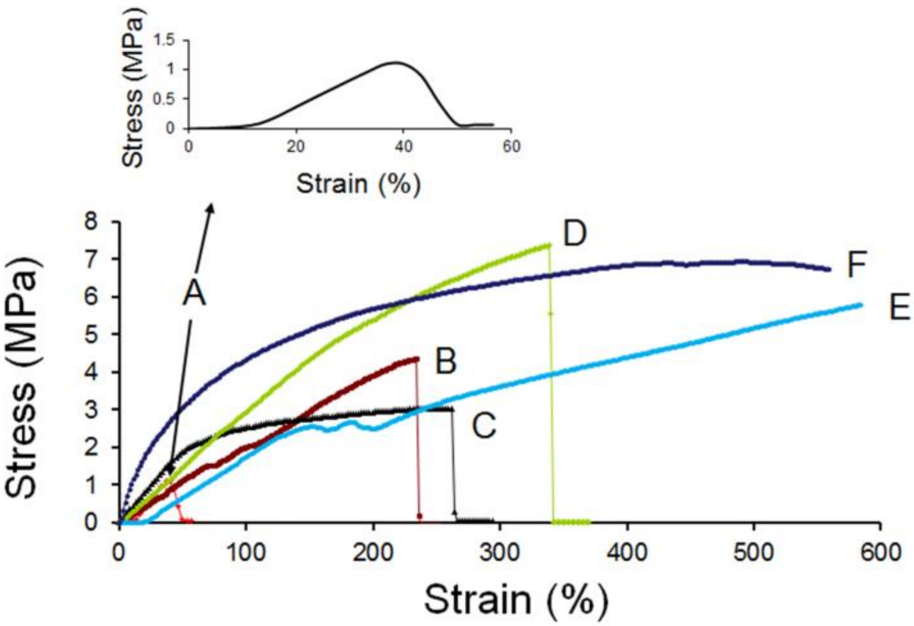

**Figure 2.3.** Stress-strain curves for U-3F-x: A, 30; B, 40; C, 50; D, 60; E, 75; F, 90.

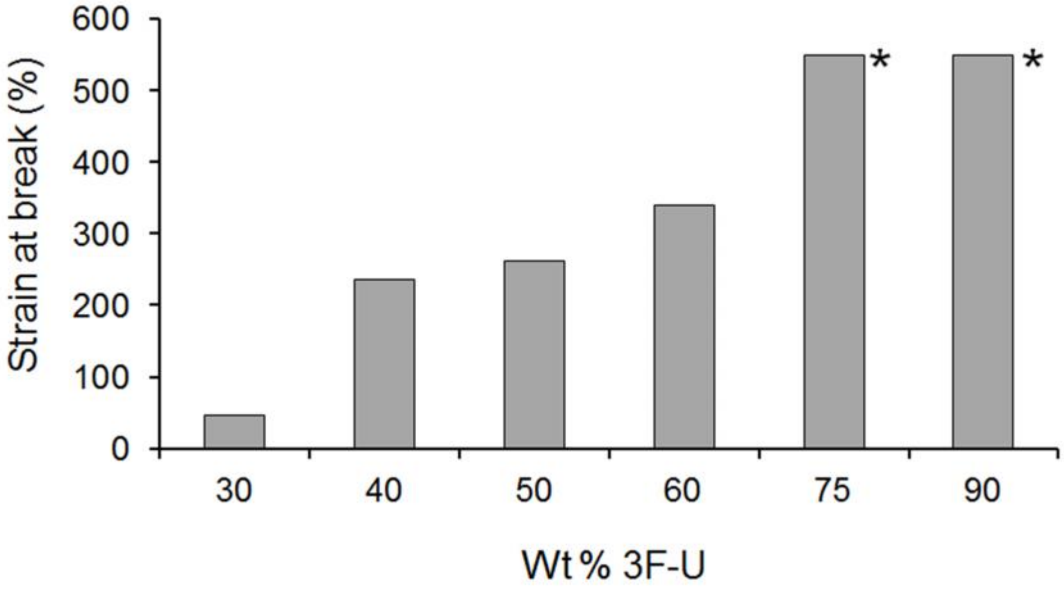

**Figure 2.4.** Strain-at-break for U-3F hybrids vs. wt% U-3F (***** exceeds limits, see text).

**Table 2.2.** Hybrid coatings: DSC transition temperatures, tensile testing and dynamic mechanical data.

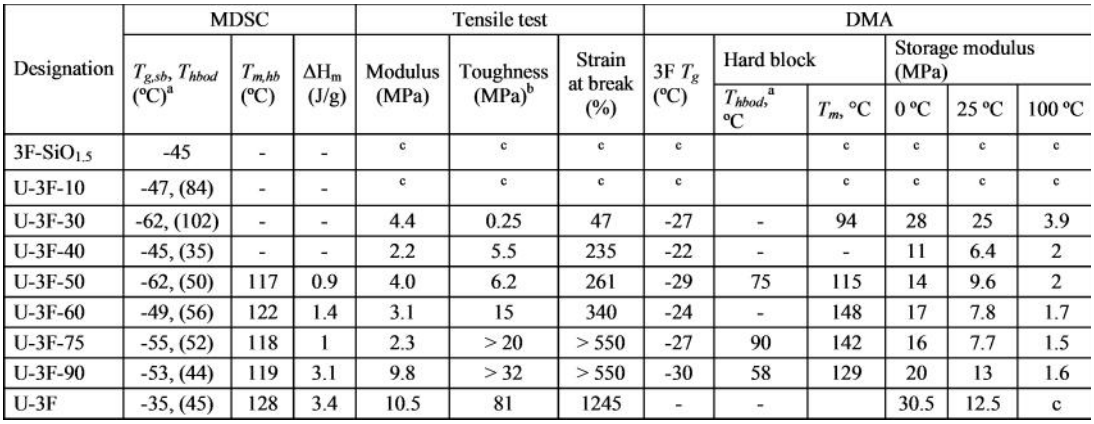

| Designation | MDSC | | | Tensile test | | | DMA | | | | | |
|---|---|---|---|---|---|---|---|---|---|---|---|---|
| | $T_{g,sb}$, $T_{hbod}$ (°C)[a] | $T_{m,hb}$ (°C) | $\Delta H_m$ (J/g) | Modulus (MPa) | Toughness (MPa)[b] | Strain at break (%) | 3F $T_g$ (°C) | Hard block | | Storage modulus (MPa) | | |
| | | | | | | | | $T_{hbod}$,[a] °C | $T_m$, °C | 0 °C | 25 °C | 100 °C |
| 3F-SiO$_{1.5}$ | -45 | - | - | [c] | [c] | [c] | [c] | | [c] | [c] | [c] | [c] |
| U-3F-10 | -47, (84) | - | - | [c] | [c] | [c] | [c] | | [c] | [c] | [c] | [c] |
| U-3F-30 | -62, (102) | - | - | 4.4 | 0.25 | 47 | -27 | - | 94 | 28 | 25 | 3.9 |
| U-3F-40 | -45, (35) | - | - | 2.2 | 5.5 | 235 | -22 | - | - | 11 | 6.4 | 2 |
| U-3F-50 | -62, (50) | 117 | 0.9 | 4.0 | 6.2 | 261 | -29 | 75 | 115 | 14 | 9.6 | 2 |
| U-3F-60 | -49, (56) | 122 | 1.4 | 3.1 | 15 | 340 | -24 | - | 148 | 17 | 7.8 | 1.7 |
| U-3F-75 | -55, (52) | 118 | 1 | 2.3 | > 20 | > 550 | -27 | 90 | 142 | 16 | 7.7 | 1.5 |
| U-3F-90 | -53, (44) | 119 | 3.1 | 9.8 | > 32 | > 550 | -30 | 58 | 129 | 20 | 13 | 1.6 |
| U-3F | -35, (45) | 128 | 3.4 | 10.5 | 81 | 1245 | - | - | | 30.5 | 12.5 | c |

a. Values in parentheses are small changes in slope that are reproducible; these do not necessarily correspond to increases in tan δ; both are assigned to hard block order disorder transitions, $T_{\text{hbod}}$.
b. Area under the stress strain curve; lower limit is cited if strain at break exceeded instrument limits.
c. Too fragile for stress-strain tests.
d. Sample softened and distorted precluding determination (Figure 2.5 C).

2.3.2.2. *Dynamic Mechanical Analysis.* DMA was carried out to examine phase transitions and to probe retention of mechanical properties as a function of temperature. Again, 3F-$SiO_{1.5}$ and U-3F-10 samples were too fragile for testing. Table 2.2 lists transition temperatures and storage modulus (MPa) at 0, 25 and 100 ºC. Below $T_g$ U-3F-x hybrids have storage moduli of ~ $10^{10}$ Pa. The 3F $T_g$ is -40 to -50 ºC depending on composition (Table 2.1); $T_g$'s for the 3F domains in 3F-$SiO_{1.5}$ and 3F-U are apparently coincident. Above the 3F $T_g$ storage moduli decrease ~100 fold over a 40 ºC interval. The onset of a long rubbery plateau with a storage modulus of ~ $10^6$ Pa begins at 0 ºC.

Figure 2.5 shows DMA for U-3F-40, U-3F-50 and U-3F. U-3F-40 has a broad storage modulus plateau that gradually decreases from 10 to 150 °C. For U-3F-50 a prominent decrease in E' and E'' and increase in tan δ at 115 °C is assigned to hard block $T_m$. A weak, broad transition at ~75 °C is designated $T_{hbod}$ for "hard block order-disorder" transition. Such a transition might involve H-bonding of hard block to the siliceous domain or hard block domains that have a low degree of order due to constraints imposed by the siliceous network. Further work is needed to clarify the nature of sub-$T_m$ hard block transitions. In any event, above the $T_{hbod}$ transition E' for U-3F-50 drops by another order of magnitude.

DMA for U-3F is shown in Figure 2.5C and serves as a reference. U-3F has a 3F soft block $T_g$ at -18 °C (-32 °C by DSC[47]). In contrast to U-3F hybrids, U-3F becomes dimensionally unstable at ~50 ºC, which is characterized by widely scattered data points as the auto-tension sensor seeks to maintain constant strain. This temperature corresponds to a change in slope in DSC (~ 45 ºC) that is assigned to a hard block order-disorder transition ($T_{hbod}$). Softening, which prevents determination of hard block $T_m$ by DMA, is typical for linear polyurethanes such as HMDI-PDMS polyureas.[57-58] In contrast, the dimensional stability that makes possible the observation of hard block $T_m$ for U-3F-50 is attributed to support by the 3F-$SiO_{1.5}$ network. As noted above, 3F-$SiO_{1.5}$ and U-3F-10 are too fragile to permit mechanical property measurements. However, at modest DMA strains, hybrids with ≥ 30 wt% U-3F have sufficient mechanical properties to provide adequate network support for U-3F.

DMA for the remaining U-3F-x hybrids and 3F-$SiO_{1.5}$ are in Supporting Information (Figures S2.4 and S2.5). Given DMA for U-3F-50, a similar result might be expected for compositions with increased U-3F content. This expectation is not met, as different results are seen for U-3F-60 and U-3F-75, while DMA for U-3F-90 is similar to U-3F-50. Observations are briefly summarized below:

- U-3F-60 (Table 2.2, Figure S2.4) has gradual decreases for E' and E'' and an accompanying increase in tan δ above ~ 75 °C, but there are no discrete transitions.
- U-3F-75 (Table 2.2, Figure S2.5) appears to have a weak disordered hard block transition $T_{hbod}$ (90 ºC) not well distinguished from $T_m$ (142 ºC).
- DMA for U-3F-90 (Figure S2.5, Table 2.2) is similar to U-3F-50 with a modest increase in tan δ assigned to $T_{hbod}$ (58 ºC) and a pronounced $T_m$ (129 ºC).

The presence of a crystalline or highly ordered hard block phase is clear from DSC results presented next, but $\Delta H_f$ are 1-3 J/g indicating that the volume fraction is small. DMA transitions for hybrids with 50% or greater U-3F content at > 50 °C suggest that this small hard block fraction is easily disrupted with the formation of disorganized hard block domains.

U-3F physical network (PN) formation is likely impeded by "network constrained phase separation" due to the chemical network (CN) produced by hydrolysis / condensation during solid formation. This constraint was proposed to explain trends in bulk morphology for a PDMS-3F-PDMS hybrid triblock copolymer.[59] For U-3F hybrids, a "stock solution" of end group functionalized 3F-4.5 and BTESE is prepared. U-3F is added to aliquots of this solution to generate U-3F-x precursor **5** (Scheme 2.1). As hydrolysis / condensation cure proceeds over the course of the coating process, the viscosity of the precursor solution increases during coating cover slips or slides. Plaques were prepared last by pouring remaining precursor solutions into Petri dishes. Because it was not feasible to simultaneously coat all compositions, condensation cure was likely more advanced in some solutions than others. Thus, U-3F hard block phase separation would be more constrained in coatings prepared from solutions where viscosity was high, that is, where network formation was more advanced. Different initial coating viscosities could explain inconsistencies in morphological development as the time-to-coating and casting were not controlled. This hypothesis awaits further investigations including elucidation of bulk morphology.

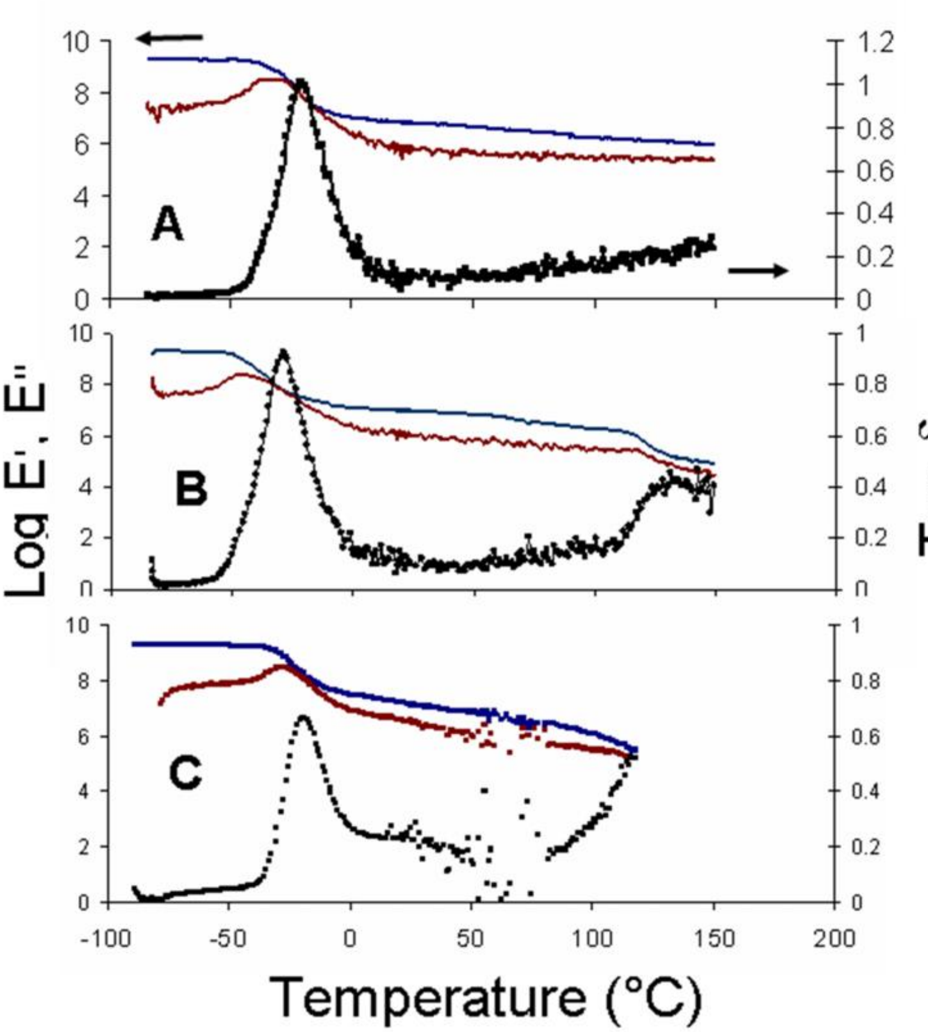

**Figure 2.5.** DMA for: **A**, U-3F-40; **B**, U-3F-50; and **C**, U-3F.

*2.3.2.3. Differential Scanning Calorimetry.* Figure 2.6 shows MDSC thermograms for U-3F, 3F-$SiO_{1.5}$ and U-3F hybrids. 3F-$SiO_{1.5}$ has a 3F $T_g$ at -45 ºC that is nearly identical to that for the 3F diol (-47 °C).[51,60] U-3F has a 3F soft block $T_g$ at -35 ºC, a disordered hard block transition $T_{hbod}$ at 45 °C and a hard block $T_m$ at 128 ºC with $\Delta H_f$ = 3.9 J/g. The 3F $T_g$ for U-3F is just 12 °C above that for the 3F diol indicating good hard block-soft block phase separation.[60]

U-3F-50 was the composition with minimum U-3F wt% for detecting a hard block $T_m$ by dynamic mechanical analysis. However, the threshold for detecting $T_m$ by MDSC was U-3F-30. Small endotherms for U-3F-30 and U-3F-40 $T_{hbod}$'s are not apparent in Figure 2.6 but are listed in Table 2.2.

For most U-3F-x hybrids with x ≥ 30, $T_m$ is ~ 10 °C lower than U-3F (Table 2.1). Figure 2.7 shows calculated $\Delta H_f$ based on U-3F wt% versus that found for U-3F hybrids. Hard block $\Delta H_f$ is consistently lower than that calculated assuming a linear extrapolation based on U-3F wt%. This finding is consistent with the systematically lower hybrid modulus noted above.

Of particular interest (*vida infra*), $\Delta H_f$ for U-3F-50 (1.4 J/g) is 28% below that calculated ($1.9_5$ J/g) based on $\Delta H_f$ for U-3F (3.9 J/g). The lower $\Delta H_f$ found for U-3F-50 compared to that calculated provides additional evidence for 3F-$SiO_{1.5}$ network constraint of hard block phase separation / crystallization. While hard block $\Delta H_f$ is reduced for all U-3F-x hybrids compared to calculated values, the reduction is not systematic (Figure 2.7). This is attributed to different degrees of hydrolysis / condensation cure for the precursor solutions noted above. However, particularly high percent reductions relative to calculated $\Delta H_f$ are seen for U-3F-30 (91%) and U-3F-40 (74%), which have 70 and 60 wt% 3F-$SiO_{1.5}$, respectively.

Changes in slope are observed in most U-3F hybrids thermograms with several at ~ 50 °C (Table 2.1). These transitions do not correlate with DMA $T_{\mathrm{hbod}}$'s. The origins are assigned to hard block order-disorder transitions $T_{\mathrm{hbod}}$, but as noted above, the origins remain unclear at present.

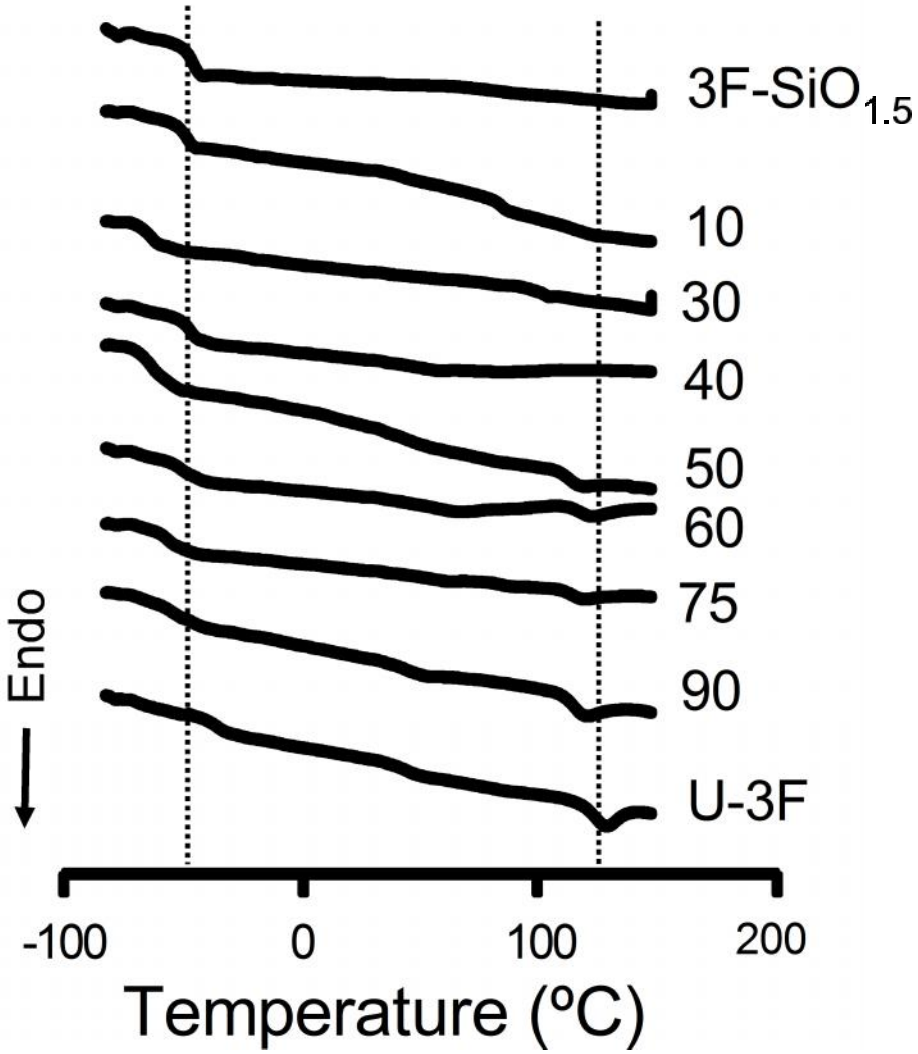

**Figure 2.6.** DSC thermograms for 3F-SiO$_{1.5}$, U-3F-x hybrids, and U-3F. Dotted lines are for guiding the eye.

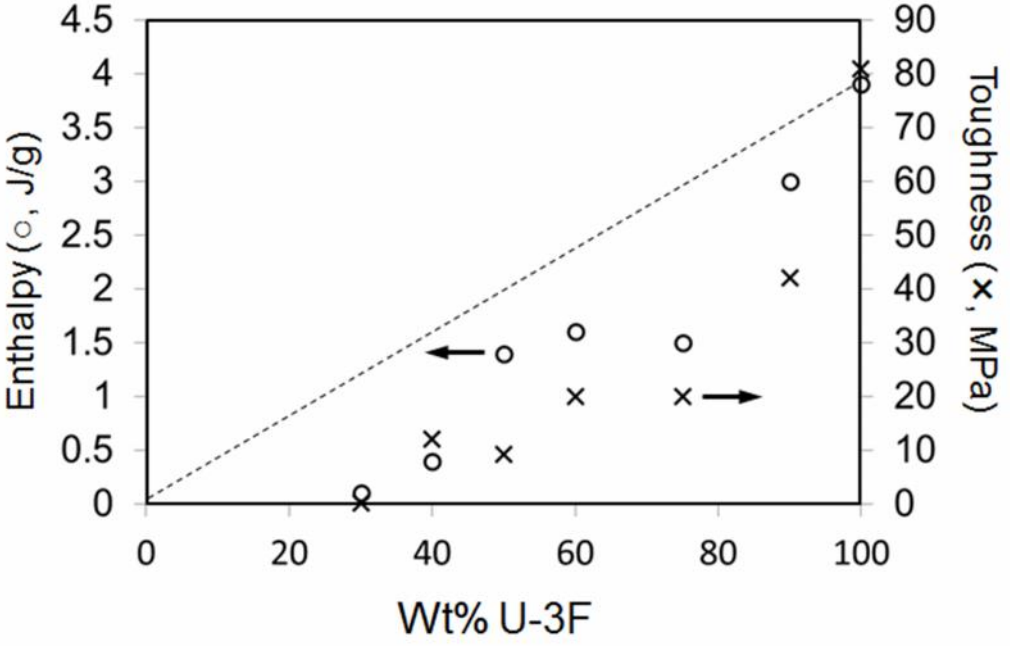

**Figure 2.7.** Calculated (-----) vs. observed (○) hard block $\Delta H_f$ for U-3F-x hybrids and U-3F and area under the stress strain curve (toughness, ×).

### 2.3.3. Surface Characterization.

*2.3.3.1. ATR-IR Spectroscopy*. U-3F. Analysis of spectra in the carbonyl region provides a correlation of hydrogen bonding with mechanical properties.[61] Two or three carbonyl absorptions occur for polyurethanes between 1600 - 1750 $cm^{-1}$.[61-63] A high frequency peak (1725 $cm^{-1}$) is assigned to "free" carbonyls while lower frequency peaks are due to carbonyls with "disordered" (~1700 $cm^{-1}$) or "ordered" (~1684 $cm^{-1}$) H-bonding [62].

Three absorptions are seen in the carbonyl region for U-3F (Figure 2.8). The highest intensity absorption is at 1695 $cm^{-1}$ (Figure 2.8). This strong "disordered H-bonded" peak correlates with good phase separation (DSC) and mechanical properties (tensile modulus 10.5 MPa).[61] The higher frequency shoulder at 1710 $cm^{-1}$ is assigned to "free" carbonyls. The lowest frequency peak (1665 $cm^{-1}$) may be associated with a region of more highly ordered H-bonded carbonyls.

Attenuated total reflection infrared (ATR-IR) spectroscopy provides vibrational spectra to a depth that depends on the crystal employed, the incident angle of IR radiation and the wavelength of the vibrational mode.[64-65] Bergbreiter applied ATR-IR to analysis of polyethylene / poly(ethylene glycol) block co-oligomer blends and demonstrated a depth dependent surface enrichment of the PE-PEG oligomer.[66] Gardella also employed ATR-IR to study polymer blends, including a study that demonstrated PMMA surface enrichment occurs in PMMA/PVC blends.[67]

In view of prior applications of ATR-IR spectroscopy to the study of near surface blend composition, spectra for the hybrid blends were investigated. The ATR-IR spectrum for U-3F-50 is provided in Figure S2.3 (3500 – 500 $cm^{-1}$). Multiple C-H peaks (~ 2900 $cm^{-1}$) and a broad N-H peak (~ 3316 $cm^{-1}$) are observed. A prominent peak at ~ 1290 $cm^{-1}$ is assigned to C-F stretch ($CF_3$, 3F side chains).[68] Carbonyl absorptions for the U-3F component are attenuated but otherwise identical to those discussed above.

The multicomponent nature of the hybrid coatings led to an examination of ATR-IR spectra in the 1200 – 1800 $cm^{-1}$ region so that peak area analysis would avoid problems due to multiple absorptions at selected frequencies (Figure 2.9). The spectra include (1) 3F-4.5 polyoxetane diol, (2) HMDI-BD prepared from a 1:1 ratio of isocyanate and butane diol, (3) the product of BTESE hydrolysis / condensation cure, viz., $Si_2(CH_2)_2O_{1.5}$, (4) U-3F polyurethane, (5) U-3F-50 and (6) 3F-$SiO_{1.5}$. Inspection of Figure 2.10 shows that the carbonyl region is free from interfering absorptions due to components other than U-3F. The weak carbonyl absorption for 3F-$SiO_{1.5}$ is discussed further below.

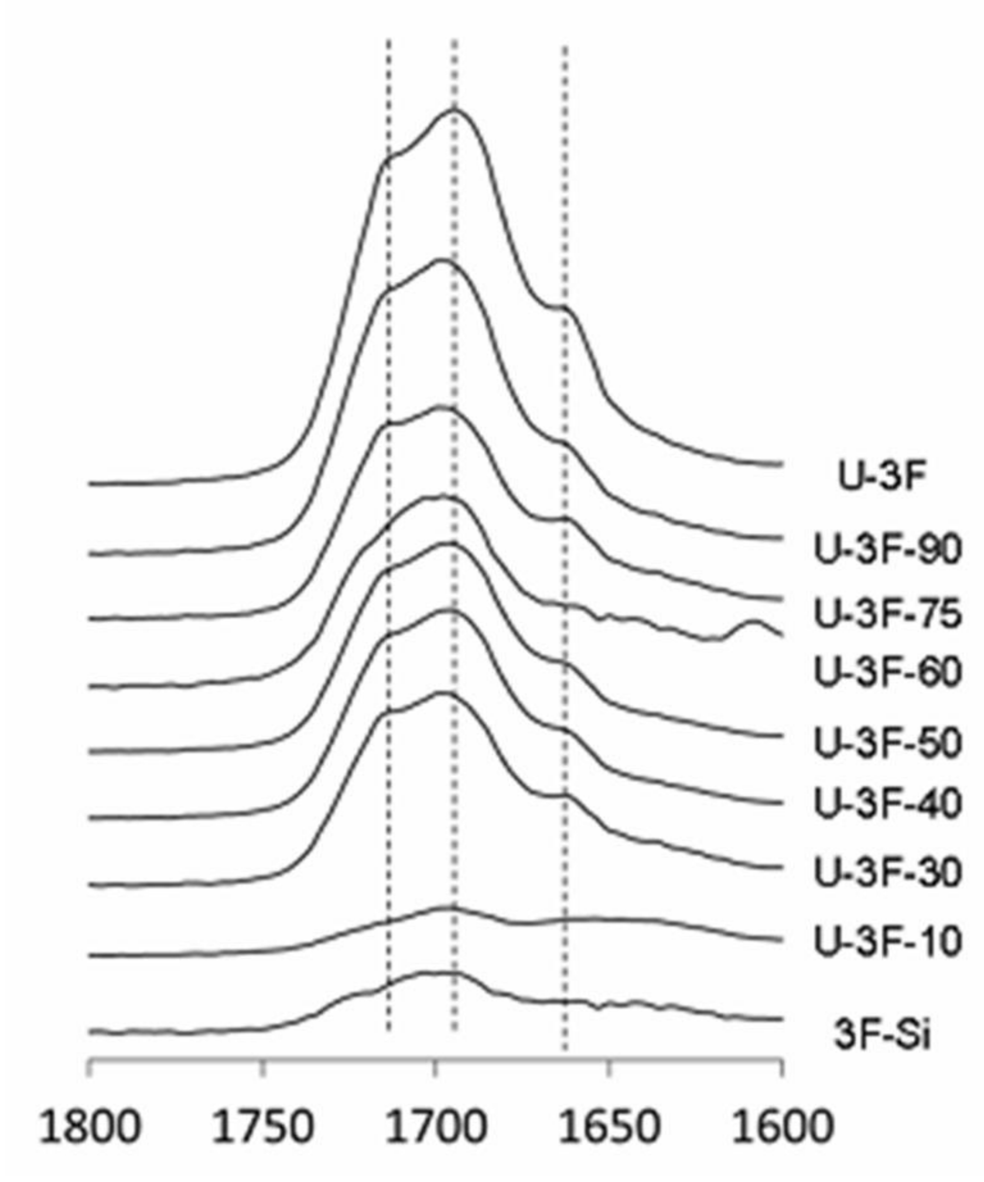

**Figure 2.8.** Carbonyl peaks for U-3F, 3F-$SiO_{1.5}$ and U-3F-x hybrid elastomers (diamond crystal). Three peaks are at about 1710, 1695, and 1665 $cm^{-1}$. Dotted lines are meant to guide the eye.

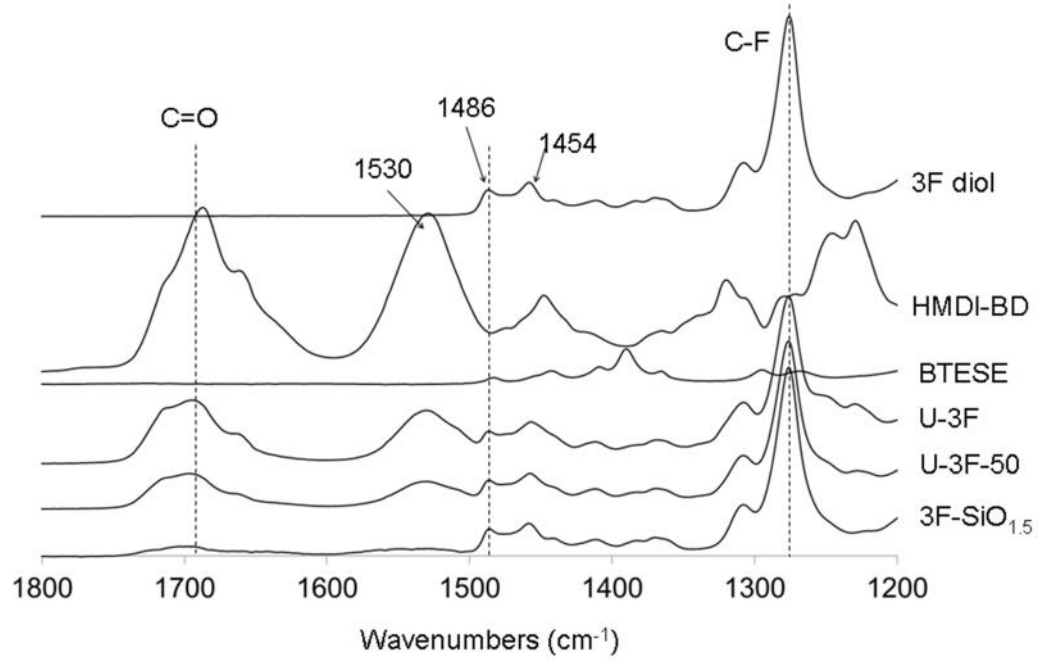

**Figure 2.9.** ATR-IR spectra (diamond crystal) for 3F-4.5 diol, HMDI-BD, BTESE (cured), U-3F, U-3F-50 and 3F-$SiO_{1.5}$.

The penetration depth for the evanescent infrared wave was calculated from Eq 2,

$$d_p = \frac{\lambda_c}{2\pi[sin^2\theta - \left(\frac{n_s}{n_c}\right)^2]^{1/2}} \qquad \text{Eq. 2}$$

where $n_s$ and $n_c$ are the refractive index of the sample and crystal respectively, $\lambda_c$ is the wavelength in the crystal ($\lambda/n_c$), and $\theta$ is the angle of incidence (45°).[64-65] Figure S2.3 shows an ATR-IR spectrum for U-3F-50 and data used for calculation. At the C=O stretching frequency of 1700 $cm^{-1}$ (~ C=O), the penetration depth for Ge is 0.38 µm and for diamond is 0.98 µm. At a frequency of 1290 $cm^{-1}$ (~ C-F), the penetration depth for Ge is 0.50 µm and for diamond is 1.29 µm.

Figure 2.8 shows ATR-IR spectra (diamond crystal) in the carbonyl region for U-3F-x hybrids. The relative peak areas provide insight into near surface concentration of the 3F-$SiO_{1.5}$ hybrid domain. Figure 2.8 shows that the carbonyl peak area decreases markedly from U-3F to 3F-$SiO_{1.5}$ as the number of carbonyl groups for U-3F (1.78 mmol/g) is 4.4 times higher than that for 3F-$SiO_{1.5}$ (0.404 mmol/g). This calculation assumes that U-3F and 3F-$SiO_{1.5}$ have the same density, an approximation that is based on the high 3F content in U-3F (70 wt%) and 3F-$SiO_{1.5}$ (91 wt%).

Figure 2.10 shows the ratio of observed carbonyl peak area ($CO_{obs}$) to that for U-3F ($CO_{U-3F}$) as a function of wt% U-3F. As noted in the experimental section (and in more detail in Supplemental Information), the ATR-IR peak areas (unfilled squares) obtained with a diamond crystal for U-3F-40 and compositions with lower wt% U-3F are thought to be unreliable due to sample whitening in compression. Data points are included in Figure 2.10, but excluded from discussion.

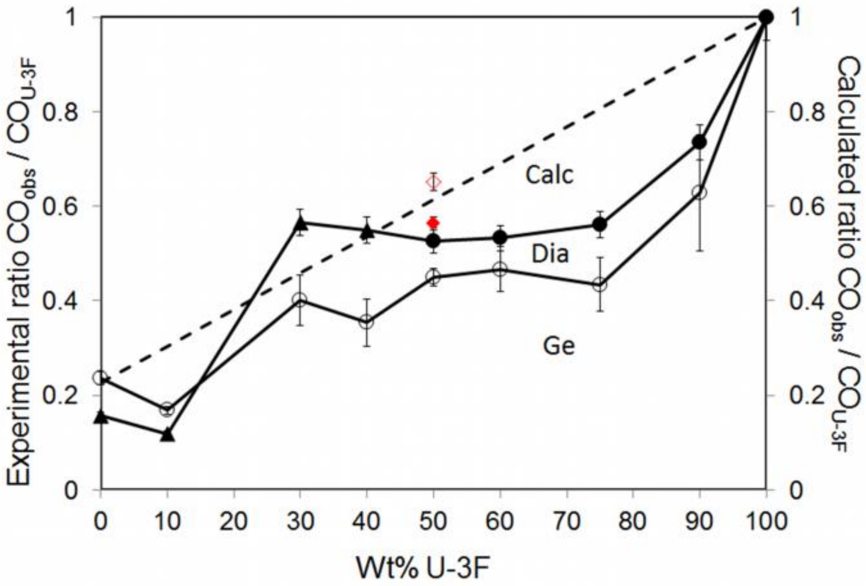

**Figure 2.10.** Ratio of U-3F-x hybrid carbonyl peak area to U-3F as a function of U-3F wt% utilizing Ge (○) and diamond (●, ▲) crystals. See Experimental for diamond crystal symbol explanation. Dashed line is the calculated $CO_{U-3F-x}$ / $CO_{U-3F}$ peak area ratio. Single points are from bulk measurements: æ, Ge; ○, diamond.

The CO / $CO_{U\text{-}3F}$ ratio is consistently lower than the calculated value demonstrating near surface depletion of U-3F, or equivalently, enrichment of 3F-$SiO_{1.5}$. At the carbonyl stretching frequency (1700 $cm^{-1}$), the calculated penetration depth is 380 nm for Ge and 980 nm for diamond. In line with the respective depths for penetration of infrared radiation ($d_p$'s, Eq 2), the $CO_{obs}$ / $CO_{U\text{-}3F}$ ratio is lower for Ge than that for the diamond crystal (Figure S2.3). That is, compared with calculated $CO_{obs}$ / $CO_{U\text{-}3F}$ ratio (0.61) the observed ratio is 0.45. Thus the U-3F wt% is depleted by ~26% in the first 380 nm and ~ 13 wt% to 980 nm (Table 2.3). Below, from an analysis of bulk modulus and adhesion measurements, near surface depletion of U-3F is believed to play an important role in facilitating low EC peak removal force.

We were concerned that near surface carbonyl peak areas might be affected by some unknown variable. The surface layer of a U-3F-50 coating was carefully removed with a razor blade to reveal the bulk. ATR-IR gave normalized peak areas shown in red in Figure 2.10. The peak area for the Ge crystal (unfilled) is above the calculated value while that for the diamond crystal (filled) is below. Both peak areas are higher than the respective surface values giving confidence to conclusions concerning U-3F mesosurface depletion.

The broad absorption at 1530 $cm^{-1}$ attributed to a combination of vibrations for bonds in the urethane moiety appeared to be another target for near surface compositional analysis (Figure 2.9).[62,69] This was not feasible due to peak complexity and interference from absorptions at 1486 $cm^{-1}$ from 3F and at 1454 $cm^{-1}$ from the product of BTESE condensation cure ($Si_2(CH_2)O_{1.5}$). Similarly, the coincidence of an HMDI-BD absorption with that for C-F precluded analysis for the C-F absorption.

*2.3.3.2. Tapping Mode Atomic Force Microscopy*. Topology and morphology for these novel hybrid systems was investigated by TM-AFM imaging. In view of results from adhesion tests described below, root mean square roughness, $R_q$, at the largest surface area imaged (2500 $\mu m^2$) was of interest. Figure 2.11 shows 2D height and phase images for U-3F-50, which are largely devoid of prominent micron scale features that might arise from phase separation.[27,70-71] Slight texturing is apparent in the 50 x 50 µm 2D height image that results in an Rq of 16 nm.

Light and dark regions can be discerned in the 2 x 2 µm phase image that are characteristic of lower and higher modulus, respectively.[72] The higher modulus domains have the appearance of diffuse globules (20-100 nm) that may be associated with 3F-$SiO_{1.5}$. The 2 x 2 µm phase image does not show nanoscale hard block / soft block domain morphological features typically seen for polyurethanes.[27,73-75]

TM-AFM images for 3F-$SiO_{1.5}$ and U-3F-x hybrids other than U-3F-50 are provided in Figures S2.6-S2.8. Surface roughness, Rq, for 50 x 50 µm scans is modest for U-3F-10 (4.7), U-3F-30 (11.3), U-3F-40 (2.9), and U-3F-75 (3.3). Like U-3F-50 (Figure 2.11) 2D height images are devoid of prominent micron scale features. U-3F-60 has the highest $R_q$ of the U-3F-x hybrid elastomers (Figure S2.8, 65 nm, 50 x 50 µm scan).

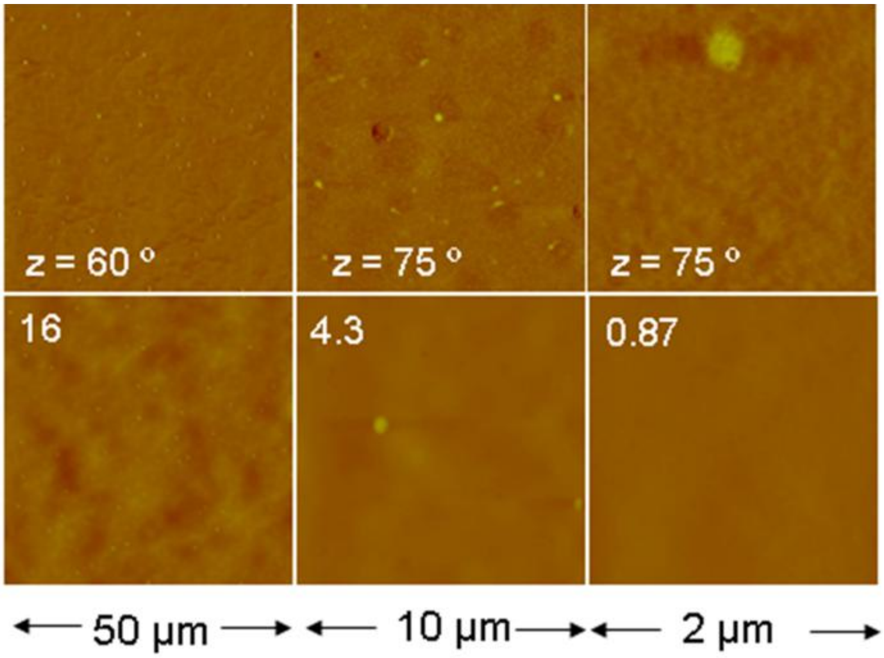

**Figure 2.11.** TM-AFM images for U-3F-50, set-point ratio 0.8 (top, phase; lower 2D height with Rq.

*2.3.3.3. Contact angles* Figure 2.12 shows representative force distance curves (fdc) for U-3F-50). The relationship used to calculate contact angles from fdc's is summarized and points on the ordinate used for $\theta_{adv}$ and $\theta_{rec}$ are shown. Dynamic and sessile drop contact angles as a function of composition are listed in Table 2.3. $\theta_{adv}$ is similar for all compositions (~5º range), while $\theta_{rec}$ varies over ~14° (Table 2.3). Sessile drop $\theta_{adv}$ tracks $\theta_{adv}$ dynamic contact angles.

The three immersion /emersion fdc cycles shown in Figure 2.12 superpose demonstrating that no water insoluble species leach from the U-3F-50 coating over the course of ~10 min.[53] This observation is attributed to the $–SiO_{1.5}$ network that does not permit long range chain reorganizations that are often observed in linear polyurethanes.[76] In addition, liquid-liquid extraction of the 3F diol reduces low molecular weight (LMW) linears and cyclics (particularly the cyclic tetramer) to a negligible level.[47] Thus, there is no evidence for diffusion of LMW species that contaminates water and leads to inaccurate contact angles. This observation gives some assurance that mobile surface species do not affect the adhesion measurements.

A relationship between receding contact angles and adhesion was found by Chaudhury.[30-31] Decreased $\theta_{rec}$, that is, increasing contact angle hysteresis was correlated with increased adhesion. Compared to coatings reported by Chaudhury that had low adhesion ($\theta_{rec}$ ~ 90º) receding contact angles for polyurethanes with 3F polyoxetane soft blocks are low and contact angle hysteresis is high (~50º). Receding contact angles for the U-3F-x hybrids are in the range 55 – 68° without a discernable trend with composition (Table 2.3). For U-3F, a 55° $\theta_{rec}$ was reported recently.[27,47] Contact angles will be considered further in the discussion of adhesion.

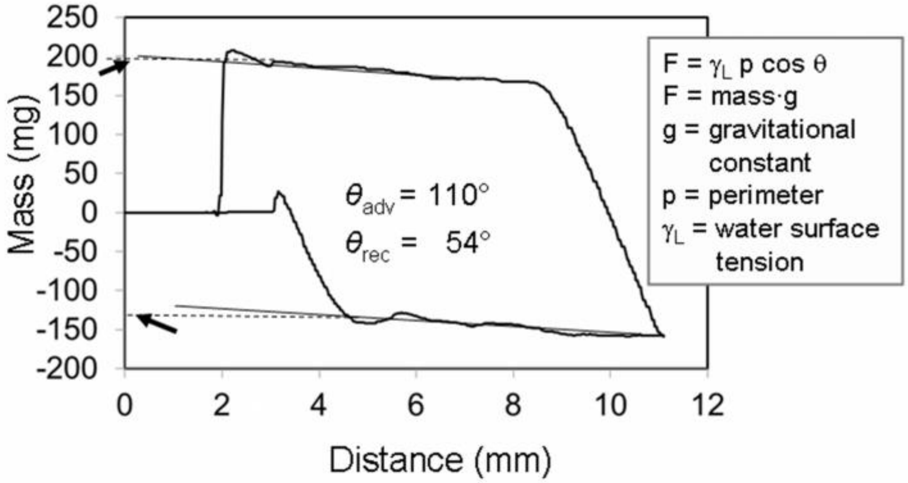

**Figure 2.12.** DCA force distance curves for U-3F-50. Three curves superpose demonstrating no contamination of water during analysis.

**Table 2.3.** Dynamic contact angles, carbonyl peak areas, coating thicknesses, and adhesion measurements

| Designation | Dynamic contact angles (°) | | Normalized C=O peak areas | | | Coating thickness (µm) | Adhesion measurements | |
|---|---|---|---|---|---|---|---|---|
| | $\theta_{adv}$ | $\theta_{rec}$ | Ge | Dia | Calc | | $P_{c\text{-}s}$ (MPa) | RE (J/m$^2$) |
| 3F-SiO$_{1.5}$ | 110 | 64 | 0.23 | 0.16 | 0.23 | 400 | 0.046 | 6.4 |
| U-3F-10 | 108 | 55 | 0.17 | 0.12 | 0.30 | 300 | 0.093 | 17.5 |
| U-3F-30 | 115 | 65 | 0.40 | 0.56 | 0.46 | 300 | 0.094 | 18.2 |
| U-3F-40 | 114 | 59 | 0.35 | 0.55 | 0.54 | 300 | 0.068 | 10.3 |
| U-3F-50 | 110 | 54 | 0.45 | 0.53 | 0.61 | 200 | 0.078 | 5.1 |
| U-3F-60 | 109 | 68 | 0.47 | 0.53 | 0.69 | 250 | 0.14 | 37.1 |
| U-3F-75 | 108 | 64 | 0.43 | 0.56 | 0.81 | 200 | 0.15 | 36 |
| U-3F-90 | 113 | 57 | 0.63 | 0.74 | 0.92 | 200 | 0.46 | 133 |
| U-3F | 107 | 55 | 1 | 1 | 1 | 300 | 0.50 | 145 |

<u>*2.3.3.4. Solvent resistance.*</u> Oleophobic character is an important consideration in coating applications. Strips of U-3F-50 and condensation cured PDMS were immersed in hexadecane for 24 hr. U-3F-50 absorbed 6.3 wt% hexadecane while PDMS was swollen with 35.5 wt%. This noteworthy difference in hexadecane uptake is attributed to the high 3F weight percent and the presence of the $–SiO_{1.5}$ network in the elastomer.

<u>*2.3.3.5. Adhesion.*</u> The ease of removal of a rigid bonded object may be assessed by a test that involves applying a force probe at a shallow angle to the substrate. This removal test is conveniently carried out with epoxied aluminum cylinders (ECs).[3,44-46] The test for EC removal in shear mimics the removal of rigid bonded objects.[35] Compared to the tensile removal test, the shear removal test better imitates a conventional cleaning process that is normally done by a water spray or brush.

The force per unit area at which a rigid object is released has been designated critical removal stress,[6] shear adhesion strength,[77] or shear stress.[35] The geometric arrangement approximates shear modulus for elastomers (G) rather than tensile modulus (E), but the two are related by the relationship $E = 3G$.[78] To retain a designation similar to Kendall's ($P_c$ in Eq 1) tensile removal force is designated $P_{c-t}$ whereas removal in shear is $P_{c-s}$.

The adhesion test used for EC removal is described in the Experimental section. A moderate dependence of $P_{c-s}$ on shear rate was found by Kim.[35] From Kim's results on hydrosilation cured silicone coatings, the 50 µm/sec shear rate employed in the present work probably results in relatively high peak removal forces for the hybrid coatings. Coating thicknesses were 200 - 300 µm. This is a fairly narrow thickness range compared to those investigated by Kim (160 – 740 µm). Future studies on U-3F-x hybrid coatings are planned to understand the details for the relationship of $P_{c-s}$ with macroscopic coating thickness and test shear rate.

The $P_{c-s}$ test employs a TA RSA-3 dynamic mechanical analyzer and parallels tests reported previously.[3,35,44] The TA RSA-3 is well suited for these tests as the 3.5 kg load cell facilitates accurate measurements. This test gives *peak force* ($P_{c-s}$) for EC removal (Figure 2.13). To our knowledge, $P_{c-s}$ measurements with the TA RSA-3 are the first utilizing a commercial instrument. Prior measurements have been obtained with manual gauges[3] or custom built devices.[4-6]

Instrument software gives the area under the force-distance curve thus providing *removal energy* (RE). This is the first report of RE for rigid bonded objects. Figure 2.13 shows a representative EC removal test for a U-3F-50 coating (average values for multiple tests, Table 2.3).

The EC removal test was used for U-3F-x hybrid compositions, 3F-$SiO_{1.5}$ and U-3F (Table 2.3). Although plaques of 3F-$SiO_{1.5}$ and U-3F-10 were too fragile for tensile tests and DMA, damage was not observed in $P_{c-s}$ tests. Also, the test was successfully performed on U-3F-10, U-3F-30 and U-3F-40 without damage that occurred during coating compression by the holder in ATR-IR spectroscopy (Figure S2.1).

After EC detachment, no visual sign of epoxy adhesive residue (grey) was apparent on the hybrid coatings or U-3F. U-3F-40 was selected for carrying out repeated removal tests on the same spot where the previous cylinder was bonded. Within experimental error, there was no change in $P_{c-s}$ or RE. Low standard deviations (error bars, Figure 2.14) attest to high reproducibility. From these observations, ECs removal constituted adhesive failure.

Figure 2.14 shows the relationship between U-3F wt% and $P_{c\text{-}s}$ as well as RE. $P_{c\text{-}s}$ for 3F-$SiO_{1.5}$ was 0.046 MPa (Table 2.2). With incorporation U-3F, $P_{c\text{-}s}$ increased to 0.093 MPa for U-3F-10 and 0.094 MPa for U-3F-30. Unexpectedly, increasing U-3F wt% led to a modest trend reversal, which is more noticeable for RE compared to $P_{c\text{-}s}$. If $P_{c\text{-}s}$ is the criterion, U-3F-40 has an adhesion minimum ($P_{c\text{-}s}$, 0.068 MPa); if RE is the criterion, EC adhesion minimum is at U-3F-50 (5.1 $J/m^2$). Considerably higher $P_{c\text{-}s}$ and RE are found for hybrids with higher U-3F content. $P_{c\text{-}s}$ and RE are similar for U-3F-60 and U-3F-75 hybrids, but a jump in removal force to 0.46 MPa and RE (133 $J/m^2$) is seen for U-3F-90.

The adhesion minimum at 40-50 wt% U-3F is an important and non-obvious result (Figure 2.14 and Table 2.3). This minimum is discussed further below and correlated with bulk modulus and with ATR-IR evidence for mesosurface depletion of U-3F (Figure 2.10).

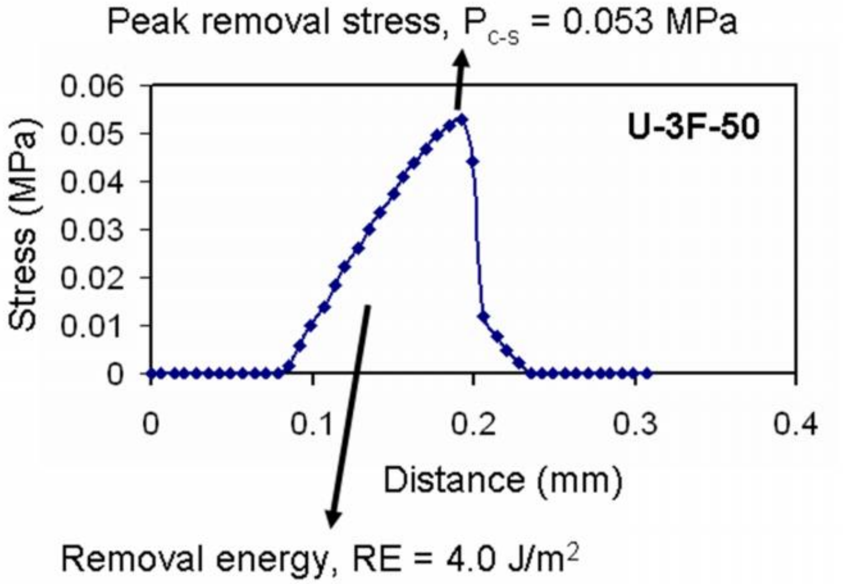

Peak removal stress, $P_{c\text{-}s}$ = 0.053 MPa

Removal energy, RE = 4.0 J/$m^2$

**Figure 2.13.** Removal stress versus distance for an EC from U-3F-50; $P_{c\text{-}s}$ and RE are 0.053 MPa and 4.0 J/$m^2$, respectively.

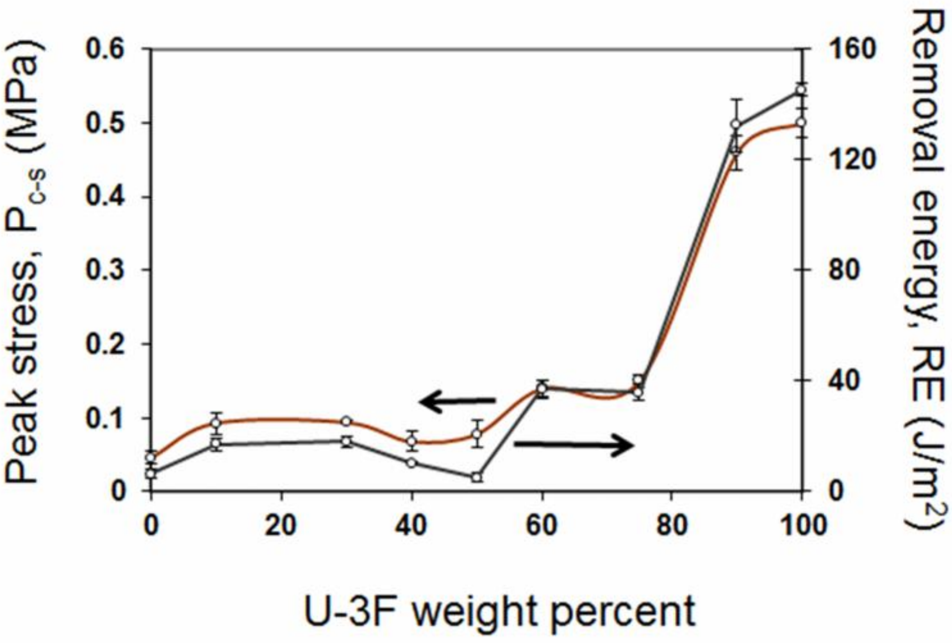

**Figure 2.14.** *Left*: peak removal stress in shear ($P_{c-s}$) for removal of an epoxied aluminum cylinder from U-3F coatings; *right*, removal energy, RE.

## 2.4. Discussion

Hybrid elastomers are easily prepared from a solution blend of linear polyurethane U-3F, which forms a physical network (PN), and a mixture of triethoxysilyl end-capped 3F polyoxetane and alkoxysilane BTESE, which augments siliceous content, or chemical network (CN). A series of blend compositions were prepared having 10 to 90 wt% U-3F. A striking compositional dependence was found for EC peak removal force $P_{c-s}$ and removal energy (RE). U-3F-50 has an attractive combination of toughness (6.2 MPa, Table 2.2) and minimum peak removal force (0.078 MPa, Figure 2.14, Table 2.3).

Virtually all published research on RARE $P_c$ concerns poly(dimethylsiloxane) based coatings. To place the result for U-3F-50 in perspective, $P_{c-s}$ measurements on filled and unfilled PDMS elastomers are considered. For the former, Xie studied hydrosilylation cured Dow Corning T4 resin, which contains at least 30% silica filler.[79] In a test similar to that described herein, but for 500 μm coatings at a very low strain rate (0.9 mm/s), $P_{c-s}$ was 0.21 MPa. To gain a rough "calibration" of our adhesion measurements, we tested a PDMS elastomeric coating made from a similar resin (Dow Corning Sylgard 184). $P_{c-s}$ (0.15 to 0.30 MPa) depended on inversely on thickness (400 to 50 μm). The differing thickness, strain rate and compositions preclude a direct comparison, but it is interesting that $P_{c-s}$ for Xie's 500 μm DC-184 coating (0.21 MPa) and $P_{c-s}$ for the DC-Sylgard-184 400 μm coating (0.15 MPa) are relatively close.

Unfilled PDMS elastomers were studied by Kim, who reported results for two (unfilled) hydrosilylation (Pt) cured silicone coatings.[35] These elastomers have low bulk moduli: "V-21" (1.3 MPa) and "V-35" (0.08 MPa). From tests on single component coatings at strain rates and coating thicknesses approximating those used in the present study, $P_{c\text{-}s}$ ranged from 0.1 (V-21) to 0.05 MPa (V-35). The lower modulus, high MW PDMS coating (V-35) had the lower $P_{c\text{-}s}$.

The peak removal force for U-3F-50 (0.078 MPa) is in the range of the two hydrosilylation (Pt) cured silicone coatings reported by Kim.[35] Such unfilled silicone coatings, whether condensation or hydrosilylation cured are mechanically weak. Strain to break is typically ≤ 20%.[80-81] Strain to break for silica reinforced resins such as Dow Corning T4 is ~400%, but Xie found that the force to remove a rigid bonded object, $P_{c\text{-}s}$, is relatively high (0.21 MPa).[79] Similarly, we found that $P_{c\text{-}s}$ for (Dow Corning Sylgard 184) was 0.15 to 0.30 MPa depending on thickness. This silica reinforced elastomer has a strain to break of ~ 242%.[82]

U-3F-50 has a low $P_{c\text{-}s}$ (0.078 MPa) in the range of unfilled silicone elastomer[35] but a strain to break that exceeds fumed silica filled PDMS examined by Xie.[79] To rationalize these results, Figure 2.15 defines near surface, bulk, and coating-substrate regions. The "nanosurface" **n-S** is the outermost region (≤ 1 nm) that conventionally determines surface energy. The mesosurface **m-S** lies between the nanosurface and bulk (**B**). Region **I-Ad** determines adhesion to substrate and is of practical concern for tests associated with removal of rigid objects. **I-Ad** is addressed only indirectly in that the removal test did not result in adhesive failure of the coating to the substrate.

*2.4.1. Bulk modulus.* A 7% decrease in modulus occurs from U-3F (10.5 MPa) to U-3F-90 (9.8 MPa), while an 80% drop is found for U-3F-75 (2.3 MPa). This decreased modulus is attributed to network constrained phase separation imposed by the $-SiO_{1.5}$ network that works against U-3F hard block association.[59] Hybrids with 40 – 75 wt% U-3F have moduli in the range 2-4 MPa without systematic trends.

Previous findings for PDMS elastomers have found a square root dependence of elastomer modulus on EC peak removal force (Eq 1).[35] Applying Eq 1 and assuming other variables are constant the ratio $[K_{U\text{-}3F}]^{1/2}$ / $[K_{U\text{-}3F\text{-}50}]^{1/2}$ is $1.6_2$. Coating thickness is different for U-3F (300 µm) and U-3F-50 (200 µm). Taking this difference into account, $P_{c\text{-}s}$U-3F / $P_{c\text{-}s}$U-3F-50 becomes $1.3_2$. From Table 2.3, the ratio of $P_{c\text{-}s}$U-3F / $P_{c\text{-}s}$U-3F-50 is $6.4_1$. Thus, decreased bulk modulus accounts for only 21 – 25 % of the $P_{c\text{-}s}$ reduction for U-3F-50 compared to that for U-3F.

*2.4.2. Mesosurface U-3F depletion.* From analysis of the ATR-IR carbonyl peak area the mesosurface (**m-S**) for U-3F-50 is ~26% depleted of U-3F in the first 380 nm and ~13 % to 980 nm (Table 2.3). At 380 nm, the **m-S** is depleted of U-3F to a level approximating that for U-3F-30, the hybrid with lowest U-3F content for which bulk mechanical properties could be determined (47% strain to break). Table 2.2 lists the bulk modulus for U-3F-30 (4.4 MPa) from the stress strain curve in Figure 2.3. The higher bulk modulus for U-3F-30 appears to be at odds with a mesosurface contribution to lower $P_{c\text{-}s}$. However, the bulk strain to break for U-3F-50 is five times higher (261%) than that for U-3F-30 (47%). Clearly, mesoscale U-3F depletion for U-3F-50 results in low mesosurface toughness in the range of U-3F-30 (0.25 MPa). This low toughness must make an important contribution to the low $P_{c\text{-}s}$ for U-3F-50. However, there is no theoretical basis for relating toughness to $P_{c\text{-}s}$. Further work is warranted to explore the mechanical properties of low U-3F wt% hybrid elastomers so that the origin of the contribution of mesosurface mechanical properties to the remarkably low $P_{c\text{-}s}$ for U-3F-50 can be better understood.

*2.4.3. Removal energy.* The inverse correlation of toughness with EC removal energy is apparent when comparing that for U-3F (RE > 145 J/m$^2$, strain at break > 1200%, modulus 10.5 MPa) with U-3F-50 (RE = 5.1 J/m$^2$, strain at break 261 %, modulus 4.0 MPa). The factor of 28 in RE ($RE_{U-3F}/RE_{U-3F-50}$) is an important finding of this study. However, this is a stand alone result as RE has not been reported previously for EC removal. Further work is planned to better understand the significance of RE and to acquire data for other RARE systems.

*2.4.4. Contact angles.* A low receding water contact angle has been correlated with high adhesion,[30-31] but $\theta_{rec}$ is low for all U-3F-x hybrids (Table 2.3). There is no relationship between $\theta_{rec}$ and changes in $P_{c-s}$ or RE with U-3F-x coating composition. Furthermore, $\theta_{rec}$ is low (~60°) compared to PDMS coatings (~80°).[53] Advancing contact angles for these hybrid fluorous coatings show little fluctuation with increasing U-3F wt% (Figure 2.15, Table 2.3). Sessile drop contact angles closely track dynamic $\theta_{adv}$. Advancing contact angles are in the range of PDMS coatings reported by Kim (118°).[35] Based on minimal changes for sessile drop $\theta_{adv}$ and dynamic $\theta_{adv}$, the work of adhesion cannot vary greatly.

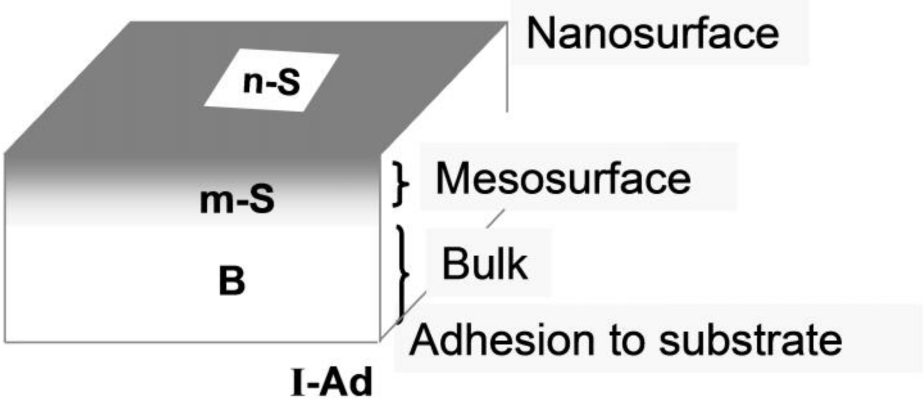

**Figure 2.15.** Proposed model for U-3F-x coating cross-section showing **n-S**, the nanosurface or outermost layer, **m-S**, the mesosurface, **B**, the bulk and **I-Ad** the interface with the substrate.

## 2.5. Conclusion

Bulk and surface characterization together with adhesion measurements have established U-3F-x coatings, and U-3F-50 in particular, as new fluorous rigid adherent-resistant elastomers (RARE) that are tough, hydrocarbon resistant, and optically transparent. The principle findings are:

(1) Increased bulk mechanical properties, particularly toughness, with increasing U-3F wt% (Figures 2.3, 2.4 and Table 2.2)

(2) Mesosurface U-3F depletion from ATR-IR spectroscopy with Ge and diamond crystals

(3) A test for peak removal force $P_{c-s}$ using a sample holder for a microscope slide in conjunction with a commercially available TA RSA-3 instrument; integration software that provides removal energy (RE).

(4) A striking compositional dependence for peak removal force $P_{c-s}$ and RE for a rigid bonded object (EC), and

(5) An optimized combination of $P_{c-s}$ and RE for the U-3F-50 hybrid coating by standards of high bulk toughness (6.2 MPa) and minimum peak removal force (0.078 MPa).

As noted earlier, most published research on RARE $P_c$ concerns poly(dimethylsiloxane) based coatings. The combination of toughness and low EC adhesion for the U-3F-50 hybrid coating with the advantage of resistance to hydrocarbon solvents meets or exceeds the performance of PDMS systems noted above. Finally, the U-3F-50 hybrid elastomers compare favorably with PDMS polyurethane networks reported by Webster.[5,13]

Research is underway to explore systematically a number of variables not addressed in this initial investigation. Compositional variations such as the wt% siliceous domain as well as the effects of time, temperature, and humidity on processing and cure for co-condensation of **3** and **4** are subjects of study so as to understand U-3F mesosurface depletion. These variables also merit study to clarify changes in dynamic mechanical behavior that are connected with hard block phase separation. Effects of coating thickness, force probe speed and other variables for the EC removal test will are also subjects for additional studies.

## 2.6. Supplemental Information

### 2.6.1. Synthesis.

*Preparative procedure for U-3F-50.* A THF solution containing polyurethane U-3F **6** (2.2 g) was added to a THF solution containing **3** (2.2 g), **4** (0.22 g) and DBTDA catalyst (0.5 wt %). The resulting solution was stirred for 30 min prior to coating microscope slides. Coatings (~0.5 mm) and dip-coated glass slides were prepared by solution casting followed by drying under vacuum for 24 hr at 60 °C. The coated slides were kept at 100 ºC overnight to ensure complete cure. Plaques (~ 150 µm) were prepared by spreading solutions on PTFE plates, curing overnight at ambient temperature, and further curing at 100 °C for 24 hr.

*3F-$SiO_{1.5}$.* As a control, a portion of precursor solution **5** was cured without addition of U-3F. This control sample is designated 3F-$SiO_{1.5}$. Bis(triethoxysilyl)ethane undergoes hydrolysis / condensation cure to a largely siliceous domain that has the empirical formula $Si_2(CH_2CH_2)_2O_{1.5}$. End groups from **3** also undergo "moisture cure". For simplicity, we designate the siliceous phase "-$SiO_{1.5}$".[2]

### 2.6.2. ATR-IR Spectroscopy.

Spectra with a Ge crystal were obtained with a Nicolet 400 FT-IR spectrometer, while spectra with a diamond crystal were obtained with a Nicolet IS10 (Figure 2.10).

*Nicolet 400 (Ge crystal).* A Nicolet 400 spectrometer equipped with a Thunderdome accessory was used for acquiring carbonyl peak intensities with a Ge prism (Figure 2.10); 32 scans were taken from 500 to 4000 $cm^{-1}$. Spectra were analyzed using Omnic software. For this ATR-IR accessory, the Ge crystal is coplanar with the sample stage, minimizing compressive stress on the elastomeric coatings. Sample whitening (described below for compositions having ≤ 40 wt% U-3F using a Nicolet iS10 spectrometer) was not observed except for a modest effect on U-3F-10 and U-3F-40.

*Nicolet IS10 (diamond crystal).* A Thermo Scientific Nicolet iS10 spectrometer was used with a Smart iTR attachment; 32 scans were taken from 500 to 4000 $cm^{-1}$. Spectra were analyzed using Omnic software.

For acquiring spectra, a slide was placed on the Smart iTR attachment and pressure was applied to obtain uniform contact with the crystal, which is positioned beneath the plane of the holder. For compositions having ≤ 40 wt% U-3F, the area in contact with the crystal was white after the coated slide was removed (Figure S2.1). The white appearance is attributed to stress in compression due to the pressure screw and strain resulting from the sub-surface position of the crystal. Attempts to obtain spectra by carefully turning the screw to a position prior to the set “click” pressure failed. The peak areas for ≥ 50 wt% U-3F are reported in Figure 2.10 as filled black circles. Peak intensities acquired for compositions with ≤ 40 wt% U-3F are reported as open squares.

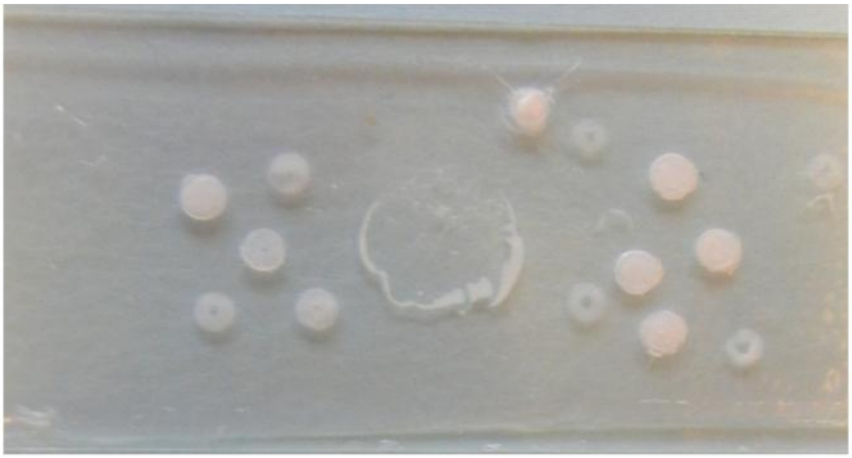

**Figure S2.1.** Digital image of a slide coated with U-3F-40 after ATR-IR spectra.

### 2.6.3. Atomic Force Microscopy

*TM-AFM imaging for 3F-SiO1.5, U-3F-10, U-3F-40, U-3F-60, U-3F-1.5 and U-3F-90.* TM-AFM images for 3F-$SiO_{1.5}$ and U-3F-x hybrids other than U-3F-50 are provided in Figures S2.6-S2.8. Surface roughness, Rq, for 50 x 50 µm scans is modest for U-3F-10 (4.7), U-3F-30 (11.3), U-3F-40 (2.9), and U-3F-75 (3.3). Like U-3F-50 (Figure 2.11) 2D height images are devoid of prominent micron scale features. U-3F-60 has the highest Rq of the U-3F-x hybrid elastomers (Figure S2.8, 65 nm, 50 x 50 µm scan).

3F-$SiO_{1.5}$. TM-AFM images for 3F-$SiO_{1.5}$ are shown in Figure S2.6 ($r_{sp}$ = 0.8). The 50 x 50 µm phase image reveals a remarkably complex near surface morphology. These features are apparently a result of phase separation and shrinkage during condensation cure. There may be a synergy resulting from hydrogen bonding between the urethane and remainder –Si-OH groups that underlies this complex morphology.

U-3F-10. Figure S2.6 shows that including 10 wt% 3F-U results in a dramatic change in near surface morphology. U-3F-10 has a much less complex surface morphology with negligible microscale and nanoscale features.

Like U-3F-10, hybrid compositions with higher wt% U-3F generally have much less complicated near surface morphologies compared to 3F-Si/H. U-3F-30 images are shown in Figure S2.7. A pattern of fine micron scale features are seen in the 50 x 50 µm images as well as nanoscale phase separated domains in the 2 x 2 µm images. For a comparable scan area, surface roughness ($R_q$ is shown in the 2D height images) is less for U-3F-x hybrids compared to 3F-Si/H.

Figure S2.7 shows images for U-3F-40. Because of the relatively featureless surfaces, only images for a setpoint ratio of 0,8 are shown. Nanoscale features are attributed primarily to near surface siliceous domains, as surface depletion of U-3F is shown by ATR-IR. Darker colored patches similar to the 30% hybrid coatings are also observed here for smaller scan sizes. The 50% hybrids show a very smooth surface with very faint or no features at softer tapping whereas hard tapping shows a phase mixed near surface morphology.

U-3F-60 coatings are exceptional in showing high surface roughness and a very well segregated near surface morphology (Figure S2.8). Perhaps some as yet not understood variation in coating deposition accounts for this exceptional surface morphology. Smaller scan sizes show a phase mixed near surface morphology.

The U-3F-75 coating shows strand like near surface features that are well dispersed throughout the phase image (Figure S2.8). These features are more prominent at softer tapping rather than hard tapping, signifying that they are more predominant at the near surface. For harder tapping at the nanoscale, some signs of phase separation are observed.

The U-3F-90 coating shows a fair amount of phase separation at both the microscale and the nanoscale having distinct light and dark colored regions throughout the phase image (Figure S2.8). These AFM images are very much analogous to those for the neat 3FOx polyurethane signifying the fact that most of the near surface of U-3F-90 is dominated by the linear 3FOx-PU. U-3F-90 coatings have relatively high Rq.

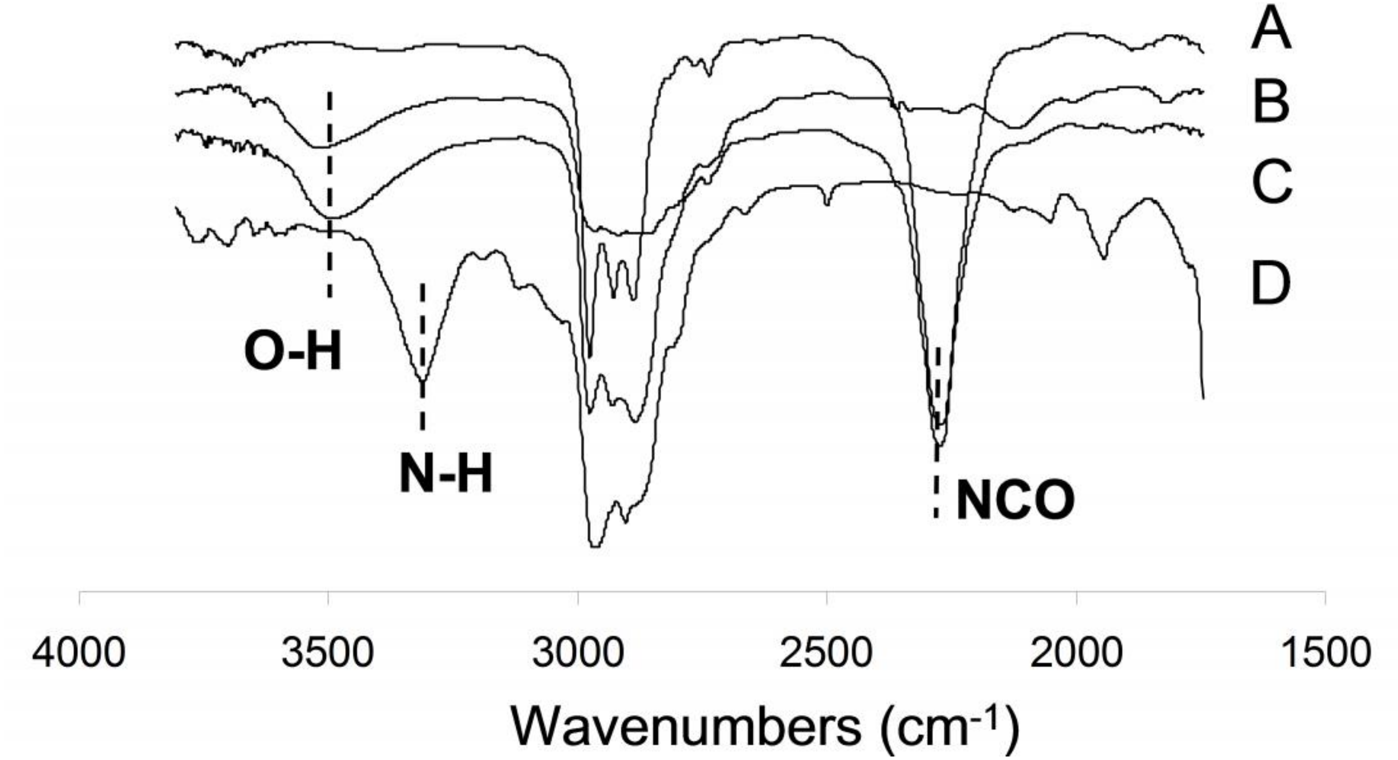

**Figure S2.2.** FTIR spectroscopic monitoring for formation of hybrid precursor **3**: **A**, isocyanato-propyl alkoxysilane **2**; **B**, 3F-4.5 diol **1**; **C**, initial (t = 0) reaction mixture; **D**, reaction mixture at t = 24 hr showing formation of **3**.

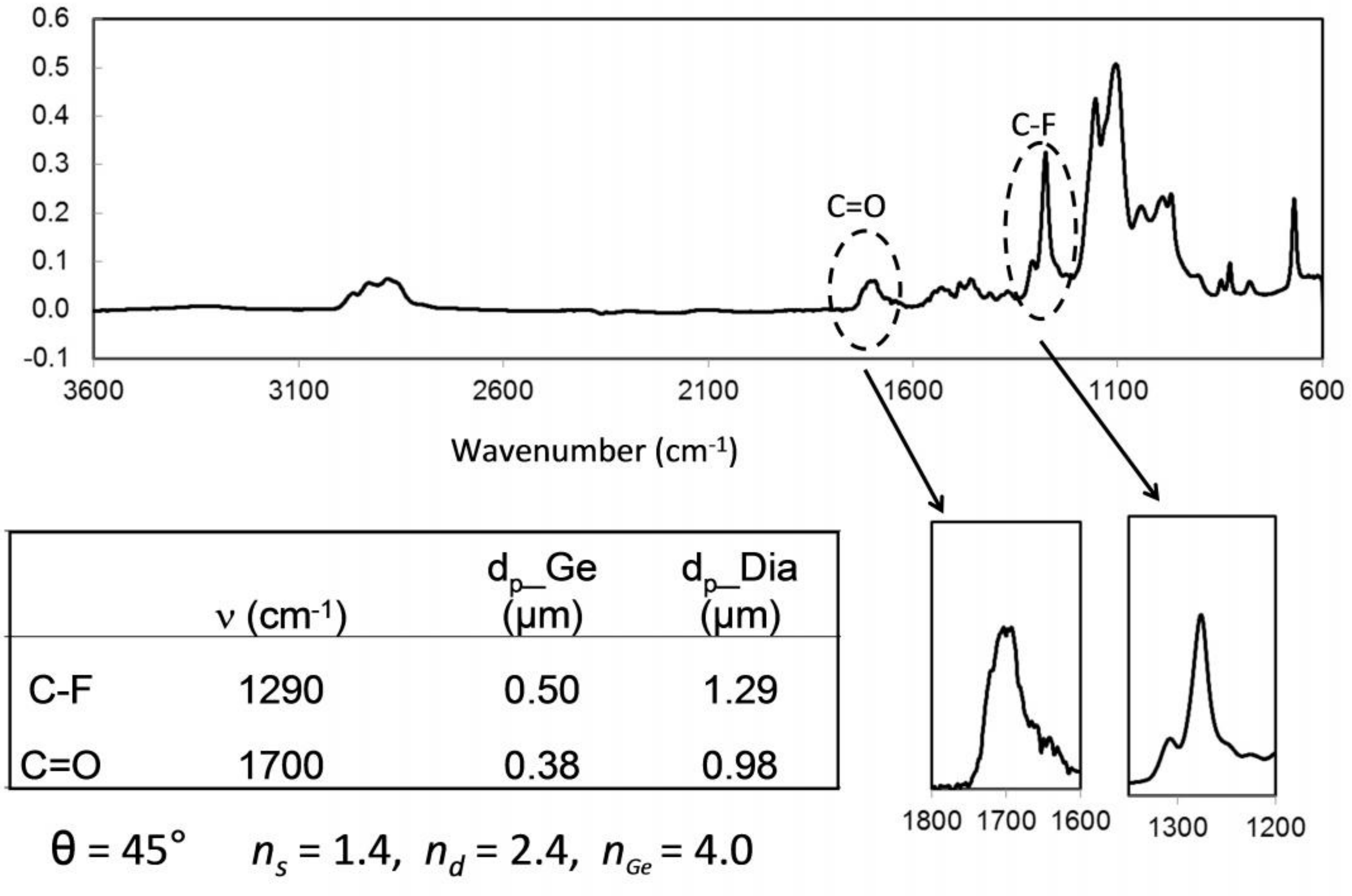

|  | $\nu$ (cm$^{-1}$) | $d_p$_Ge (µm) | $d_p$_Dia (µm) |
|---|---|---|---|
| C-F | 1290 | 0.50 | 1.29 |
| C=O | 1700 | 0.38 | 0.98 |

$\theta = 45°$ $n_s = 1.4$, $n_d = 2.4$, $n_{Ge} = 4.0$

**Figure S2.3.** ATR-IR spectrum for U-3F-50 and calculation of $d_p$ for Ge and diamond at the carbonyl and C-F stretching frequencies.

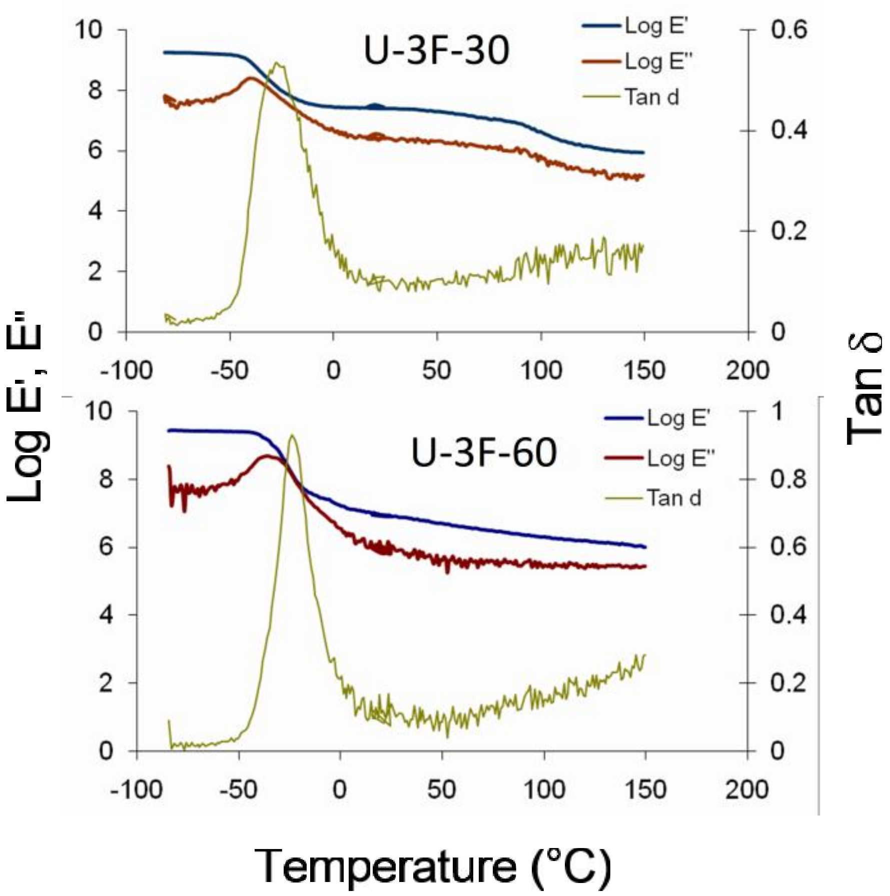

**Figure S2.4**. DMA for U-3F-30 and U-3F-60.

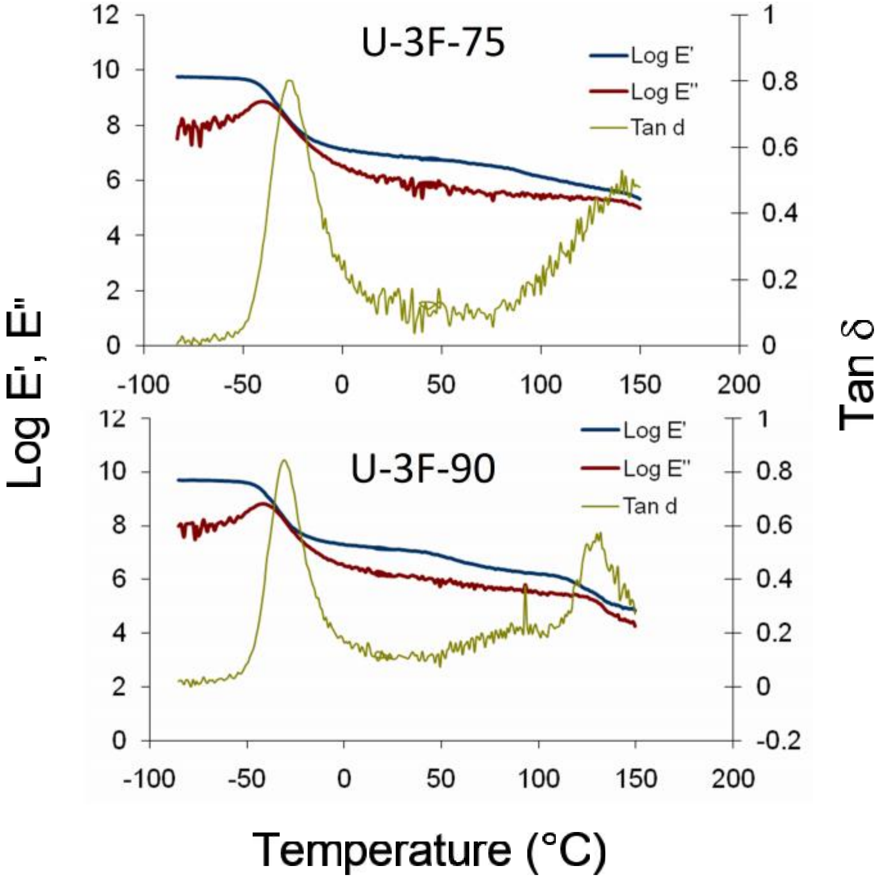

**Figure S2.5**. DMA for U-3F-75 and U-3F-90.

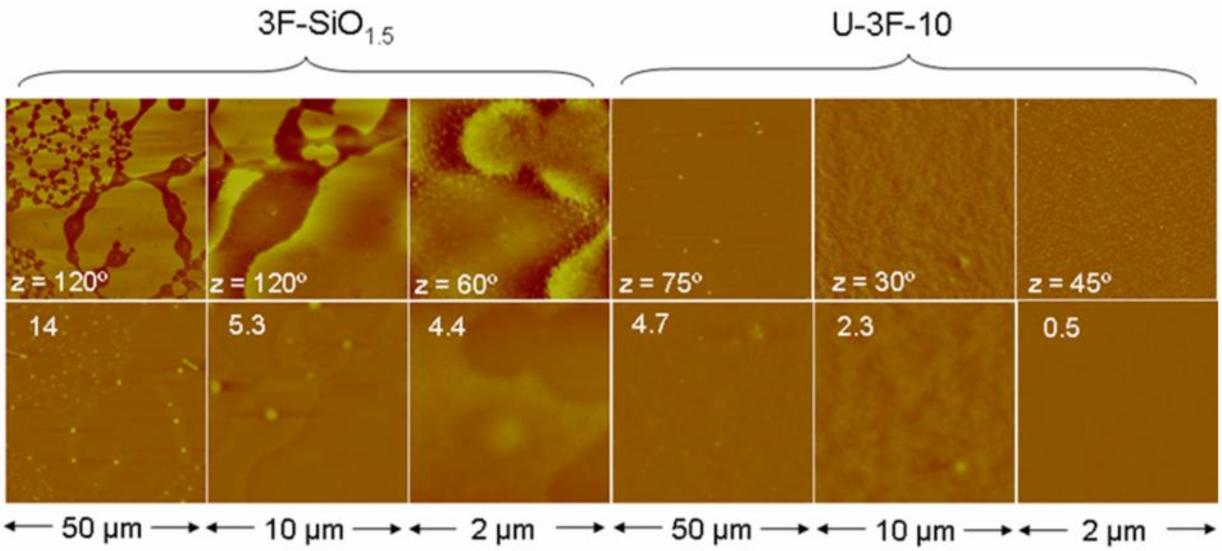

**Figure S2.6.** TM-AFM images for 3F-SiO$_{1.5}$ and U-3F-10 coatings; upper, phase; lower, 2D height with Rq at $r_{sp}$ = 0.8.

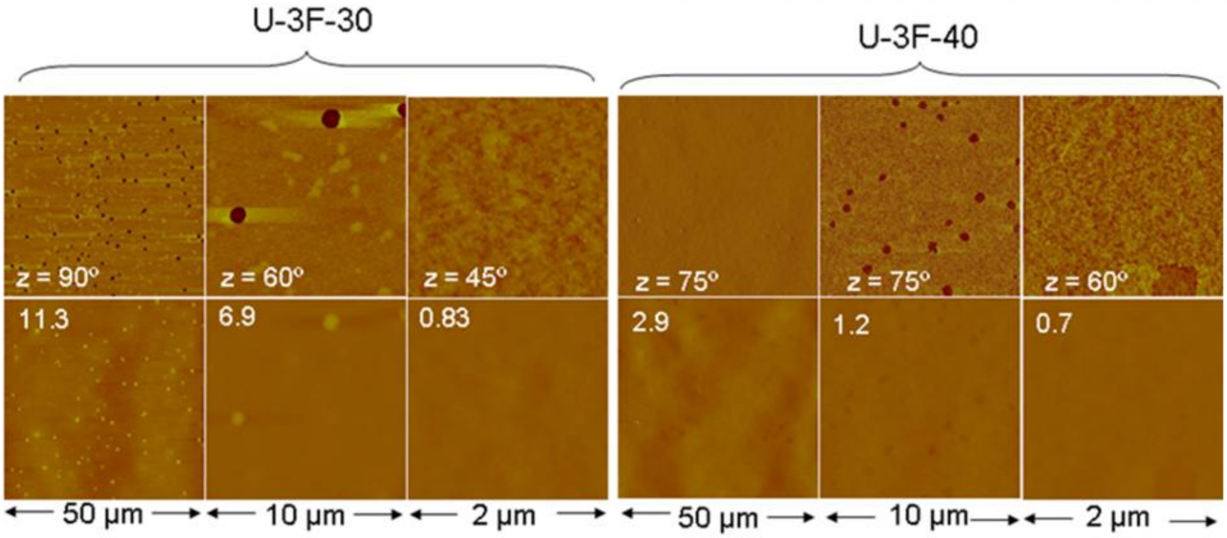

**Figure S2.7.** TM-AFM images ($r_{sp} = 0.8$) for U-3F-30 and U-3F-40 coatings; upper, phase; lower 2D height with Rq.

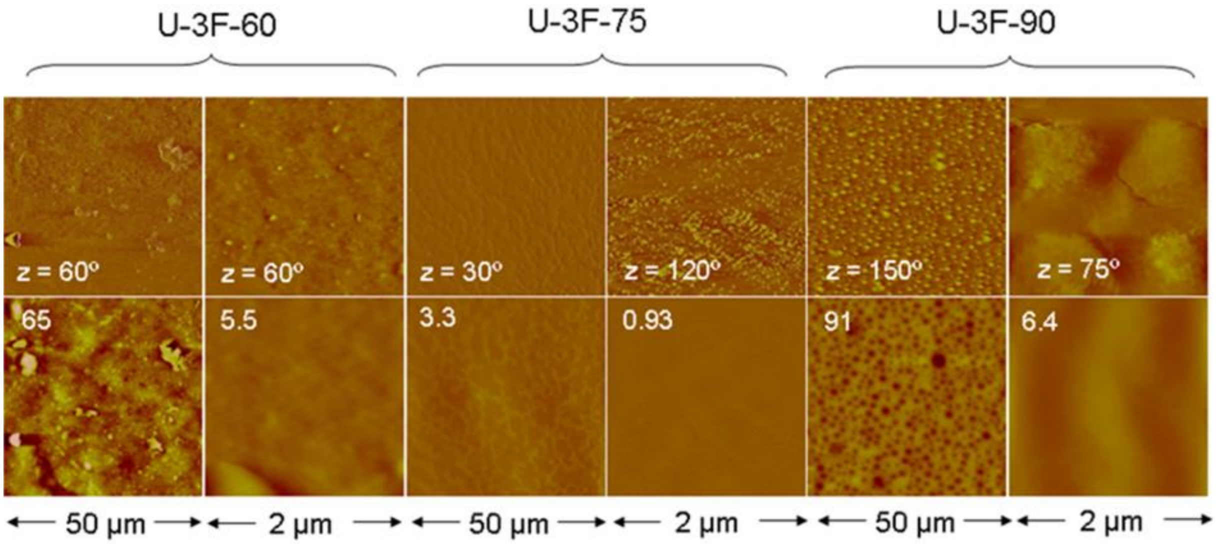

**Figure S2.8.** TM-AFM images ($r_{sp}$ = 0.8) for U-3F-60, U-3F-75 and U-3F-90 coatings; upper, phase; lower 2D height with Rq.

# CHAPTER 3

# A laboratory test for ice adhesion strength using commercial instrumentation

## 3.1. Introduction

Ice accumulation oftentimes has adverse effects on energy infrastructure including wind turbines, offshore oil exploration, transportation, and electric wires.[1,36,83-88] Ice adhesion and accumulation result in a range of problems leading to reduced performance and interference with normal operations. Problematic ice accumulation is also associated with air conditioning systems and commercial refrigeration.

Thus far, only custom built equipment has been employed for quantitative assessment of ice adhesion. Most often, various probe designs are used to remove ice in shear. In 1978, Jellinek reported ice shear adhesion measurements using equipment "supplied by the U. S. Army Corps of Engineers, CRREJ, and designed by K. Itagaki".[83] This work evaluated ice adhesion to several substrates including poly[(dimethylsiloxane)-*b*-bisphenol-A-polycarbonate)] copolymer films. In 1992 Crouch and Hartley reviewed ice adhesion and presented shear adhesion measurements for a variety of coatings including silicones and alkyd paints.[85] They employed an ice removal test apparatus that could be used for both tensile and shear measurements, but shear removal was easier to perform and provided more accurate data.

Meuler provided an extensive review of ice release coatings.[1] An apparatus was described that utilized a Peltier plate to freeze ice on polymer thin films. Multiple ice adhesion tests with a horizontal probe provided removal force in shear. Ice adhesion was correlated with receding contact angles as a measure of the practical work of adhesion.

Another test method is based on removal of ice from a substrate by centrifugal force. For example, Kulinich described spraying cooled water droplets in a wind tunnel, deposition of glaze ice and then mounting the sample on a rotating arm. The rotation rate at which ice was released was compared for several substrates and an "ice adhesion reduction factor" was determined relative to bare aluminum.[87] Test facilities such as The Vertical Lift Research Center of Excellence at Pennsylvania State University also use a centrifugal force method for evaluating ice adhesion.[89] A spray of cool water impinges on the sample and ice builds up until the mass detaches. Mass at release is monitored by a sensor and surface area is determined. Removal force is determined by a numerical analysis.[90]

A test for ice removal was developed by Andrews whereby ice was fractured to produce a crack and then subjected to pressure for ice removal.[84,91] After formation of an ice cylinder, a crack was introduced by non-adherence of ice to a polytetrafluorothylene (PTFE) disc. Subsequently, pressure was applied with a bubble of air compressed by hydraulic oil. Temperature, rate of pressurization and coating thickness were varied and failure energy (critical energy release rate) determined. For a tested polyurethane, the apparent failure energy decreased as the coating thickness increased. The thickness effect was explained quantitatively in terms of flexible polyurethane energy release. The true failure energy was derived and correlated with viscoelastic response.

Yorkgitis and Giaquinto at 3M recently reported tests for ice removal using the Andrews/ Lockington apparatus.[88] Air / corona oxidation of polypropylene was found to increase the ice adhesion parameter and to change the fracture mode from adhesive to cohesive. For unfilled, platinum cured polydimethylsiloxane elastomers (three similar formulations), the ice adhesion parameter decreased with increasing coating thickness. Also, a transition from mostly cohesive to mostly adhesive failure was found with increasing coating thickness.

The investigation reported herein was motivated by the idea that a readily available laboratory test method would facilitate fundamental understanding of surface science relevant to ice adhesion. We report a laboratory test for ice release employing a TA Instruments TA RSA-3 that is customarily used for dynamic mechanical analysis (DMA). The upper grip range of ~10 mm permits a test that uses an easily made sample holder. Peak removal force in shear ($P_S$) is determined while test parameters including temperature and probe speed are easily controlled. The principle of operation is similar to that reported in a study of adhesion of epoxy cylinders (ECs) to RARE, rigid adherent resistant elastomers.[2]

Application of this new ice release test method to a range of coatings and thin films is underway. For this initial report, test development using the prototypical polymer glass poly(methylmethacrylate), PMMA, is described.

## 3.2. Experimental

*3.2.1. Materials.* Poly(methyl methacrylate) (PMMA, $M_w$ = 540 kg/mol) was purchased from Scientific Polymer Products. Tetrahydrofuran (THF, anhydrous) was obtained from Aldrich.

*3.2.2. Coatings.* PMMA solutions were prepared in THF (5, 2.5, 1.25 and 0.625 wt%). Equal volumes of the solutions (~1 mL) were drip coated on microscope glass slides to make coatings with different thicknesses. Solvent removal conditions **A**, **B**, and **C** correspond to designations in Figure 3.7. Solvent was evaporated at ambient temperature followed by residual solvent removal in a vacuum oven at 60 °C for 24 h (**C**, Rq = 23 nm).

To generate coatings with varying roughness, microscope slides with PMMA solutions were: (**A**) placed on a 60 °C hot plate (Rq = 4 nm) or (**B**) covered by 75 × 75 × 25 mm paper box to slow solvent evaporation overnight, followed by residual solvent removal in a vacuum oven at 60 °C for 24 h (Rq = 12 nm). To increase roughness, an embossing method was used. PMMA samples **D** and **E** were melt pressed against paper (ordinary office white paper) and sandpaper (3M Sandpaper, 600-Grit) respectively. Under these conditions, the paper and sandpaper split, but sufficient intact areas were recovered to provide PMMA test surfaces for ice release tests. A release agent was used to prevent adhesion of PMMA to the sandpaper; subsequently the release agent was removed with isopropanol.

*3.2.3. Ice release test*. A coated microscope slide (25 × 75 mm) was cut into 3 pieces (25 × 25 mm). These dimensions are close to the maximum permitted by the temperature controlled chamber. Molds were made by cutting 2 cm long pieces from the large end (top) of pipettes. For tests employing 3 and 4 mm probe distances, Eppendorf 1000 µL pipettes (catalog number 022491954) were used. To accommodate higher peak removal forces associated with 1 and 2 mm probe distances, TipOne 200 µL pipettes (catalog number 1120-8810) were used. The mold was placed on the coating surface and filled with 200 µL distilled water. Samples were placed in a freezer at -15 °C for 2-3 h to form ice cylinders that were 7.5 mm in diameter (1000 µL pipet) or 5.2 mm in diameter (200 µL pipet).

A sample holder was devised for a TA Instruments TA RSA-3 (Figure 3.1B).[92] The force probe is fitted into the upper grip so that it passes a chosen distance (1, 2, 3, or 4 mm) above the coating surface. Temperature control is achieved with liquid nitrogen boil-off. Temperature may be controlled from -5 to -60 °C (± 0.5 °C); tests described herein were conducted at -10 °C.

The coated glass slide with an adherent ice cylinder is rapidly transferred from the freezer to the pre-cooled chamber and sample holder. After closing the chamber, temperature equilibration takes about 2 min. The force probe does not engage the ice cylinder directly, but rather the thin, plastic cylinder containing the ice. The force probe is engaged and moves toward the ice cylinder at a selected speed. DMA software was modified so that a force distance curve is obtained.

Removal force is calculated according to Eq 1.

$$P_s = \frac{4Mg}{\pi d^2} \qquad \text{Eq 1}$$

where $P_s$ is removal force (kPa), $M$ is the normal force recorded by the load cell (g), g is standard gravity (9.8 m/s$^2$) and $d$ is the diameter of ice cylinder (mm). Measurements are reported as the value of $P_s$ followed by the standard deviation (plus/minus).

*3.2.4. Dynamic contact angles.* Wetting characteristics were determined by dynamic contact angle measurements (DCA, Wilhelmy plate) with a Cahn model 312 instrument.[53] Beakers used for DCA analysis were cleaned by soaking in an isopropanol/potassium hydroxide base bath for at least 24 h, rinsed with distilled water and treated with a gas/oxygen flame. Deionised water was used as the probe liquid with an immersion/withdrawal rate of 100 μm/s. Force distance curves often have irregularities near immersion or emersion points, for example, due to variation in coating thickness at the base of the coated slide. An example of an irregularity is the slight upturn in the emersion (receding) fdc shown in Figure 3.9. To correct for this irregularity the main part of the linear force distance curve is extrapolated to the point of emersion, which is used for the calculation of $\theta_{rec}$.

*3.2.5. Differential Scanning Calorimetry.* A TA-Q 1000 (TA instruments) temperature Modulated Differential Scanning Calorimetry (MDSC) was used for determination of thermal transitions at a heating rate of 3 °C /min. and ± 0.5 ºC modulation at 60 s.

## 3.3. Results and Discussion

Previously, we reported a study of adhesion of epoxy cylinders (ECs) to RARE, rigid adherent resistant elastomers.[2] The extension of this method to testing adhesion of ice cylinders was attractive as construction of specialized equipment was not necessary. The method used for ice cylinder formation on a coating is described below followed by the adhesion test. The new method was applied to ice adhesion measurements on PMMA, a prototypical polymer glass. This polymer was chosen for comparison with results from a previous investigation by Meuler with a custom designed apparatus.[1]

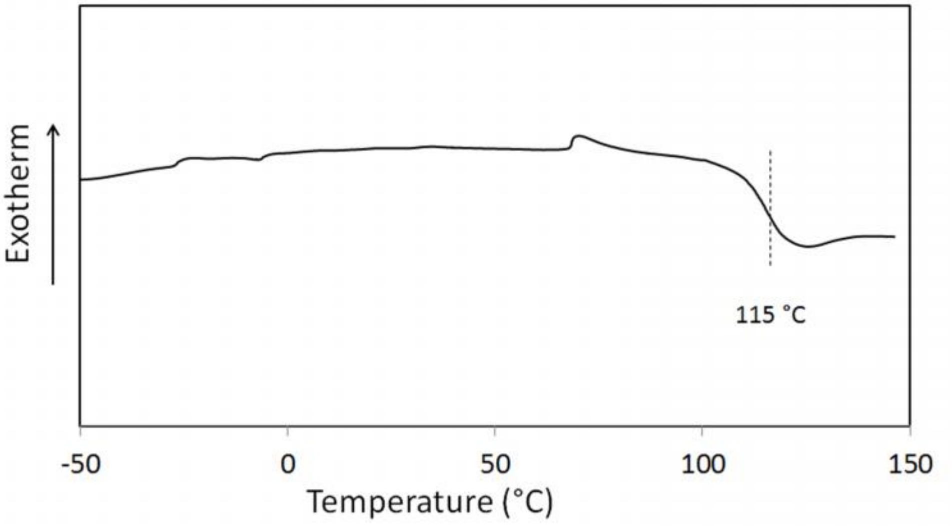

**Figure 3.1.** DSC for PMMA (540 kDa).

*3.3.1. Polymer coatings.* PMMA (540 kDa) is a readily available, well known polymer glass. The $T_g$ for this relatively high molecular weight PMMA is 115 °C, which is 125 °C above the test temperature (Figure 3.1). PMMA is well suited for test trial development because the modulus is nearly flat from ambient temperature to -60 °C.[93]

*3.3.2. Deposition of ice cylinder on coating.* Environmental conditions for ice deposition have been mimicked by ice deposition from water droplets and measurement of adhesion strength using an apparatus that spins the substrate at increasing speeds.[87,90,94-95] Other investigators have simply poured liquid water into a mold on a substrate followed by ice formation.[1,83,85,96-100] We used this latter approach, which is easily adaptable to small coated substrates.

Figure 3.2 depicts the formation of ice cylinders. A glass microscope slide is coated and cut into three pieces, each with dimensions approximately 25 x 25 x 1 mm. Other substrates such as aluminum, steel, and fiberglass are accommodated as long as the substrate dimensions are about the same. Geometric constraints imposed by the temperature controlled chamber preclude tests on larger area samples.

A section (~ 2 cm) is cut from the wide end of a micropipette tip (Figure 3.1a). This cylinder, which serves as the mold during ice formation, is placed on the sample and 200 μL water is added in (Figure 3.2 b, c, d). Pipette tips are made of hydrophobic polypropylene so that surface tension holds water in the cylinder and no water leakage occurs. The water/cylinder is placed in a small freezer for 2-3 h to form the ice cylinder (Figure 3.1 e, f). To avoid sample disruption during transfer, multiple samples may be placed on a tray in the freezer and water added by means of syringe. The inner diameter of the container tube is the outer diameter of the ice cylinder as there is usually no visible ice formation beneath the cylinder wall. This diameter is used to calculate the interfacial area, which is either 7.5 mm (1000 µL pipette) or 5.2 mm (200 µL pipette). The smaller interfacial area was used for 1 and 2 mm probe distances due to peak removal forces that approached or exceeded the load cell limit for 7.5 mm diameter ice cylinders.

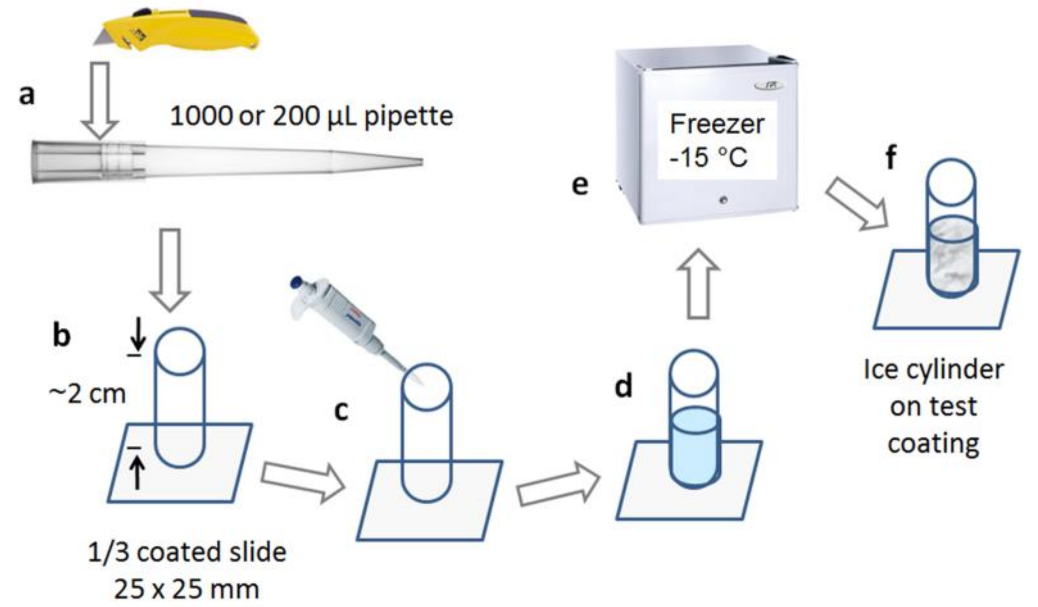

**Figure 3.2.** Steps **a** through **f** for forming an ice cylinder on test coating.

<u>*3.3.3. Ice removal test.*</u> A TA Instruments RSA-3, which is customarily used for dynamic mechanical analysis (DMA), was adapted for the ice release test. The range of motion for the upper grips (~10 mm) is critical for testing adhesion of rigid objects.[2] The TA RSA-3 has a 3.5 kg load cell with 0.2 mg resolution. The low stress limit of this load cell provides precision and accuracy, but precludes measurements for strongly bonded objects. Using liquid nitrogen (LN) boil-off, the chamber temperature may be controlled. The lowest temperature so far is about -60 °C due to heating of LN gas in the delivery system.

A sample holder was fabricated by bending a piece of steel mesh so as to hold a coated slide with adherent ice cylinder (Figure 3.3B and E). The sample holder was fabricated from metal mesh so that the ice-substrate interface could be seen through a view port in the temperature controlled chamber. The force probe does not engage the ice cylinder directly but rather the mold that contains the ice (Figure 3.3C). The force probe is fitted into the upper grip so that it passes close to the coating surface. The distance of the probe to the surface is an important variable that is discussed further below.

A representative ice release test at -10 °C for a 15 μm PMMA coating on glass is shown in Figure 3.4:

**A**, The probe, which is attached to the upper DMA grip, moves vertically in cooled nitrogen gas;

**B**, The probe impinges on the ice cylinder;

**C**, Ice is detached at 446 kPa, which is designated $P_s$, the peak removal force in shear; and

**D**, Zero force after ice cylinder removal. The ice cylinder is removed intact, that is, no residual ice is observed on the PMMA surface (adhesive failure).

The force-distance curve shown in Figure 3.4 is similar to that reported by Zoe, et al., for removal of a frozen water droplet by a conical tip from aluminum and sand blasted aluminum with hydrocarbon and fluorocarbon plasma coatings.[101]

Removal energy (RE) is the area under the force-distance curve. RE for PMMA is low because of the steep force-distance curve. RE may be related to critical energy release parameter provided by a more rigorous test described by Andrews[84,91] and more recently by Yorkgitis.[88]. The slope of the curve yields $K_s$, the apparent shear modulus, but further work is required to analyze this parameter as well. Both RE and Ka are dependent on the distance of the probe from the surface, which is discussed in the next section.

Figure S3.1 shows $P_s$ for PMMA coatings having several thicknesses. Probe distance from the surface, which is discussed in the next section, was 3 mm. As might be expected for a polymer glass with a $T_g$ that is 125 °C above the test temperature, no dependence of $P_s$ on thickness is observed. These measurements provide an opportunity to assess accuracy. As a mechanical property measurement, peak removal force must be influenced by flaws at the ice-substrate interface, such as bubbles, cracks and topological deviations. For 32 measurements shown in Figure S3.1, the average value for $P_s$ is 354 ± 85 kPa.

Ice removal tests were carried out at probe speeds from 0.25 to 0.2 mm/s and a probe distance of 3 mm (Figure S3.2). There is no discernible dependence of $P_s$ on probe speed in this range. For 21 measurements shown in Figure S3.2, the average value for $P_s$ is 338 ± 80 kPa

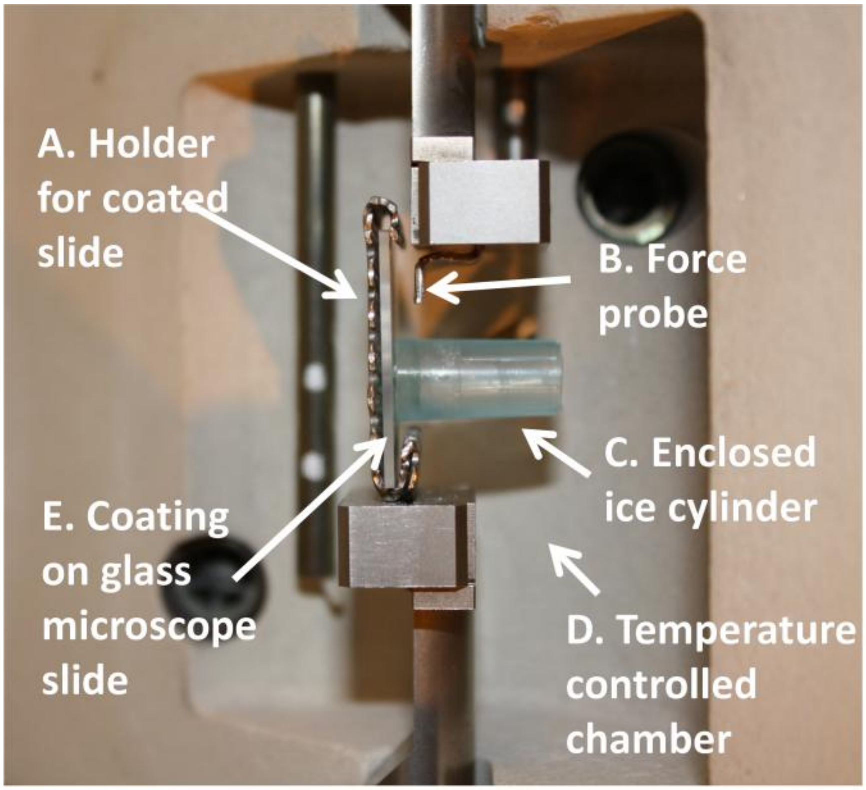

**Figure 3.3.** Ice adhesion test assembly.

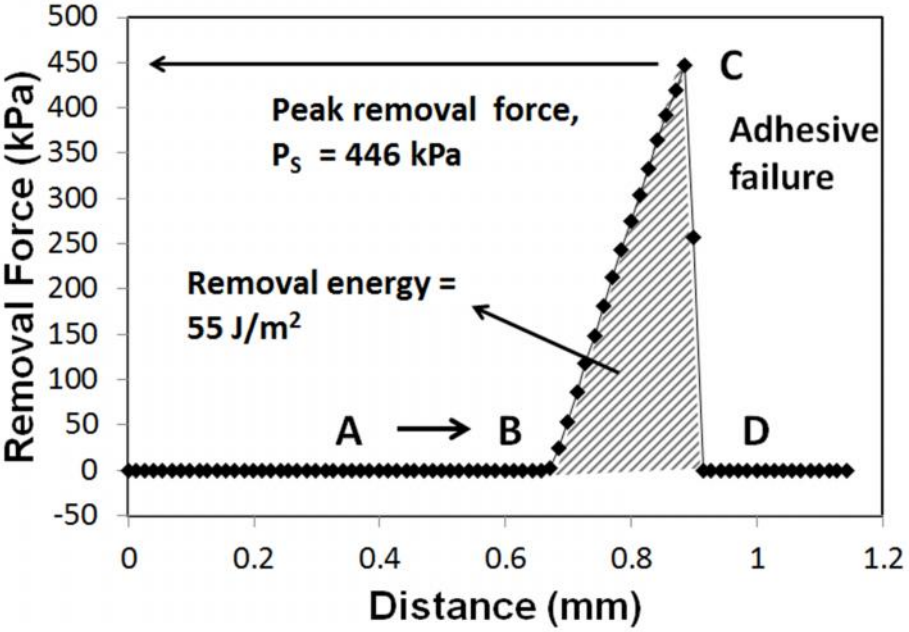

**Figure 3.4.** Representative test for ice removal: $P_S$, peak removal force (kPa); RE, removal energy (J/m$^2$). Rq, 12 nm; probe distance, 2 mm.

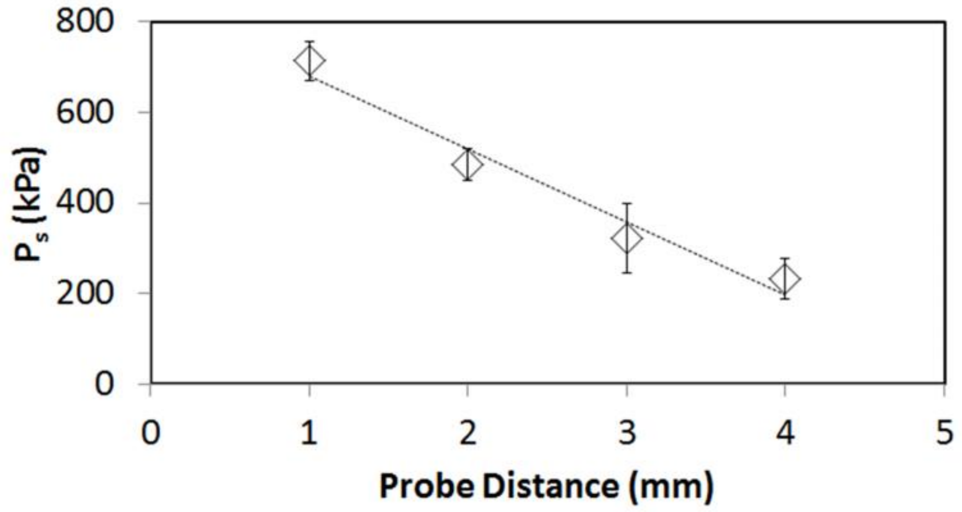

**Figure 3.5.** The dependence of $P_s$ on probe distance from the surface for a 15 μm PMMA coating with $R_q$ 12 nm; data in Table S3.1, Supporting Information.

*3.3.4. Probe distance from surface.* The test for adhesion described herein is meant to remove the ice cylinder in shear, which requires a close approach of the probe to the surface. In exploring test variables, the dependence of $P_s$ on probe distance from the surface has been examined. The steel probe thickness is ~0.7 mm. Two force probe geometries were used as shown in Figure S3.3. For 1 and 2 mm probe distances, a 20° angle was built into the probe Figure S3.3A. This geometry precluded any portion of the probe contacting the PMMA coating. For 3 and 4 mm probe distances, a probe with a curved tip was used. The center of the probe was used to calculate probe distance (Figure S3.3B). To change either probe distance, a shim was put in place between the upper grip and the probe.

Figure 3.5 shows the dependence of probe distance from the surface for ice release tests on a 15 μm PMMA coating with $R_q$ 12 nm. A nearly linear relationship is found between $P_s$ and probe distance. $P_s$ is greater than 700 kPa for the 1 mm probe but drops to ~200 kPa for the 4 mm probe distance. The decrease of peak removal force with increasing distance of the probe from the surface indicates an increasing contribution of removal of ice in tensile mode, as illustrated in Figure 3.6.

As noted above, PMMA was chosen to compare results to a previous study by Meuler with a custom designed apparatus.[1] Processing and test procedures described by Meuler and those employed in this work are summarized in Table 3.1. Sample preparation reported by Meuler was carried out by spin coating 200-300 nm films on a steel disks.[1] According to the Supplemental Information, the root-mean square roughness $R_q$ of the steel disk, which was determined by profilometry with a 10 μm stylus, was 0.85 ±0.04 μm (850 nm). Of note, $R_q$ was about the same after deposition of various films by spin coating including PMMA, 0.85 ± 0.06 μm.

With a probe distance of 2 mm, $P_s$ for a PMMA coating with $R_q$ 12 nm is 480 ± 35 kPa (Figures 3.1, 3.7 and Table 3.1). This result may be compared to 463 ± 65 kPa reported by Meuler from an average of 11 tests also utilizing a 2 mm probe distance.[1] The differences in coating preparation, roughness, ice geometry and test procedure are noted in Table 3.1. Of importance, with a probe distance of 2 mm, the results for peak removal force for ice release with the TA RSA-3 test and the custom apparatus reported by Meuler are the same within experimental error despite the difference in roughness discussed in the next section.

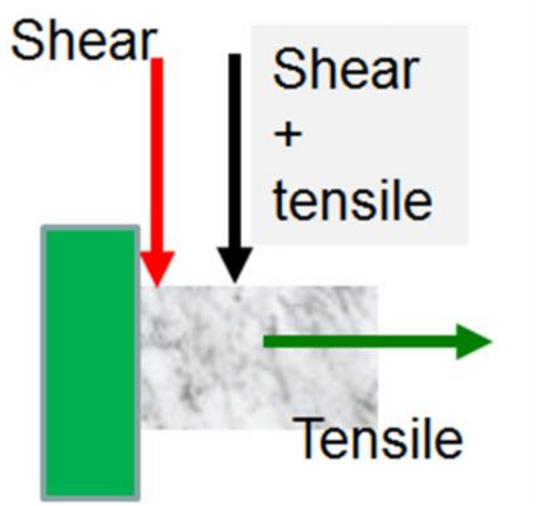

**Figure 3.6.** Illustration of probe force: shear, mixed, and tensile modes.

**Table 3.1.** A summary of PMMA sample preparation and processing and experimental procedures from Meuler[1] and this work.

| | **Cited ref** | **This work** |
|---|---|---|
| Solvent | Asahiklin AK-225, 100% HCFC-225 | THF |
| Processing | Solvent removal at ambient | 60 °C for solvent removal / annealing |
| Coating thickness | 200-300 nm | Tens of microns |
| Roughness ($R_q$) | 850 nm[a] | Varied (4-600 nm)[b] |
| Contact angles | Syringe drop in / out | Dynamic contact angles |
| Ice Geometry | Square column | Cylinder |
| Probe position | Horizontal | Vertical |
| $P_s$, 2 mm probe distance | 463 ± 65 kPa,<br>$R_q$ = 850 nm[a] | 480 ± 35 kPa,<br>$R_q$ = 12 nm[b] |

a. From profilometry (10 μm stylus).

b. From AFM, 80 x 80 μm scan.

*3.3.5. Roughness.* There is an extensive literature on the relationship of roughness to adhesion including theory at the nanoscale,[102-104] and experimental studies in diverse areas including micromachining[105] and bacterial[106] and cell adhesion. The effect of roughness on adhesion is dependent on the nature of the substrate and the roughness profile.[103]

Previous studies showed ice adhesion strength increases with increasing surface roughness.[101,107-108] However, Persson noted that the effect of roughness on adhesion is dependent on the roughness profile.[103] In view of the similar peak removal forces for PMMA with Rq 850 nm.[1] and our solvent cast PMMA (~10 nm, *vida infra*) we set about making PMMA coatings with varied roughness for ice adhesion tests.

The usual solvent removal process that we employ for obtaining coatings is slow evaporation in the presence of solvent vapor. PMMA coatings prepared in this manner typically have root mean square roughnesses ~10 nm (Figure 3.7B). Figure 3.7 shows surface topology of PMMA coatings changed depending on the solvent evaporation process. Drying at 60 °C on a hot plate generated smooth surfaces with negligible microscale imperfections (Figure 3.7A) while solvent removal in an open air environment had peaks and pits with various dimensions (Figure 3.7C).

The differences in surface topology are reflected by $R_q$, which is low for coatings dried at 60 °C on a hot plate (4 nm), higher for drying in closed environment (12 nm) and highest for solvent removal in air (23 nm). Imperfections are seen including micro-pits (3D, section analyses) that are likely due to solvent evaporation, nano-peaks (3D, section analyses), and signs of hardness inhomogeneity in the phase image.

To increase roughness coatings were heated above $T_g$ and embossed with ordinary white office paper or sandpaper using a press. Although not ideal, these roughened surfaces were used for a preliminary study of roughness on ice adhesion. Figure 3.7D and 3.9E show 80 x 80 TM-AFM images for two areas of resulting coatings that were selected for ice adhesion tests. These test surfaces had Rq's of 200 and 600 nm, respectively. It is important to note the z axis scale for 3D images in Figure 3.7 changes from 300 nm (**A**, **B**, **C**) to 5000 nm for **D** and **E**. Similarly, the z axis scale changes from 300 nm (**A**, **B**, **C**) to 1000 nm (**D**, **E**) for section analyses.

Figure 3.8 shows $P_s$ (kPa) as a function of surface roughness ($R_{q,}$) from 4 - 600 nm with a probe distance of 2 mm. Table S3.1 lists $R_q$, $P_s$, and standard deviations. $P_s$ increases with increasing $R_q$ from 4 to 600 nm. The increase in $P_s$ is ~50% over this Rq range, but standard deviations are high particularly for PMMA with Rq's of 4, 200, and 600 nm. Increased ice adhesion with increased roughness agrees with previous studies.[97,101,107-108] This result is easily understood as a consequence of increased surface areas and asperities at the ice-polymer interface. Asperities act to reinforce interfacial ice and increase adhesion.

The PMMA nanofilms reported by Meuler have an $R_q$ that is similar to the steel substrate (850 nm).[1] The peak removal force in shear with a probe distance of 2 mm was 463 ± 65 kPa (Table 3.1). In the present work, a similar $P_s$ was observed for PMMA having $R_q$ 12 nm ($P_s$ = 480 ± 35 kPa). Increasing roughness to a level approaching that reported by Meuler resulted in a 50% increase in peak removal force ($P_s$ = 625 ± 245 kPa).

Roughness for Meuler PMMA was high (Rq 850 nm) but fairly uniform with the average maximum height of the profile, Rz = 3.5 ± 0.3 μm. Although comparable topological images are not available, we conclude that the roughness profile must be important in determining $P_s$ in shear, as pointed out by Persson.[103] That is, a small area fraction of large asperities such as those seen for PMMA with Rq 600 nm (Figure 3.7E) may act to reinforce the ice-substrate interface and play a strong role in increasing adhesion. This proposition will remain as speculation until a careful study of the relationship of topology to peak removal force is carried out. Such a study would parallel that reported by McCarthy for effects of topographical length scales on wettability.[109]

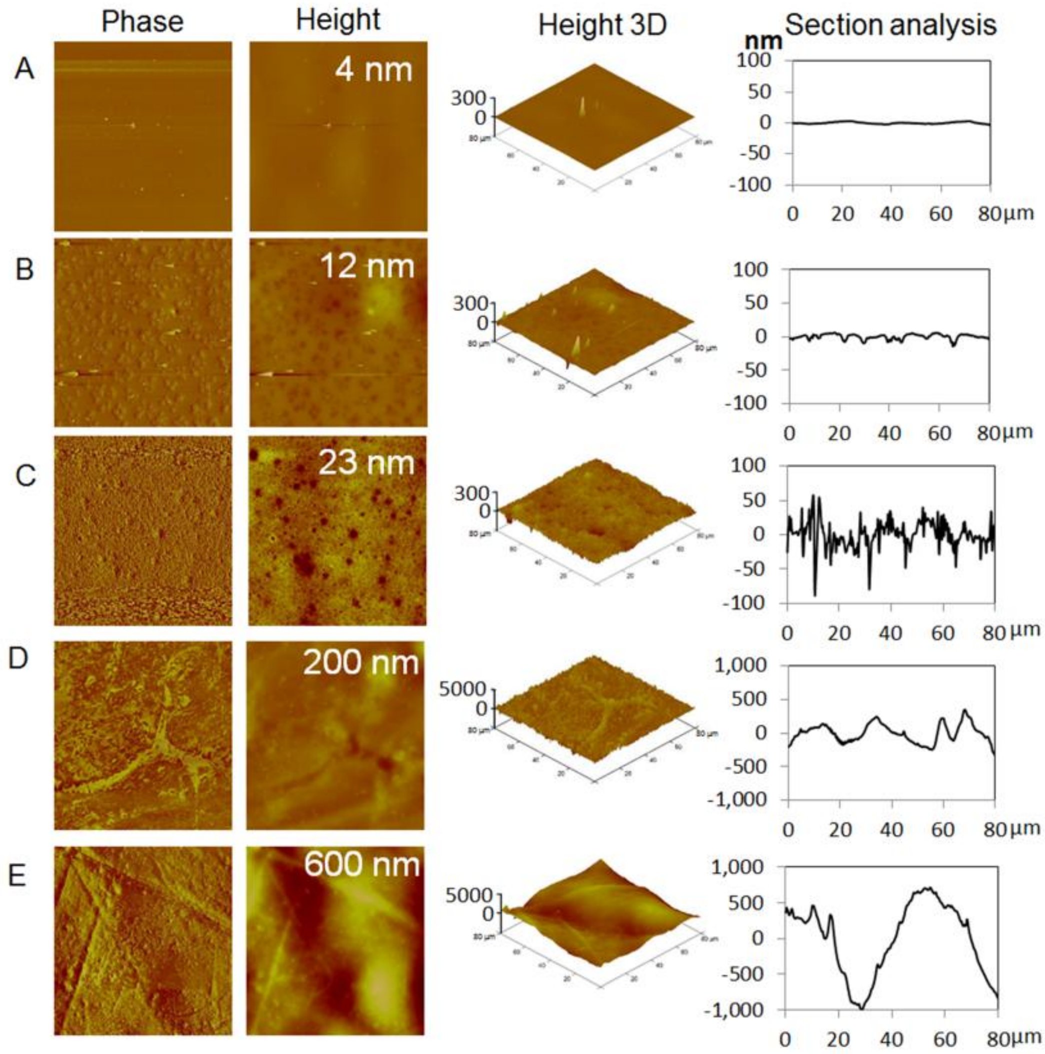

**Figure 3.7.** Typical 80 x 80 μm AFM images for solvent cast 15 μm thick PMMA coatings dried as follows: **A**, on 60 °C hot plate; **B**, in closed environment and **C**, in open environment. **D**, embossed with ordinary white office paper; **E**, embossed with sand paper (600 grit). $R_q$ is shown in 2D height images; for 3D height images the z axis scale changes from 300 nm (**A**, **B**, **C**) to 5000 nm (**D**, **E)**. The z axis scale changes from 100 nm (**A, B, C**) to 1000 nm (**D, E**) for section analyses.

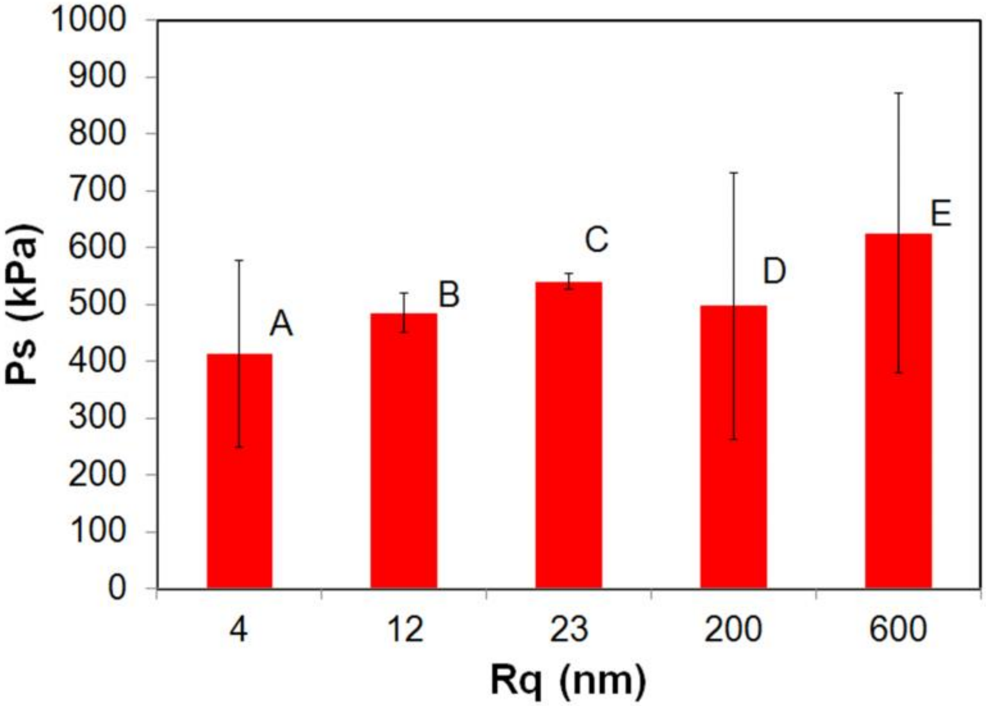

**Figure 3.8.** $P_s$ (kPa) as a function of surface roughness (2 mm probe distance, $R_q$, 2D AFM, 80 x 80 μm): **A – C**, solvent cast; **D**, **E**, heat / embossed; data in Table S3.2, Supporting Information.

*3.3.6. Contact Angles.* Ice adhesion strength has been correlated with the practical work of adhesion, $1 + \cos \theta_{rec}$, where $\theta_{rec}$ is the receding contact angle for water.[1,86] DCA force distance curves for PMMA are shown in Figure 3.9. Rq for this dip coated coverslip is similar to that for drip coated microscope slides (~ 10 nm). Contact angles were independent of cycle: $\theta_{adv}$, 78°; $\theta_{rec}$, 56°. These contact angles are comparable to those reported by Meuler, $\theta_{adv} = 83.6°$ and $\theta_{rec} = 60.7°$.[1] This good agreement is surprising considering the difference in roughness noted above.

Many contact angle studies on PMMA have been carried out, but information on effects of roughness on $\theta_{rec}$ is sparse, as sessile drop contact angles are usually reported.[110-111] On smooth PMMA surfaces, an extensive study by Erbil gave a 54-64° range for $\theta_{rec}$.[112] Based on this range, which includes $\theta_{rec}$ for coatings reported herein (Rq 10 nm) and those reported previously (850 nm),[1] we conclude that the factor of ~85 in roughness does not significantly affect contact angles or contact angle hysteresis. This finding is attributed to PMMA being a moderately wettable surface ($\theta_{adv} < 90°$) and to restricted long range mobility due to high molecular weight and high $T_g$.

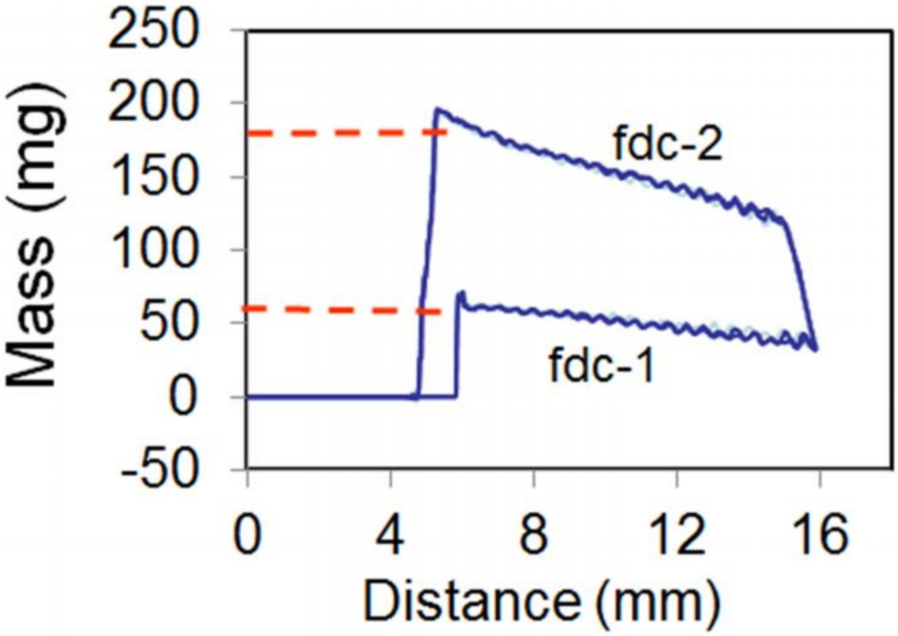

**Figure 3.9.** DCA force distance curve for PMMA.

## 3.4. Conclusions.

The principle accomplishment described herein is the development of a laboratory test for determining strength of ice adhesion with a commercially available instrument. The procedure adapts a test previously described for a study of adhesion of epoxy cylinders (ECs) to RARE, rigid adherent resistant elastomers.[2] The significance for development of this ice adhesion test method is that construction of specialized equipment used in all prior studies of ice adhesion is not necessary.

The new method was applied to ice adhesion measurements on the polymer glass PMMA. This polymer was chosen for comparison with a previous study by Meuler with a custom designed apparatus.[1] The most important result from PMMA ice adhesion tests was the finding that $P_s$, the peak removal force, is strongly dependent on the distance of the probe from the surface. Thus, in reporting $P_s$ for ice adhesion by this method, the probe distance must be specified. In using this test to develop coatings that have easy ice release, a reference coating must be selected and the ratio of $P_s$ for reference and sample used as a metric. Such a ratio has been used in engineering studies that employ custom built equipment for ice release testing.[85-87,113-115] A case can be made for using PMMA as a reference due to ready availability, ease of preparation of nano-smooth coatings, thickness independence of $P_s$, and poor ice release characteristics.

Previous studies showed increased roughness resulted in increased ice adhesion.[97,101,107-108] Everyday experience such as sanding before painting makes improved adhesion to a roughened surface commonly accepted. With a probe distance of 3 mm, increasing $R_q$ from 4 - 600 nm lead to an increase of 50% in $P_s$ (Figure 3.8). This trend is ascribed to increased surface area and to an increased area fraction of asperities at the ice-polymer interface that reinforce ice and increase adhesion.

On the other hand, the PMMA nanofilms reported by Meuler had a $P_s$ of 463 ± 65 kPa (Table 3.1) with an $R_q$ of 850 nm.[1] With the same 2 mm probe distance a similar $P_s$ was observed for $R_q$ 12 nm ($P_s$ = 480 ± 35 kPa). Increasing roughness to a level approaching that reported by Meuler resulted in a 50% increase in peak removal force ($P_s$ = 625 ± 245 kPa). Some combination of different methods for determination of roughness (AFM vs. profilometry), different roughness profiles, or low measurement accuracies apparently account for the disagreement for $P_s$ on rough PMMA surfaces.

The test described herein is not rigorous compared to tests based on fracture mechanics utilizing specialized equipment such as those developed by Chaudhury[116-119] and Andrews.[84,91] However, if the distance of the force probe from the surface is carefully controlled, our new test provides a relative measure of ice adhesion strength. As such, this test is useful for our ongoing research aimed at clarifying the relationship of roughness to ice adhesion and to the development of coatings with low ice adhesion. In parallel to the development of coatings that easily release ice, future research is aimed at more precise control of probe distance so as to improve measurement accuracy.

## 3.5. Supplemental information

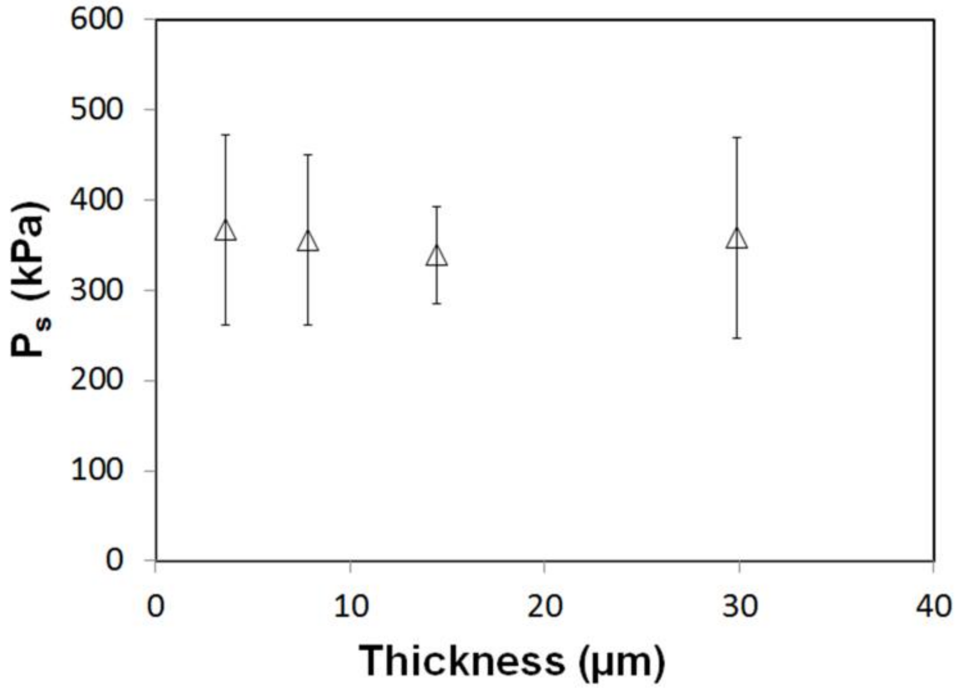

**Figure S3.1.** Ice peak removal force (Ps) for as a function of coating thickness, probe distance, 3 mm.

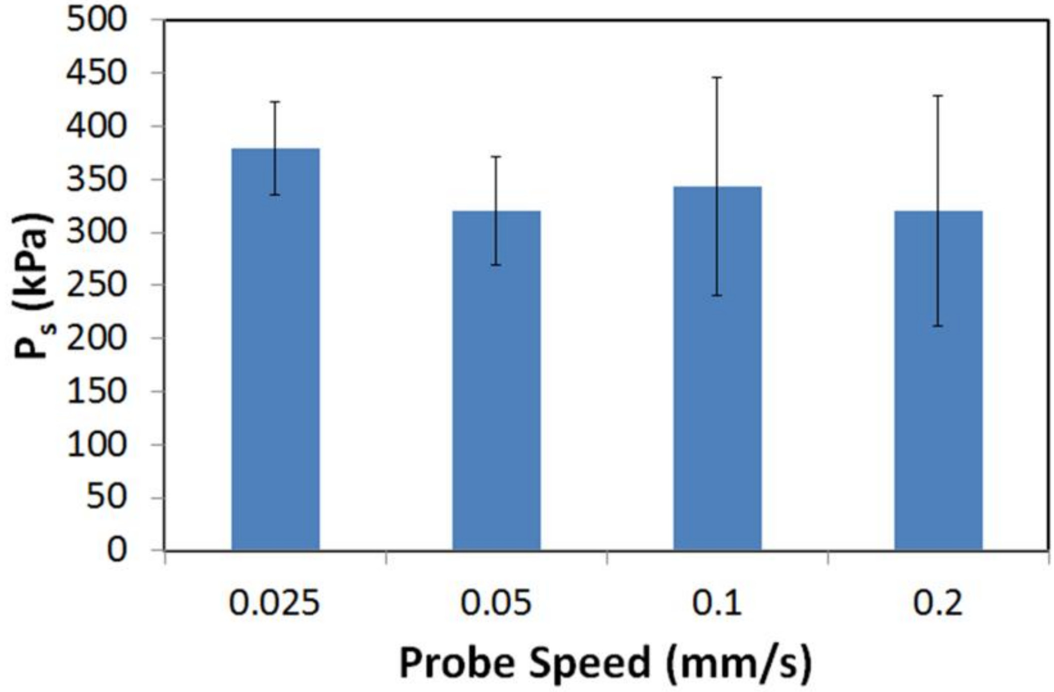

**Figure S3.2.** Ice peak removal force for PMMA as a function of probe speed.

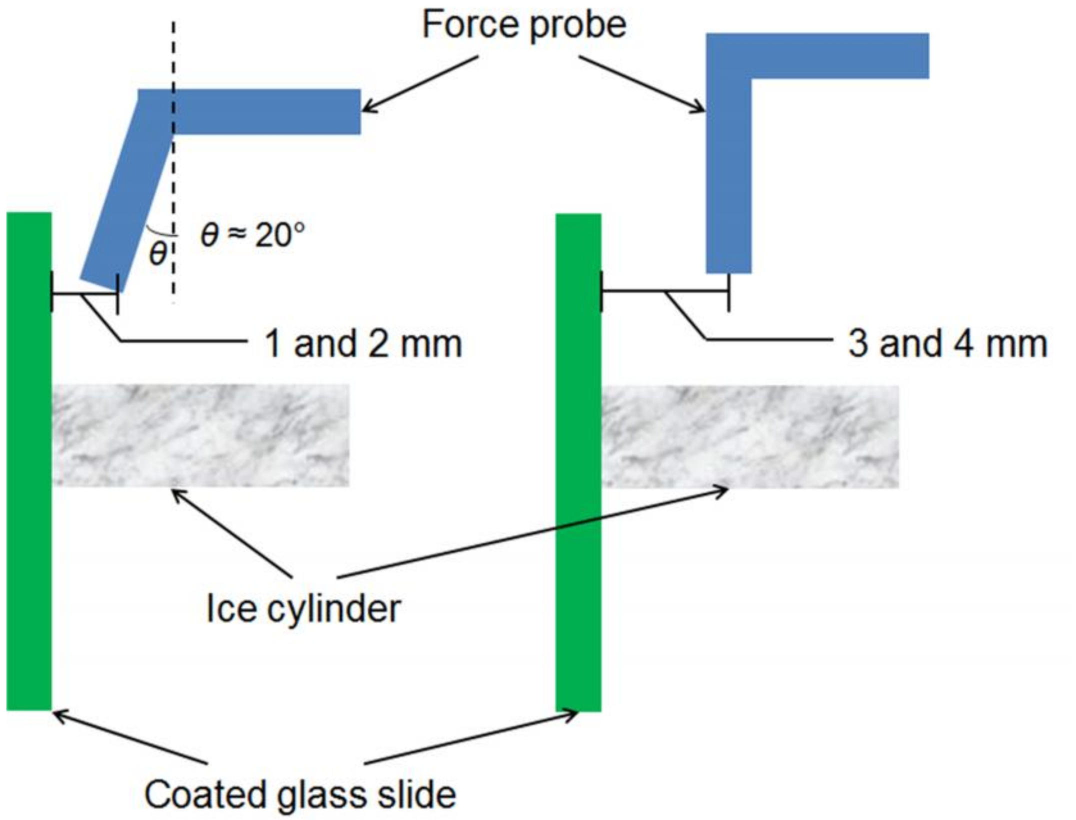

**Figure S3.3.** Probe geometries.

**Table S3.1.** The dependence of $P_s$ on probe distance from the surface for a 15 μm PMMA coating with $R_q$ 12 nm (data for Figure 3.7).

| Probe distance (mm) | $P_s$, (kPa) | Number of tests | s.d.[b] |
|---|---|---|---|
| 1 | 714 | 5 | 45 |
| 2 | 485 | 3 | 35 |
| 3 | 321 | 15 | 77 |
| 4 | 232 | 10 | 44 |
| | | | |

a. From 2D AFM, 80 x 80 μm scan.
b. Number of trials in parentheses.

**Table S3.2.** $R_q$, $P_s$, and standard deviation for the Figure 3.6 bar graph.

| $R_q$ (nm)[a] | $P_s$, (kPa) | Number of tests | s.d. |
|---|---|---|---|
| 4 | 412 | 5 | 164 |
| 12 | 485 | 3 | 35 |
| 23 | 540 | 3 | 14 |
| 200 | 498 | 3 | 234 |
| 600 | 624 | 4 | 246 |

a. From 2D AFM, 80 x 80 μm scan.

# Thickness dependence and modeling of ice removal stress for a polydimethylsiloxane nanocomposite: Sylgard 184

## 4.1. Introduction

Wide ranging problems associated with ice accumulation for wind turbine blades, offshore structures employed in oil exploration and energy infrastructure including electric wires have been noted in previous studies of ice adhesion.[1,83-84,86-87,120-121] Deadly accidents, material loss, reduced performance and interference with normal operations are often encountered due to icing. For critical applications such as aircraft, de-icing methods include energy inefficient electric heating and time consuming application of de-icing fluids, which are environmentally problematic. Icing and associated problems, such as downed power lines seem to be simply accepted as an inescapable part of the winter season. However, consideration of the consequences of icing makes clear that the development of economical coatings from which ice can be removed easily would have broad applications impacting safety and reliability of low temperature operations. Such coatings should decrease ice adhesive strength to less than ~100 kPa (14.5 psi) so that ice is removed by natural forces, such as wind, gravity or vibration or a combination thereof.[122]

A reliable test for ice release is of importance for understanding fundamental factors affecting adhesion. Several designs for custom built ice release test equipment have been employed for quantitative assessment of ice release. Usually, ice removal stress in shear is determined using a force probe as described over three decades ago by Jelenick.[83] Force probe equipment has also been built and applied by Croutch[120] and by Meuler.[1]

A test method based on removal of ice accumulation by centrifugal force has been used by specialized centers. Typically, cooled water droplets are sprayed onto a substrate to form ice followed by increasing rotational speed and measurement of ice removal stress upon release.[90,123] Alternatively, the relative strength of ice adhesion can be determined based on ice mass and rotation speed. An “ice adhesion reduction factor” is then used employing a reference material.[87] A fundamental approach for the determination of ice adhesion characteristics based on fracture mechanics was developed by Andrews and Lockington.[84,91] This test employed a thin flexible plastic disk to form a pre-crack between ice and the test surface. In those cases where the mode of release was entirely or nearly entirely interfacial, adhesion energy ( $\Xi$ ) was calculated.

Rather than custom built equipment, we recently described a laboratory method for evaluating ice adhesion using a commercially available instrument normally used for dynamic mechanical analysis (TA RSA-3).[124] This method utilizes a probe for removal of an ice cylinder and the determination of peak removal force ($P_s$). Initially, the strength of ice adhesion to poly(methyl methacrylate) was investigated. The distance of the force probe from the PMMA surface was identified as a critical variable for the determination of $P_s$. This outcome is implemented in the work described herein.

Several groups have sought correlations for ice adhesion and basic materials parameters. Cohen and Farzenha emphasized the correlation of ice adhesion with the practical work of adhesion or $[1 + \cos \theta_{rec}]$.[1] That is, ice adhesion was correlated with the scaling parameter $[1 + \cos \theta_{rec}]$ for liquid water, which meant that “icephobicity of nominally smooth surfaces can be predicted simply by measuring the receding contact angle for water droplets on the substrate”.[1]

Yorgitis stressed a correlation of sessile drop contact angles or surface free energy in determining ice adhesion.[121] This group used the Andrews/Lockinton test[84,91] and found an increase the ice adhesion strength/parameter and a change in fracture from adhesive to cohesive after subjecting polypropylene to air / corona oxidation. The ice adhesion parameter increased from 0.72 to 3.42 after corona treatment, a factor of 4.75. In parallel, the sessile drop contact angle for biaxially oriented PP was 108° but 77° after corona treatment. The surface free energy correlation was supported by these results.

Coating thickness has also been reported to affect ice adhesion strength on elastomers. For a polyurethane, Andrews reported that the failure energy decreased as coating thickness increased.[84,91] Yorgitis reported ice adhesion studies on an unfilled, platinum cured vinyl polysiloxane resin crosslinked with poly(methylhydro)siloxane.[121] Although cohesive failure was common for these weak, unfilled elastomers, ice removal energy ( $\Xi$ ) decreased from 1.16 $J/m^2$ to 0.12 $J/m^2$ with increasing coating thickness.

While silicones have often been investigated for ice release coatings, a broad range of values for ice adhesion strength has been reported. As noted above, Yorgitis studied a Pt cured silicone and in addition to ice removal energy ( $\Xi$ ) reported a remarkably low peak removal force of 20– 28 kPa, which was obtained by an unspecified independent laboratory.[121] Wang, et al., found a shear ice adhesion strength of 55 kPa for a Pt cured silicone with ~27 wt% $SiO_2$ nano-filler; $P_s$ dropped below 40 kPa after addition of 20 wt% silicone oil.[122] The ice adhesion strength of a room-temperature vulcanized (RTV) silicone coating was ~190 kPa according to Kulinich.[115] Sylgard 184 is a commercially available (Dow Corning), Pt cured silicone elastomer. Coatings are prepared from a two parts comprised of a base resin and curing agent. Sylgard 184 coatings have been the subject of two studies concerning ice adhesion. For a spin coated Sylgard 184 thin film, Cohen found an average strength of ice adhesion of 291 ± 44 kPa.[1] Recently, Petit studied the mechanism of frost growth on cast plaques (1 mm) of Sylgard 184.[125] Coatings with decreasing stiffness were prepared by increasing the ratio of base resin to curing agent. These coatings or thin plaques were used to investigate frost formation from condensed supercooled liquid droplets.

From the above, silicone coatings and thin films have often been the subject of studies for ice formation and adhesion. The range of ice adhesion strength for silicones reflects different compositions, surface roughness, test conditions and other parameters. In beginning a systematic study, we have selected Sylgard 184 and have employed our recently reported ice release test method based on commercially available instrumentation. Our results emphasize the importance of elastomer thickness as a variable in the determination of the removal force for ice. We correlate the thickness dependence of $P_s$ with theory developed by Kendall over four decades ago.[36]

## 4.2. Experimental

*4.2.1. Coating preparation.* A Sylgard 184 kit was purchased from Dow Corning. In a typical coating preparation, base (10 g) and curing agent (1 g) were put in a 50 g capacity Flacktek screw top container. The container was placed in a Speed Mixer-DAC 150FV (Flacktek Inc., Landrum SC) followed by high speed (HS) mixing at 3500 rpm for 60 sec. This HS process was repeated 2 times to obtain a thoroughly homogeneous, bubble-free, pre-cured resin. As shown in Table 4.1, thin coatings (12 – 150 µm) were created by spin coating (SPS SPIN150). Microscope glass slides (75 × 25 mm) were drip coated with ~ 0.6 g of pre-cured mixture, and then were spun at 6000, 4000, 2000, 1000 and 500 rpm to generate coating thicknesses of 12, 18, 29, 73 and 143 µm, respectively. Making coatings thinner than 12 µm was precluded by difficulties associated with holding the slide on the stage at high rpm. Microscope glass slides were drip coated with 0.5, 1 and 1.5 g of pre-cured mixture to obtain the coatings thicknesses of 266, 533 and 800 μm. Coatings were cured at 60 °C overnight followed by 100 °C in a vacuum oven for 3 d. Coatings were optically transparent and bubble free. An initial step reported by some investigators that utilized high vacuum to remove bubbles was not required.[126]

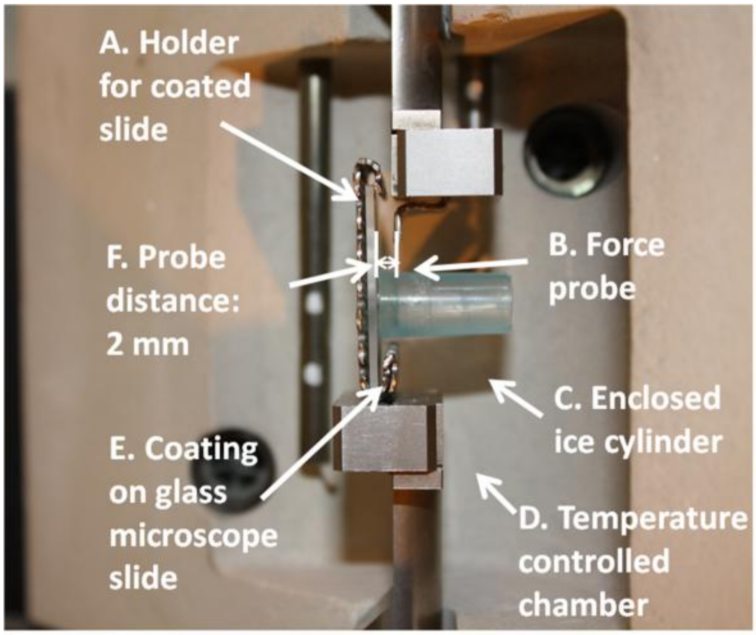

**Figure 4.1.** Ice adhesion test assembly.

*4.2.2. Ice release test.* A TA Instruments RSA-3 was adapted for the ice release test. This test has been described in detail previously. [124] The range of motion for the upper grips (~10 mm), the 3.5 kg load cell and the temperature controlled chamber are critical elements for this test. A force probe and a sample holder were fitted into the upper and lower grips as shown in Figure 4.1. Ice cylinders were formed on coating surfaces at -15°C by using plastic molds.[124] The force probe does not engage the ice cylinder directly but rather the mold that contains the ice (Figure 4.1C). The distance between force probe and coating surface was held constant at 2 mm. Tests described herein were conducted at -10 °C, with the force probe speed of 0.5 mm/s.

*4.2.3. Differential Scanning Calorimetry.* A TA-Q 1000 (TA instruments) temperature Modulated Differential Scanning Calorimetry (MDSC) was used for determination of thermal transitions at a heating rate of 3 °C /min. and ± 0.5 ºC modulation at 60 s.

*4.2.4. Thermogravimetric Analysis*. TGA was carried out using a Pyris 1 TGA (Perkin Elmer) under $N_2$ atmosphere at heating rates of 20 °C/min from 50 °C to 300 °C, 3 °C/min from 300 °C to 600 °C and 20 °C/min from 600 °C to 700 °C.

*4.2.5. Tapping Mode Atomic Force Microscopy (TM-AFM).* A Dimension Nanoscope V (originally Digital Instruments, then Veeco) atomic force microscope was used for morphological and topological analysis of the coated surfaces. Tapping mode used silicon crystal cantilevers (40 N/m). Imaging was done at both soft and hard tapping by altering the setpoint ratio $r_{sp}$ or $A_{exp} / A_o$ from 0.95 to 0.6, where $A_o$ is free oscillation amplitude and $A_{exp}$ is the experimental oscillation amplitude. Images with scan sizes of 10 µm were taken to probe microscale and nanoscale morphology of the coated surfaces.

**Table 4.1.** Coating preparation methods and resulting thicknesses.

| Sample No. | Coating method | Spin rate (RPM) | Coating net weight (g) | Thickness (µm) |
|---|---|---|---|---|
| 1 | Spin | 6000 | 0.023 | 12 |
| 2 |  | 4000 | 0.034 | 18 |
| 3 |  | 2000 | 0.054 | 29 |
| 4 |  | 1000 | 0.138 | 73 |
| 5 |  | 500 | 0.269 | 143 |
| 6 | Drip | N/A | 0.5 | 266 |
| 7 |  |  | 1 | 533 |
| 8 |  |  | 1.5 | 800 |

*4.2.6. Contact angles*. Water drop image profiles and associated contact angles and were obtained by using a Ramé-Hart goniometer equipped with a camera. Advancing and receding contact angles were measured as water was supplied via a syringe into ($\theta_{adv}$) or from ($\theta_{rec}$) sessile drops. Contact angles were calculated using Drop Image software (version 1.4.11). The reported value is an average obtained from 3 drops with 5 measurements per drop.

## 4.3. Results and Discussion

In our first report of a laboratory test for ice adhesion, we chose PMMA as a test substrate.[124] The glass transition temperature for PMMA is ~110 °C higher than the ice removal test. This test case may be described as removal of a rigid object (ice) from a rigid substrate (a glass). To broaden understanding of ice adhesion, the present study focuses on removal of ice from an elastomer. As such, this is conceptually related to a prior investigation that described removal of a rigid object (an epoxied aluminum cylinder) from a fluorous elastomer.[2] For the present study, Sylgard 184 was chosen as a readily available silicone elastomer that has been the subject of several adhesion studies.[38,124,126-128]

*4.3.1. Polymer coatings.* Sylgard 184 coatings were prepared according to the manufacturer’s protocol. A high speed mixer was used to assure homogeneous distribution of crosslinker and Pt catalyst. Coatings were cured at 60 °C overnight followed by 100 °C in a vacuum oven for 3 d. The resulting coatings were bubble free and optically transparent.

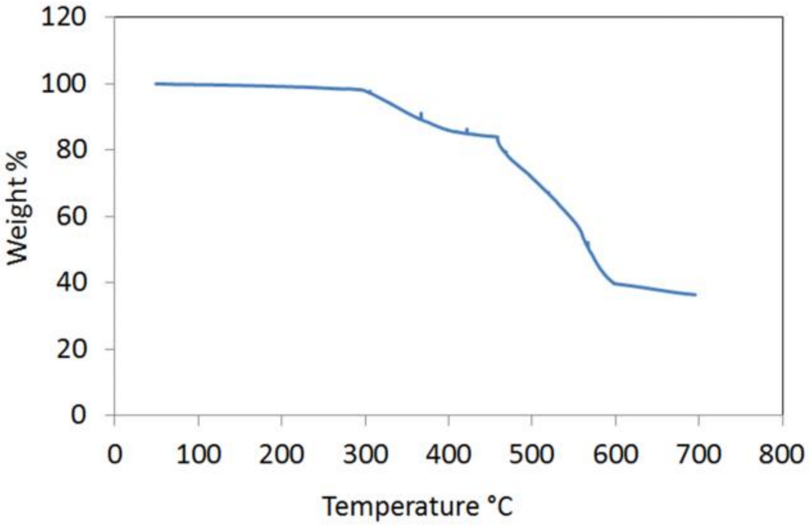

**Figure 4.2.** TGA for Sylgard 184.

*4.3.2. Thermogravimetric analysis.* Unfilled PDMS typically has a high mass loss at elevated temperatures due to depolymerization to cyclics, while inorganic fillers retard mass loss. Thus at 700 °C Xu, et al., found a mass loss for unfilled PDMS of ~95% and ~70 % for 25 wt% $SiO_2$ filled PDMS.[129] TGA for Sylgard 184 showed a mass loss of 64% after heating from ambient to 700 °C. (Figure 4.2) The retention of 36 wt% mass at 700 °C and information from the product data safety sheet suggests a silica nano-particle content of ~30 wt%.

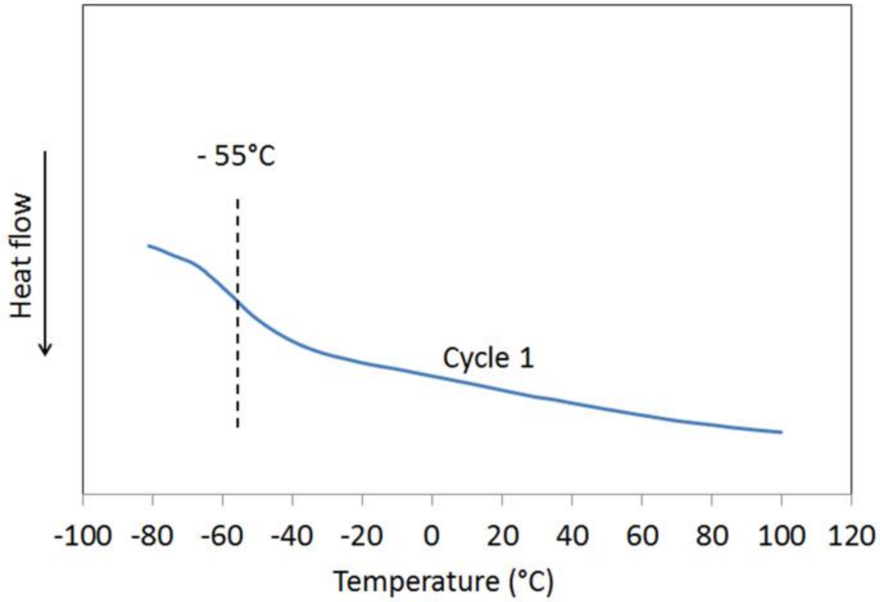

**Figure 4.3.** DSC for Sylgard 184.

*4.3.3. Differential scanning calorimetry.* A broad $T_g$ for Sylgard 184 was observed at -55 °C (Figure 4.3). Presumably, a lower temperature $T_g$ also occurs in the vicinity of -110°C, but at present, our instrumentation has a low temperature limit of ~ -90 °C. A more detailed study is planned using DMA to establish whether the -55 °C $T_g$ results from association of a portion of PDMS chains with nano-silica filler. In any event, ice release tests reported herein were carried out at a - 10 °C at which Sylgard 184 may be considered a prototypical elastomer in a rubbery state.[93]

*4.3.4. Contact angles*. Previously, Meuler found that ice adhesion strength could be correlated with the practical work of adhesion, 1 + cos $\theta_{rec}$, where $\theta_{rec}$ is the receding contact angle for water.[1] To obtain wetting behavior for coatings described herein, sessile drop contact angles were obtained. A typical set of water drop images for Sylgard 184 coatings cured as described in the Experimental Section is shown in Figure 4.4. The thickest (800 µm) and the thinest coating (12 µm) were selected for contact angle measurements. $\theta_{adv}$ is comparable to that reported previously (109°), but $\theta_{rec}$ is 58°, about 34° lower. Table S4.1 in Supporting Information notes differences in processing, coating thickness and rugosity that preclude a direct comparison of results. Of particular note is Rq for coatings reported herein (~5 nm, 100 x 100 µm, 2D AFM image) while an Rq of 850 nm was reported previously by Mueler using profilimetry.[1]

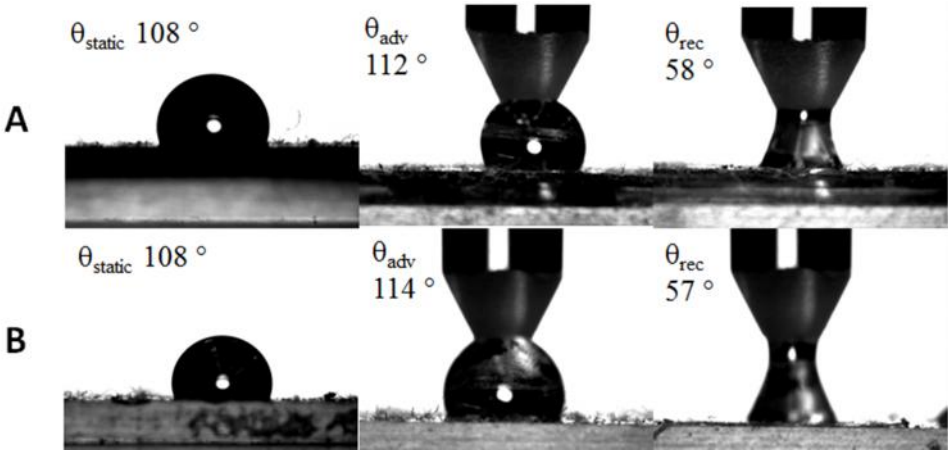

**Figure 4.4.** Contact angle measurements for Sylgard 184 coatings with thicknesses **A**, 800 µm and **B**, 12 µm.

*4.3.5. Ice removal test.* Figure 4.1 shows the experimental setup including the sample holder, the force probe and a coated glass slide. To generate the ice cylinder, a section (~ 2 cm) is cut from the top of a micropipette tip. The cylinder is place on the sample and 200 μL water is added. Surface tension holds the water in the cylinder and no leakage from the water / cylinder / sample interface is encountered. The air space above the water in the cylinder confines the water during ice formation and allows vertical expansion. The inner diameter of the container tube is the outer diameter of the ice cylinder as there is no visible ice formation beneath the cylinder wall. This diameter is used to calculate the interfacial area. For measurements described below, a chamber temperature of -10 °C was employed. Previously, we showed that $P_s$ decreased as the distance of the probe from the sample increased. For measurements herein, a probe distance of 2 mm was chosen. This distance is the closest approach that assures no probe contact with the coating surface.

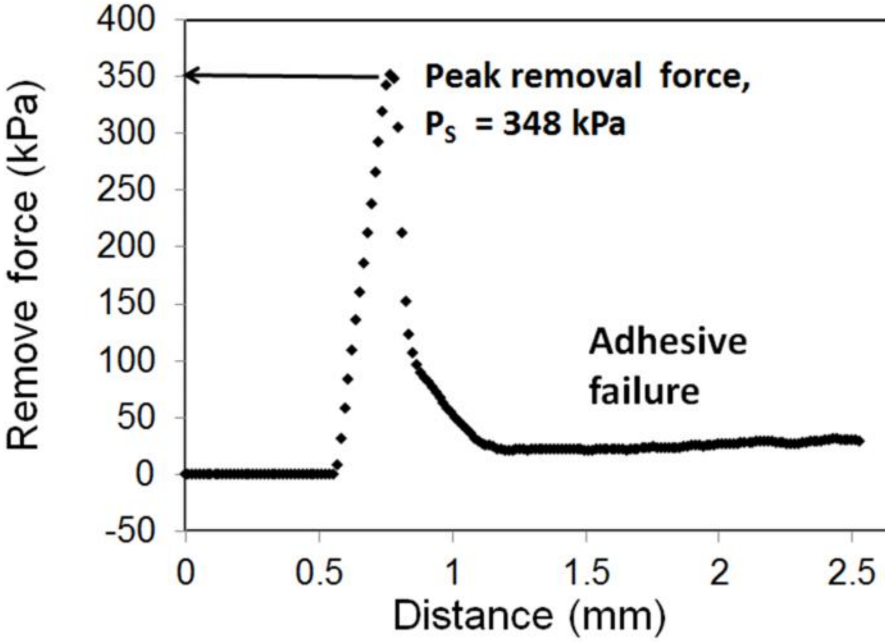

**Figure 4.5.** A representative force *vs*. distance curve for a Sylgard 184 coating of 29 µm.

Figure 4.5 shows a force vs. distance curve for a representative ice removal test. At ~ 0.5 mm the probe touches the tube containing the ice cylinder. A linear force distance curve is observed up to the point of ice release that is associated with $P_s$, the peak removal force in shear (kPa). However, pure shear is not achieved for this test. This point is clear from the dependence of $P_s$ on probe distance found previously for PMMA.[124] Preliminary tests showed a higher $P_s$ for a probe distance of 1 mm. However, as noted above, concern about the probe touching the coating resulted in the compromise probe distance of 2 mm.

The test illustrated in Figure 4.6 shows that removal force drops markedly after the release point. Unlike PMMA coatings investigated earlier,[124] a precipitous drop to baseline (zero force) does not usually occur. While adhesive failure is evident with no ice remnants visible after tests, an immediate return to zero force is found for only ~20% of tests. That is, a shoulder corresponding to slippage is found for most tests. The reason for this weak residual adhesion is under study.

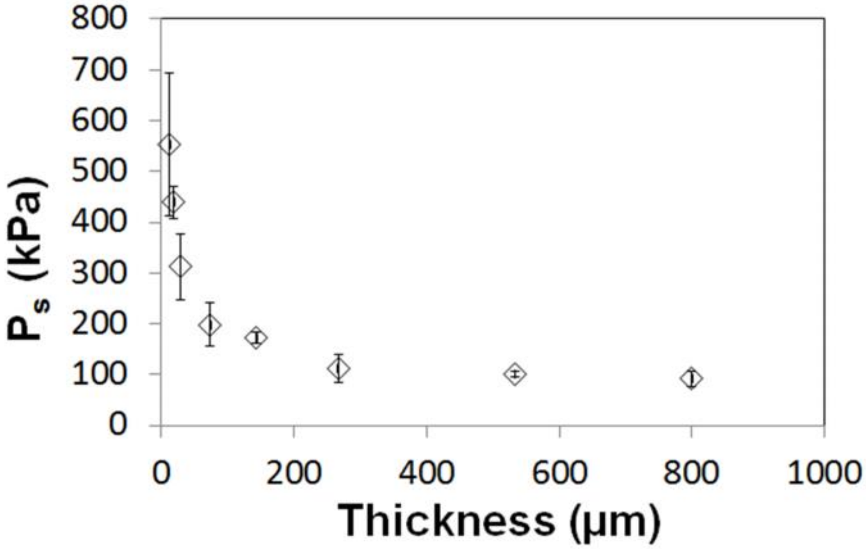

**Figure 4.6.** Peak removal force in shear ($P_s$) as a function of coating thickness.

*4.3.6. Thickness dependence for peak removal force.* Coatings having different thicknesses were made by a combination of spin and drip coating (Table 4.1). Figure 4.6 shows $P_s$ as a function of coating thickness. Values for $P_s$ and standard deviations may be found in Supporting Information (Table S4.2). For thin coatings (~ 10 μm) $P_s$ is ~ 550 kPa but for thick coatings (~800 μm) $P_s$ decreases to ~ 100 kPa. The large error bar for the thin coating (12 μm, 553 ±149 kPa) is due to the relatively high peak removal force being near the limit for the load cell. Thicker coatings have relatively small error bars that testify to the accuracy of the test.

The 5.5 times reduction in $P_s$ demonstrates the importance of thickness in the determination of ice removal strength. This result is similar to Yorgitis' finding for an unfilled Pt cured silicone.[121]

$$P_c \propto \pi a^2 \left( \frac{2 w_a K}{t} \right)^{1/2} \qquad \text{Eq. 1}$$

*4.3.7. Modeling ice adhesion.* Over 40 years ago, Kendall developed a theory (Eq. 1) for removing a solid from an elastomeric substrate. The result was a correlation of the force required to remove a rigid cylinder ($P_c$) with work of adhesion ($w_a$), modulus ($K$) thickness (t), and radius (a).[36] Kendall's theory applied to removal of a rigid object from an elastomer in tensile mode. However, tensile and shear modulus are related by the relationship $K_{tensile} = 3K_{shear}$.[78] By analogy, a similar relationship can therefore be applied to removal that is mostly in shear ($P_s$, Eq. 2). By keeping the probe distance constant (2 mm) and as close to the surface as practical, non-shear contributions are thought to be minimized and approximately constant.

$$P_s \propto \pi a^2 \left( \frac{2 w_a K}{t} \right)^{1/2} \qquad \text{Eq. 2}$$

From dynamic mechanical analysis, the modulus of Sylgard 184 at -10 ºC is ~10 MPa.[130] At ambient temperature, contact angle analysis shows $\theta_{rec}$ is ~58º for the processing conditions employed herein. Modulus and work of adhesion ($1 + \cos \theta_{rec}$) are therefore constant under the test conditions employed. The Kendall criteria for detachment of a rigid cylinder bonded to an elastomeric substrate provides a test for the influence of coating thickness on $P_s$.

Over the coating thickness range examined a nearly linear correlation is found between $P_s$ and $1/t^{1/2}$ (Figure 4.7). This finding demonstrates the quantitative relationship between ice removal stress and thickness for Sylgard 184 elastomeric coatings. The slope for $P_s$ vs. $1/t^{1/2}$ provides a measure of the extent of thickness dependence ($1.8 \times 10^3$ kPa / $\mu m^{-1/2}$).

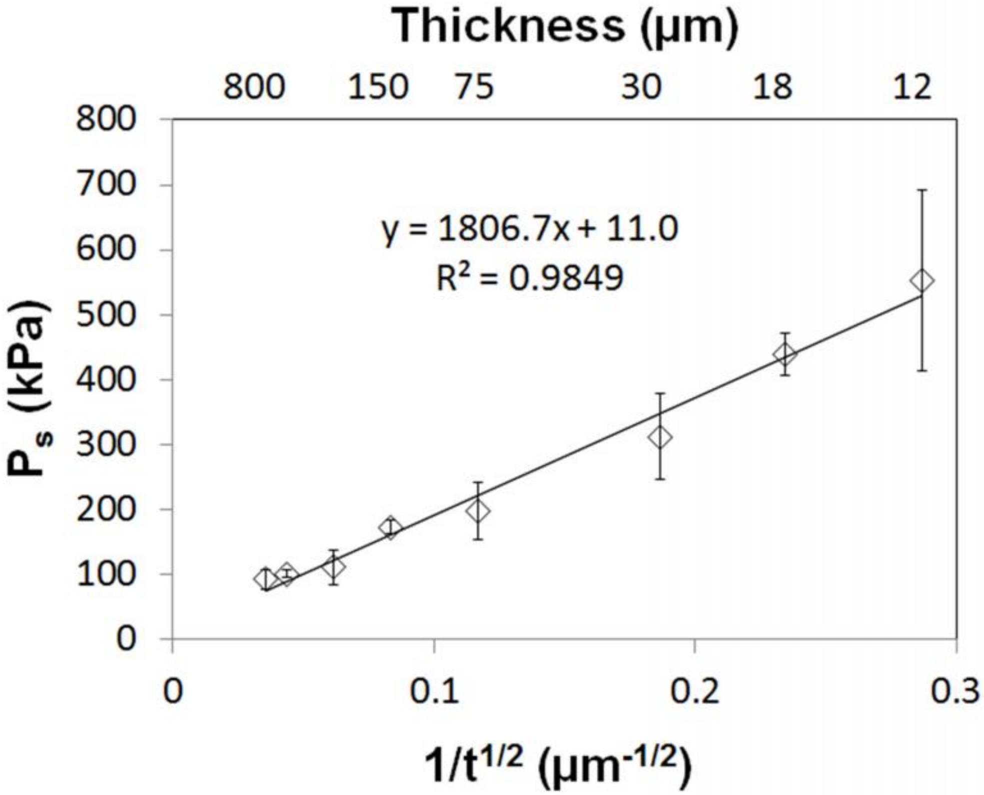

**Figure 4.7.** Ice adhesion ($P_s$, kPa) as a function of $1/t^{1/2}$.

*4.3.8. A generalized model for ice adhesion*. The Kendall criteria apply to elastomers with low modulus. In contrast, $P_s$ for PMMA, a prototypical glass with $T_g > 110$ °C above the test temperature (-10 ºC) was independent of thickness. Herein, a model is proposed for the removal of ice from an elastomer compared to a rigid substrate such as PMMA, which has a modulus of ~ 3 GPa. This model takes into account the higher modulus of ice (~ 10 GPa),[131] which is about 1000 times higher than typical elastomers (10 MPa).

The large difference in moduli for ice and soft surfaces results in a mismatch in strain under stress when a force acts to remove ice. For a rubbery or “soft” coating stress cannot be evenly distributed but builds up at the interface. The concentrated stress at the interface provides a path for easy ice release. The concepts described above form the basis of a new model that acknowledges the contribution of surface energy to minimizing adhesion (nanosurface noted above) while including the contribution from the relative stiffness of ice and the coating surface to adhesion. The length scale for coating stiffness can be from mesoscale to microscale.

Eq. 2 shows a dependence of adhesion strength on modulus and thickness. Above it was noted that a mismatch in modulus leads to stress building up at the interface. The thickness term is important because thicker coatings facilitate larger vertical displacements that lead to building up stress at the frontier point or line rather than a plane, as illustrated in Figure 4.8.

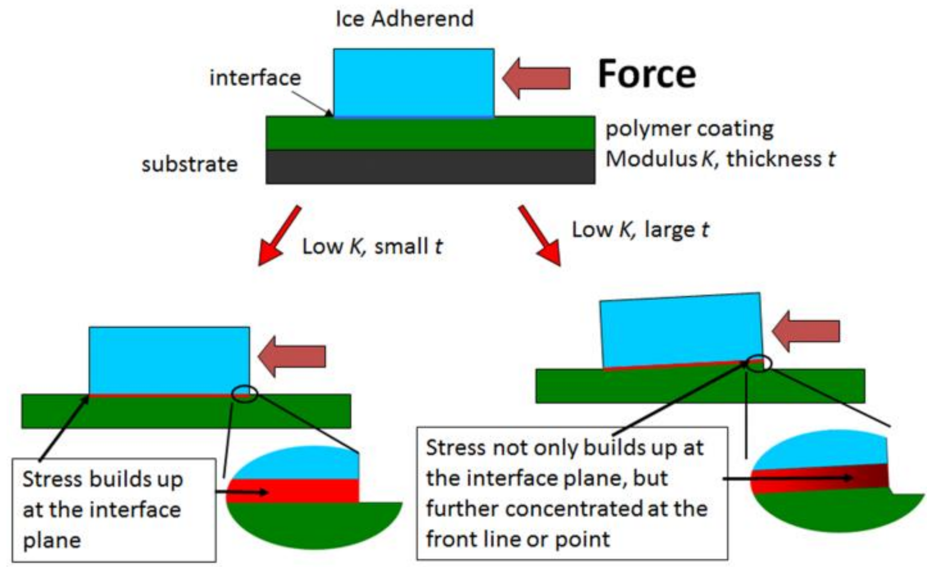

**Figure 4.8.** Schematic diagram demonstration of stress building up at the interface plane and/or the front line or point during removal of a rigid, bonded object (ice) from a soft coating.

Removal of ice from rigid substrates may also be considered in the context of Eq 2. For example, Yorgkitis studied ice release from polypropylene (PP), which has a $T_m$ of 160 °C. If it is assumed that plasma treatment does not affect modulus, $P_s$ is independent of thickness (rigid, like PMMA), and the removal force for ice is only determined by the interfacial free energy or $w_a$.[121] As noted earlier, an increase the ice adhesion strength/parameter and a change in fracture from adhesive to cohesive after subjecting polypropylene to air / corona oxidation. The ice adhesion parameter increased from 0.72 to 3.42 after corona treatment, a factor of 4.75. Only a sessile drop contact angle (CA) is reported (not $\theta_{rec}$) but the trend is clear as the CA dropped from 108° to 77° after corona treatment. Clearly, work of adhesion, which is equivalent to surface free energy, correlates these results.

It is important to consider the relationship developed by Cohen and Farzenha,[1]Kulinich and Farzaneh,[115] and by Dotan et al.[132]. This work emphasized the connection of ice adhesion with the practical work of adhesion or $[1 + \cos \theta_{rec}]$. That is, ice adhesion was correlated with the scaling parameter $[1 + \cos \theta_{rec}]$ for liquid water. This correlation is appropriate for rigid substrates where $P_s$ is independent of thickness and modulus. However, the inclusion of test results for elastomeric Sylgard 184 and the correlation of $P_s$ with $w_a$ is clearly not warranted. The peak removal force of 291 ± 44 kPa for Sylgard 184 reported by Cohen happens to lie near the correlation line for rigid substrates apparently due coating thinness ( ~0.3 μm). This is not clear as roughness ($R_q$) was high (0.7 μm).[1]

## 4.4. Conclusion.

The work described herein is part of continuing research on correlating ice release from polymer surfaces with fundamental parameters including physical state, work of adhesion, modulus, thickness and non-intrinsic parameters such as roughness. Guided by experimental parameters used for testing PMMA, ice release tests for Sylgard 184 elastomeric coatings were carried out. Probe distance was 2 mm at the test temperature (-10 °C). Because $P_s$ is sensitive to probe distance, a reference coating would be advantageous. The ratio of $P_s$ for reference and sample would then be a useful metric. Such a ratio has been used in engineering studies that employ custom built equipment for ice release testing.[86-87,115,120,133-134] One objective of future work is the identification of a convenient standard.

In contrast to glassy PMMA, which showed negligible coating thickness dependence for ice adhesion strength, coating thickness dependence was observed for elastomeric Sylgard 184. $P_s$ decreased by a factor of 5.5 (550 to 100 kPa) with coating thickness increasing from 12 μm to 800 μm. These results support those of Yorgitis, who reported ice adhesion studies on an unfilled, platinum cured vinyl polysiloxane resin crosslinked with poly(methylhydro) siloxane.[121] Although cohesive failure was common for these weak, unfilled elastomers, ice removal energy ( $\Xi$ ) decreased by a factor of 8 from 1.16 $J/m^2$ to 0.12 $J/m^2$ with decreasing coating thickness.

Importantly, a linear correlation between $P_s$ and $1/t^{1/2}$ is found for ice release from Sylgard 184 coatings (Figure 6) validating a theory developed by Kendall 40 years ago. Based on these results, a generalized model is proposed for the removal of ice from low modulus elastomers (~10 MPa).

The test described herein is not rigorous compared to those based on fracture mechanics reported by Chaudhury[135-138] and Andrews.[84,91] However, if probe distance is controlled, a relative measure of ice adhesion strength can be established easily using commercially available instrumentation. As such, this test is useful for ongoing research aimed at clarifying the relationship of roughness to ice adhesion and to the development of coatings with low ice adhesion.

## 4.5. Supplemental Information.

**Table S4.1.** A summary of Sylgard 184 sample preparation and processing and experimental procedures from Meuler[a] and this work.

| | **Cited ref[a]** | **This work** |
|---|---|---|
| Solvent | Asahiklin AK-225, 100% HCFC-225 | No solvent |
| Processing | Heated for ~2 h at 60 °C | Heated for overnight at 60 °C, followed by 3 d at 100 °C, vacuum. |
| Coating thickness | 200-300 nm | 12-800 µm |
| Roughness | 850 nm[b] | ~ 5 nm[c] |
| Ice Geometry | Square column | Cylinder |
| Probe position | Horizontal | Vertical |
| $\theta_{adv}$, water | 109 | 113 |
| $\theta_{rec}$, water | 92 | 57 |

a. Meuler, A. J.; Smith, J. D.; Varanasi, K. K.; Mabry, J. M.; McKiney, G. H.; Cohen, R. E. *ACS Appl. Mater. Interfaces* **2010**, *2*, 3100.

b. From profilometry (10 µm stylus).

c. From AFM, 100 x 100 µm scan.

**Table S4.2**. $P_s$, and standard deviation for the Figure 4.6.

| Coating thickness (μm) | $P_s$, (kPa) | Standard deviation (kPa) |
|---|---|---|
| 12 | 553 | 139 |
| 18 | 439 | 33 |
| 29 | 313 | 65 |
| 73 | 198 | 43 |
| 143 | 173 | 11 |
| 266 | 112 | 27 |
| 533 | 101 | 6 |
| 800 | 93 | 15 |

# CHAPTER 5

## Conclusions

Minimizing adhesion of ice has been the subject of extensive studies because of importance to applications such aircraft wings, spacecraft and power transmission wires. The work described here describes progress for coatings and ice release test method development over the last few years. Major achievements include:

(1) New Rigid Adherent-Resistant Elastomers (RARE)
(2) A new Epoxied Cylinder (EC) adhesion test
(3) Validation of an ice release test, and
(4) Study of ice adhesion strength on coating thickness for a PDMS elastomer.

### 5.1. New Rigid Adherent-Resistant Elastomers (RARE)

New Rigid Adherent-Resistant Elastomers (RARE) were discussed in Chapter 2. RARE coatings are comprised of 3F **1** terminated with triethoxysilane moieties and linear 3F polyurethane (U-3F). Hybrid compositions U-3F-x are designated by polyurethane weight percent "x". Interestingly, spectroscopic studies revealed that RARE coatings spontaneously "self-stratify" during coating deposition and cure. Cured RARE coatings are comprised of (1) a nanoscale surface layer with very low work of adhesion, (2) a low modulus mesoscale and (3) a strong bulk, where "mesoscale" is defined as a near surface region with a depth less than 1000 nm.

Bulk and surface characterization together with adhesion measurements have established U-3F-x coatings, and U-3F-50 in particular, as new fluorous rigid adherent-resistant elastomers

(RARE) that are tough, hydrocarbon resistant, and optically transparent. The principle findings are:

(1) Increased bulk mechanical properties, particularly toughness, with increasing U-3F wt% (Figures 2.3, 2.4 and Table 2.2)

(2) Mesosurface (to ~1000 nm) U-3F depletion from ATR-IR spectroscopy with Ge and diamond crystals

(3) A test for peak removal force $P_{c\text{-}s}$ using a sample holder for a microscope slide in conjunction with a commercially available TA RSA-3 instrument; integration software that provides removal energy (RE).

(4) A striking compositional dependence for peak removal force $P_{c\text{-}s}$ and RE for a rigid bonded object (EC), and

(5) An optimized combination of $P_{c\text{-}s}$ and RE for the U-3F-50 hybrid coating by standards of high bulk toughness (6.2 MPa) and minimum peak removal force (0.078 MPa).

As noted earlier, most published research on RARE $P_c$ concerns poly(dimethylsiloxane) based coatings. The combination of toughness and low EC adhesion for the U-3F-50 hybrid coating with the advantage of resistance to hydrocarbon solvents meets or exceeds the performance of PDMS systems noted above. Finally, the U-3F-50 hybrid elastomers compare favorably with PDMS polyurethane networks reported by Webster.[5,13]

### 5.2. A new Epoxied Cylinder (EC) adhesion test

An EC adhesion test was devised by using a commercially available TA RSA-3 instrument. The TA RSA-3 is well suited for these tests as the 3.5 kg load cell facilitates accurate measurements. This test gives *peak* force ($P_s$) for EC removal. To our knowledge, $P_s$

measurements with the TA RSA-3 are the first utilizing a commercial instrument. Prior measurements have been obtained with manual gauges[3] or custom built devices.[4-6] A striking compositional dependence was found for EC adhesion. A "RARE" U-3F-50 hybrid coating had the lowest adhesion ($P_s$ = 0.078 MPa) with good toughness (6.2 MPa).

### 5.3. Validation of an ice release test

As discussed in Chapter 3, a laboratory test method for evaluating ice adhesion was developed employing the same instrument as that used for Epoxied Cylinder (EC) adhesion test, the TA RSA-3. This is the first laboratory ice adhesion test that does not require a custom built apparatus. The temperature controlled chamber is an enabling feature that is essential for the test. The method involves removal of an ice cylinder from a polymer coating with a probe and the determination of peak removal force ($P_s$). To validate the test method, the strength of ice adhesion was determined for a prototypical glassy polymer, poly(methyl methacrylate), PMMA. For PMMA, the distance of the probe from the PMMA surface and surface roughness have been identified as two critical variables for $P_s$. The new test provides a readily available platform for investigating fundamental surface characteristics affecting ice adhesion. The significance for development of this ice adhesion test method is that construction of specialized equipment used in all prior studies of ice adhesion is not necessary.

### 5.4. Study of ice adhesion strength on coating thickness for a PDMS elastomer

The work described in Chapter 4 is part of continuing research on correlating ice release from polymer surfaces with fundamental parameters including physical state, work of adhesion, modulus, thickness and non-intrinsic parameters such as roughness. In contrast to glassy PMMA, which showed negligible coating thickness dependence for ice adhesion strength, strong coating thickness dependence was observed for Sylgard 184, a filled polydimethylsiloxane elastomer. A correlation between ice adhesion and coating thickness (t) was found, that follows a theory developed over 40 years ago, a nearly linear relationship between peak removal stress ($P_s$) and $1/t^{1/2}$ was found. In particular, $P_s$ decreased from 550 kPa to 100 kPa with coating thickness increasing from 12 µm to 800 µm. While work of adhesion, which is related to surface free energy, is recognized as an important factor that can affect ice release, the results reported herein show that coating thickness can override this single parameter for elastomeric substrates. Base on the result, a general model is proposed for the removal of ice from low modulus elastomers (~10 MPa).

# CHAPTER 6

## Further Exploration

A laboratory test method for evaluating ice adhesion was developed employing the same instrument as that used for Epoxied Cylinder (EC) Adhesion test, the TA RSA-3. This is the first laboratory ice adhesion test that does not require a custom built apparatus. The temperature controlled chamber is an enabling feature that is essential for the test. The method involves removal of an ice cylinder from a polymer coating with a probe and the determination of peak removal force ($P_s$). To validate the test method, the strength of ice adhesion was determined for a prototypical glassy polymer, poly(methyl methacrylate) and a commercially available elastomeric silicone, Sylgard 184. For PMMA, the distance of the probe from the PMMA surface and surface roughness have been identified as two critical variables for $P_s$. Implementing this knowledge, probe distance was kept constant for Sylgard 184 tests. At a probe distance of 2 mm, coating thickness was found to be the most significant parameter in ice release test. The new test provides a readily available platform for investigating fundamental surface characteristics affecting ice adhesion.

### 6.1. Temperature dependence

Several parameters for ice release tests including probe distance, probe speed, coating roughness and coating thickness have been studied in this investigation. However, the effect of temperature is unclear due to the complexity of the temperature effect. Temperature may affect ice adhesion strength due to the following reasons: 1) coatings modulus may change with temperature; 2) the difference between thermal expansion coefficient of ice and that of coatings; and 3) unknown structural effects for ice at the coating / ice interface.

Temperature is important because it is a major factor influencing the modulus of polymers. According to Kendall's model,[36] adhesion strength is proportional to the square root of modulus for elastomers. Jellinek reported that ice adhesion increases with decreasing temperature (-2 °C to -20 °C) for polysiloxane / polycarbonate mixture with a $T_g$ of -20 °C. However, very little is known about the temperature dependence of ice adhesion. Thus, systematic studies of temperature dependence of ice adhesion are expected to be fruitful and to make an important contribution to fundamental understanding.

The difference between thermal expansion coefficient of ice and that of coatings may affect ice adhesion strength. According to literature, the coefficient of linear thermal expansion is ~50 ppm/°C for ice[139] at 0 to -40 °C, 310 ppm/°C for Sylgard 184[140] and 50 - 70 ppm/°C for PMMA[141]. Thus the coefficient of linear thermal expansion for ice is about 6 times lower than Sylgard 184 and 4 times lower than PMMA. The large differences in thermal expansion coefficient may cause physical cracks at the ice/coating interface and then decrease ice adhesion strength at low temperatures.

A recent study indicated superhydrophilic polyelectrolyte brush layers could decrease ice adhesion strength.[142] This is because the superhydrophilic polymer chains were believed to interrupt the crystallization or the association of ice molecules to a more ordered stage at the ice/coating interface. Thus the ice at ice/coating interface may be amorphous or less ordered at below zero temperature. This study suggested the exist of $T_g$ of ice at interface. A significant difference should be observed near $T_g$.

The control of temperature is an important capability for the TA RSA-3 instrument. Thus temperature dependence can be investigated relatively easily. Our preliminary study on PMMA showed clear temperature dependence for 3 mm probe, but this result was not observed for a 4 mm probe distance. As shown in Figure 5.1, ice removal force increased linearly with decreasing temperature (-10 °C to -40 °C) for 3 mm probe, while essentially no temperature dependence was observed for 4 mm probe. The temperature dependence for PMMA is surprising since differential scanning calorimetry (DSC) confirmed the well-known ($T_g$) of 115 °C for PMMA (MW 540 kDa). The reason for the different results shown in Figure 10 is not clear. The reproducibility of this result will be addressed in future work. In addition, this study will be expanded to include what is now our “standard” probe distance of 2 mm.

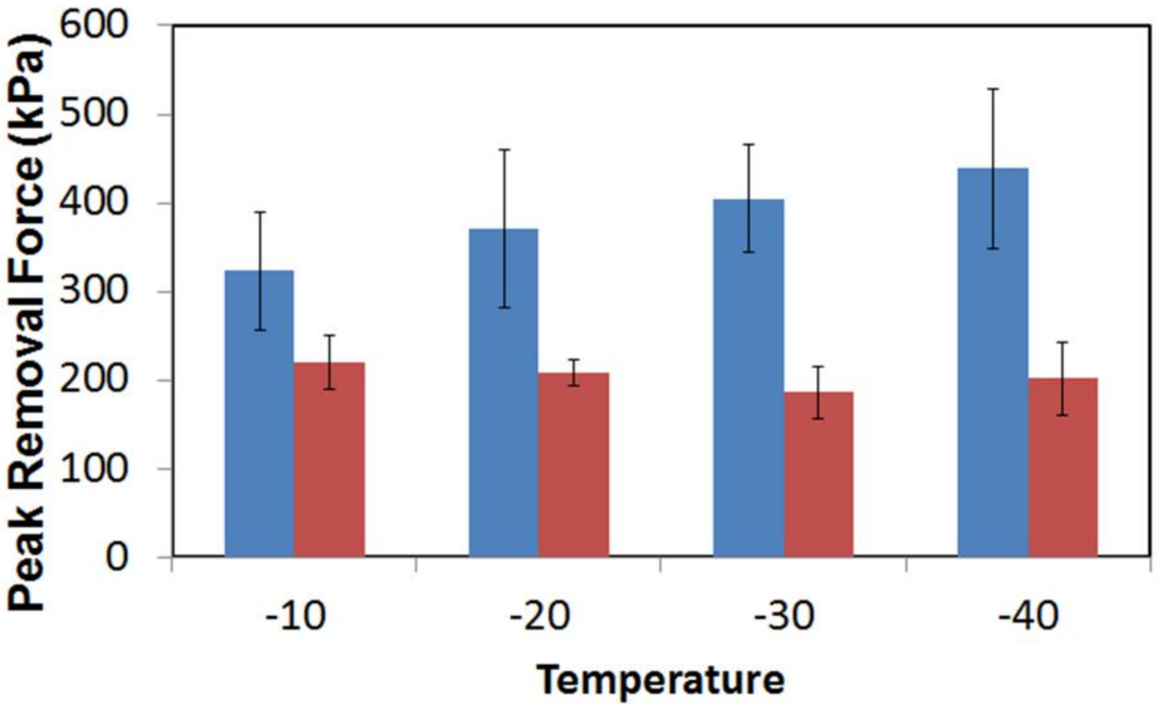

**Figure 5.1.** Peak removal force (kPa) as a function of temperature for **blue**, 3 mm probe and **red**, 4 mm probe. Coating material: PMMA.

A broad $T_g$ for Sylgard 184 was observed at -70 °C to -35 °C.[108] Thus it is reasonable to assume that the modulus of Sylgard 184 is affected by test temperature (-10 °C to -40 °C). As expected, the peak removal force for 75 μm coatings increased about linearly with decreasing temperature form –10 °C to -40 °C (Figure 5.2). However, our preliminary result suggested a different temperature dependence for thin coatings (12 μm). The peak removal force increased significantly from -10 °C to -20 °C, remained about the same level at -20 °C to -30 °C, and then decreased from -30 °C to -40 °C. The reason of the different behavior of thin coating and thick coating is not clear. An in-depth and systematic study is needed to generate a well-defined temperature dependence for Sylgard 184.  In addition, dynamic mechanical analysis (DMA) will be used to better define $T_g$ and to explore whether there may be two $T_g$'s, which may be associated with "free" and filler-associated domains.

Several parameters of ice release test, including probe distance, probe speed, coating roughness and coating thickness, have been studied in the present investigation, but the effect of temperature is unclear. Temperature dependence of ice adhesion will be a high priority for future studies.

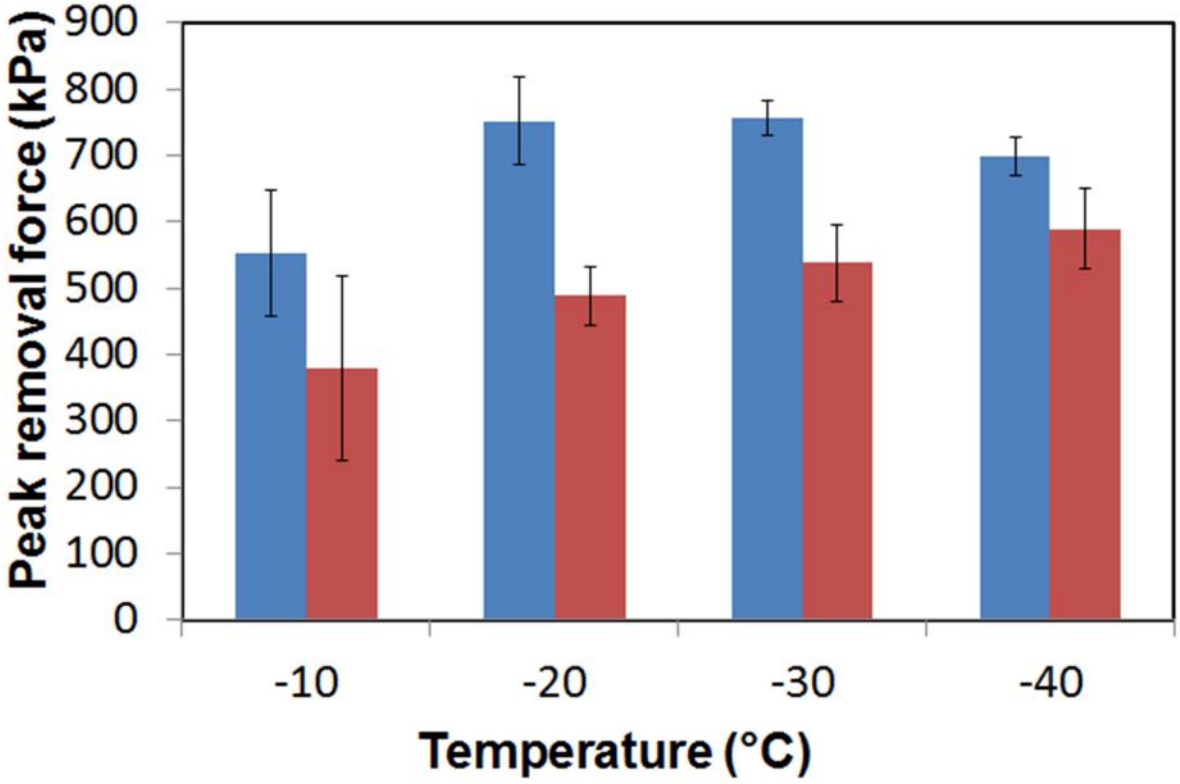

**Figure 5.2.** Peak removal force (kPa) as a function of temperature for **blue**, 12 µm and **red**, 75 µm coating thickness. Coating material: Sylgard 184.

### 6.2. Evaluate ice release property for Rigid Adhesion Resist Elastomer (RARE)

As described in Chapter 2, an epoxied aluminum cylinder (EC) adhesion test was developed to investigate release characteristics of Rigid Adhesion-Resistance Elastomers (RARE).[2] Cured RARE coatings are comprised of (1) a nanoscale surface layer with very low work of adhesion, (2) a low modulus mesoscale and (3) a strong bulk, where “mesoscale” is defined as a near surface region with a depth less than 1000 nm.[2] Epoxy Cylinder (EC) Adhesion testing was for RARE by using the commercially available instrument, TA RSA-3. A striking compositional dependence was found for EC adhesion. A U-3F-50 hybrid coating had the lowest adhesion ($P_s$ = 0.078 MPa) with good toughness (6.2 MPa). Due to the factor that U-3F-50 has shown superior anti-rigid adhesion properties, a good ice release property is expected for this material.

On the other hand, unlike the EC adhesion test, ice release test is done at low temperature. Low temperature will affect the physical property of RARE significantly. As mentioned in Chapter 2, $T_g$ is -45 °C for 3F-$SiO_{1.5}$ and -62 °C for U-3F-50. [2] This result suggests that the surface of U-3F-50 has a $T_g$ at between -45 °C and -62°C, which is close to the lowest test temperature (- 40 °C). Thus a significant increase of $P_s$ might be observed when test temperature is close to – 40 °C. An investigation of U-3F-50 will be interesting to discover whether ice release will be affected with decreasing temperature as the glass transition temperature is approached.

# REFERENCES

1. Meuler, A. J.; Smith, J. D.; Varanasi, K. K.; Mabry, J. M.; McKiney, G. H.; Cohen, R. E. Relationships between Water Wettability and Ice Adhesion. *ACS Applied Materials & Interfaces* **2010,** *2* (11), 3100-3110.

2. Chakrabarty, S.; Wang, C.; Zhang, W.; Wynne, K. J. Rigid Adherent-Resistant Elastomers (RARE): Nano-, Meso-, and Microscale Tuning of Hybrid Fluorous Polyoxetane-Polyurethane Blend Coatings. *Macromolecules* **2013,** *46* (8), 2984-2996.

3. Swain, G. W.; Schultz, M. P. The testing and evaluation of non-toxic antifouling coatings. *Biofouling* **1996,** *10* (1-3), 187-197.

4. Chisholm, B. J.; Webster, D. C.; Bennett, J. C.; Berry, M.; Christianson, D.; Kim, J.; Mayo, B.; Gubbins, N. Combinatorial materials research applied to the development of new surface coatings VII: An automated system for adhesion testing. *Review of Scientific Instruments* **2007,** *78* (7).

5. Ekin, A.; Webster, D. C. Combinatorial and high-throughput screening of the effect of siloxane composition on the surface properties of crosslinked siloxane-polyurethane coatings. *Journal of Combinatorial Chemistry* **2007,** *9* (1), 178-188.

6. Conlan, S. L.; Mutton, R. J.; Aldred, N.; Clare, A. S. Evaluation of a fully automated method to measure the critical removal stress of adult barnacles. *Biofouling* **2008,** *24* (6), 471-481.

7. Gruner, M. S.; Szilvay, G. R.; Berglin, M.; Lienemann, M.; Laaksonen, P.; Linder, M. B. Self-assembly of Class II Hydrophobins on Polar Surfaces. *Langmuir* **2012,** *28* (9), 4293-4300.

8. Zeiger, D. N.; Stafford, C. M.; Cheng, Y. J.; Leigh, S. D.; Lin-Gibson, S.; Lin, N. J. Effects of Sample Preparation on Bacterial Colonization of Polymers. *Langmuir* **2012,** *26* (4), 2659-2664.

9. Joy, A.; Cohen, D. M.; Luk, A.; Anim-Danso, E.; Chen, C.; Kohn, J. Control of Surface Chemistry, Substrate Stiffness, and Cell Function in a Novel Terpolymer Methacrylate Library. *Langmuir* **2011,** *27* (5), 1891-1899.

10. Brady, R. F.; Singer, I. L. Mechanical factors favoring release from fouling release coatings. *Biofouling* **2000,** *15* (1-3), 73-81.

11. Joshi, R. G.; Goel, A.; Mannari, V. M.; Finlay, J. A.; Callow, M. E.; Callow, J. A. Evaluating Fouling-Resistance and Fouling-Release Performance of Smart Polyurethane Surfaces: An Outlook for Efficient and Environmentally Benign Marine Coatings. *Journal of Applied Polymer Science* **2009,** *114* (6), 3693-3703.

12. Weinman, C. J.; Finlay, J. A.; Park, D.; Paik, M. Y.; Krishnan, S.; Sundaram, H. S.; Dimitriou, M.; Sohn, K. E.; Callow, M. E.; Callow, J. A.; Handlin, D. L.; Willis, C. L.; Kramer, E. J.; Ober, C. K. ABC Triblock Surface Active Block Copolymer with Grafted Ethoxylated Fluoroalkyl Amphiphilic Side Chains for Marine Antifouling/Fouling-Release Applications. *Langmuir* **2009,** *25* (20), 12266-12274.

13. Bodkhe, R. B.; Thompson, S. E. M.; Yehle, C.; Cilz, N.; Daniels, J.; Stafslien, S. J.; Callow, M. E.; Callow, J. A.; Webster, D. C. The effect of formulation variables on fouling-release performance of stratified siloxane-polyurethane coatings. *Journal of Coatings Technology and Research* **2012,** *9* (3), 235-249.

14. Owens, D. K.; Wendt, R. C. Estimation of Surface Free Energy of Polymers. *Journal of Applied Polymer Science* **1969,** *13* (8), 1741.

15. Owen, M. J. Surface properties of silicone release coatings. *Jocca-Surface Coatings International* **1996,** *79* (9), 400-407.

16. Gordon, G. V.; Perz, S. V.; Tabler, R. L.; Stasser, J. L.; Owen, M. J.; Tonge, J. S. Silicone release coatings: An examination of the release mechanism. *Adhesives Age* **1998,** *41* (11), 35-43.

17. Owen, M. J. Why Silicones Behave Funny. *Chemtech* **1981,** *11* (5), 288-292.

18. Kohl, J. G.; Singer, I. L.; Schwarzer, N.; Yu, V. Y. Effect of bond coat modulus on the durability of silicone duplex coatings. *Progress in Organic Coatings* **2006,** *56* (2-3), 220-226.

19. Scheirs, J. *Modern Fluoropolymers*; John Wiley and Sons Ltd.: West Sussex, England, 1997. p 637.

20. Li, X.; Andruzzi, L.; Chiellini, E.; Galli, G.; Ober, C. K.; Hexemer, A.; Kramer, E. J.; Fischer, D. A. Semifluorinated Aromatic Side-Group Polystyrene-Based Block Copolymers: Bulk Structure and Surface Orientation Studies. *Macromolecules* **2002,** *35* (21), 8078-8087.

21. Harada, K.; Koizumi, A.; Saito, N.; Inoue, K.; Yoshinaga, T.; Date, C.; Fujii, S.; Hachiya, N.; Hirosawa, I.; Koda, S.; Kusaka, Y.; Murata, K.; Omae, K.; Shimbo, S.; Takenaka, K.; Takeshita, T.; Todoriki, H.; Wada, Y.; Watanabe, T.; Ikeda, M. Historical and geographical aspects of the increasing perfluorooctanoate and perfluorooctane sulfonate contamination in human serum in Japan. *Chemosphere* **2007,** *66* (2), 293-301.

22. Clarke, B. O.; Smith, S. R. Review of 'emerging' organic contaminants in biosolids and assessment of international research priorities for the agricultural use of biosolids. *Environment International* **2010,** *37* (1), 226-247.

23. Buck, R. C.; Franklin, J.; Berger, U.; Conder, J. M.; Cousins, I. T.; de Voogt, P.; Jensen, A. A.; Kannan, K.; Mabry, S.; van Leeuwen, S. P. J. Perfluoroalkyl and Polyfluoroalkyl Substances in the Environment: Terminology, Classification, and Origins. *Integrated Environmental Assessment and Management* **2011,** *7* (4), 513–541.

24. Zushi, Y.; Hogarh, J. N.; Masunaga, S. Progress and perspective of perfluorinated compound risk assessment and management in various countries and institutes. *Clean Technologies and Environmental Policy* **2012,** *14* (1), 9-20.

25. Zheng, Y.; Wynne, K. J. Poly(bis-2,2,2-trifluoroethoxymethyl oxetane): Enhanced Surface Hydrophobicity by Crystallization and Spontaneous Asperity Formation *Langmuir* **2007,** *23* (24), 11964-11967.

26. Zheng, Y.; Zhang, W.; Gupta, M.; Kankanala, S.; Marks, C.; Carpenter, E.; Carroll, K.; Wynne, K. J. Poly(bis-2,2,2-trifluoroethoxymethyl oxetane): Multiple Crystal Phases, Crystallization-Induced Surface Topological Complexity and Enhanced Hydrophobicity. *Journal of Polymer Science Part B-Polymer Physics* **2010,** *48* (10), 1022-1034.

27. Zhang, W.; Fujiwara, T.; Taskent, H.; Zheng, Y.; Brunson, K.; Gamble, L.; Wynne, K. J. A Polyurethane Surface Modifier: Contrasting Amphiphilic and Contraphilic Surfaces Driven by Block and Random Soft Blocks Having Trifluoroethoxymethyl and PEG Side Chains. *Macromolecular Chemistry and Physics* **2012,** *213* (14), 1415–1434,.

28. Guo, J.; Resnick, P.; Efimenko, K.; Genzer, J.; DeSimone, J. M. Alternative fluoropolymers to avoid the challenges associated with perfluorooctanoic acid. *Industrial & Engineering Chemistry Research* **2008,** *47* (3), 502-508.

29. Yarbrough, J. C.; Rolland, J. P.; DeSimone, J. M.; Callow, M. E.; Finlay, J. A.; Callow, J. A. Contact Angle Analysis, Surface Dynamics, and Biofouling Characteristics of Cross-Linkable, Random Perfluoropolyether-Based Graft Terpolymers. *Macromolecules* **2006,** *39* (7), 2521-2528.

30. Thanawala, S. K.; Chaudhury, M. K. Surface modification of silicone elastomer using perfluorinated ether. *Langmuir* **2000,** *16* (3), 1256-1260.

31. Schmidt, D. L.; Brady, R. F., Jr.; Lam, K.; Schmidt, D. C.; Chaudhury, M. K. Contact Angle Hysteresis, Adhesion, and Marine Biofouling. *Langmuir* **2004,** *20* (7), 2830-2836.

32. Gao, L. C.; McCarthy, T. J. Wetting 101 degrees. *Langmuir* **2009,** *25* (24), 14105-14115.

33. Katano, Y.; Tomono, H.; Nakajima, T. Surface property of polymer films with fluoroalkyl side chains. *Macromolecules* **1994,** *27*, 2342-2344.

34. Honda, K.; Morita, M.; Otsuka, H.; Takahara, A. Molecular aggregation structure and surface properties of poly(fluoroalkyl acrylate) thin films. *Macromolecules* **2005,** *38* (13), 5699-5705.

35. Kim, J.; Chisholm, B. J.; Bahr, J. Adhesion study of silicone coatings: the interaction of thickness, modulus and shear rate on adhesion force. *Biofouling* **2007,** *23* (2), 113-120.

36. Kendall, K. The adhesion and surface energy of elastic solids. *J. Physics D Applied Physics* **1971,** *4*, 1186-1195.

37. Wynne, K. J.; Swain, G. W.; Fox, R. B.; Bullock, S.; Uilk, J. Two silicone nontoxic fouling release coatings: hydrosilation cured PDMS and CaCO3 filled, ethoxysiloxane cured RTV11. *Biofouling* **2000,** *16* (2-4), 277-288.

38. Singer, I. L.; Kohl, J. G.; Patterson, M. Mechanical aspects of silicone coatings for hard foulant control. *Biofouling* **2000,** *16* (2-4), 301-309.

39. Kohl, J. G.; Singer, I. L. Pull-off behavior of epoxy bonded to silicone duplex coatings. *Progress in Organic Coatings* **1999,** *36* (1-2), 15-20.

40. Chujo, Y.; Ihara, E.; Kure, S.; Saegusa, T. Synthesis of Triethoxysilyl-Terminated Polyoxazolines and Their Cohydrolysis Polymerization with Tetraethoxysilane. *Macromolecules* **1993,** *26* (21), 5681-5686.

41. Zhang, J. A.; Yang, J. J.; Wu, Q. Y.; Wu, M. Y.; Liu, N. N.; Jin, Z. L.; Wang, Y. F. SiO2/Polymer Hybrid Hollow Microspheres via Double in Situ Miniemulsion Polymerization. *Macromolecules* **2010,** *43* (3), 1188-1190.

42. Song, J. X.; Chen, G. X.; Ding, Y.; Shi, J. J.; Liu, Y.; Li, Q. F. Preparation and characterization of epoxy resin modified with alkoxysilane-functionalized poly(urethane-imide) by the sol-gel process. *Polymer International* **2011,** *60* (11), 1594-1599.

43. Liu, P. G.; Song, J. X.; He, L. H.; Liang, X. Q.; Ding, H. Y.; Li, Q. F. Alkoxysilane functionalized polycaprolactone/polysiloxane modified epoxy resin through sol-gel process. *European Polymer Journal* **2008,** *44* (3), 940-951.

44. Swain, G. Barnacle adhesion strengths in shear *J. Protective Coatings and Linings* **1999,** *16,* 26-33.

45. Berglin, M.; Lonn, N.; Gatenholm, P. Coating modulus and barnacle bioadhesion. *Biofouling* **2003,** *19*, 63-69.

46. Sommer, S.; Ekin, A.; Webster, D. C.; Stafslien, S. J.; Daniels, J.; VanderWal, L. J.; Thompson, S. E. M.; Callow, M. E.; Callow, J. A. A preliminary study on the properties and fouling-release performance of siloxane-polyurethane coatings prepared from poly(dimethylsiloxane) (PDMS) macromers. *Biofouling* **2010,** *26* (8), 961-972.

47. Zhang, W.; Henke, D.; Presnall, D.; Chakrabarty, S.; Wang, C.; Wynne, K. J. Liquid–Liquid Extraction of 3FOx and 5FOx Polyoxetane Diols: Impact on Polyurethane Mechanical Properties, Surface Morphology, and Wetting Behavior. *Macromolecular Chemistry and Physics* **2012,** *213* (12), 1225-1238.

48. Saegusa, T.; Chujo, Y. An Organic Inorganic Hybrid Polymer. *Journal of Macromolecular Science-Chemistry* **1990,** *A27* (13-14), 1603-1612.

49. Adachi, K.; Achimuthu, A. K.; Chujo, Y. Synthesis of organic-inorganic polymer hybrids controlled by Diels-Alder reaction. *Macromolecules* **2004,** *37* (26), 9793-9797.

50. Kurt, P.; Wynne, K. J. Co-Polyoxetanes with alkylammonium and fluorous or PEG-Like side chains: soft blocks for surface modifying polyurethanes. *Macromolecules* **2007,** *40* (26), 9537-9543.

51. Makal, U.; Uilk, J.; Kurt, P.; Cooke, R. S.; Wynne, K. J. Ring opening polymerization of 3-semifluoro- and 3-bromomethyloxetanes to poly(2,2-substituted-1,3-propylene oxide) telechelics for soft blocks in polyurethanes. *Polymer* **2005,** *46* (8), 2522-2530.

52. Shin, J.; Matsushima, H.; Chan, J. W.; Hoyle, C. E. Segmented Polythiourethane Elastomers through Sequential Thiol-Ene and Thiol-Isocyanate Reactions. *Macromolecules* **2009,** *42* (9), 3294-3301.

53. Uilk, J. M.; Mera, A. E.; Fox, R. B.; Wynne, K. J. Hydrosilation-cured poly(dimethylsiloxane) networks: Intrinsic contact angles via dynamic contact angle analysis. *Macromolecules* **2003,** *36* (10), 3689-3694.

54. Ong, M. D.; Volksen, W.; Dubois, G.; Lee, V.; Brock, P. J.; Deline, V. R.; Miller, R. D.; Dauskardt, R. H. Molecular-controlled fracture and release of templated nanoporous organosilicate thin films. *Advanced Materials (Weinheim, Germany)* **2008,** *20* (16), 3159-3164.

55. Volksen, W.; Magbitang, T. P.; Miller, R. D.; Purushothaman, S.; Cohen, S. A.; Nakagawa, H.; Nobe, Y.; Kokubo, T.; Dubois, G. J. M. A Manufacturing Grade, Porous Oxycarbosilane Spin-On Dielectric Candidate with K <= 2.0. *Journal of the Electrochemical Society* **2011,** *158* (7), G155-G161.

56. Volksen, W.; Miller, R. D.; Dubois, G. Low Dielectric Constant Materials. *Chemical Reviews (Washington, DC, United States)* **2010,** *110* (1), 56-110.

57. Tyagi, D.; Yilgor, I.; McGrath, J. E.; Wilkes, G. L. Segmented Organosiloxane Copolymers .2. Thermal and Mechanical-Properties of Siloxane Urea Copolymers. *Polymer* **1984,** *25* (12), 1807-1816.

58. Yilgor, E.; Eynur, T.; Kosak, C.; Bilgin, S.; Yilgor, I.; Malay, O.; Menceloglu, Y.; Wilkes, G. L. Fumed silica filled poly(dimethylsiloxane-urea) segmented copolymers: Preparation and properties. *Polymer* **2011,** *52* (19), 4189-4198.

59. Chakrabarty, S.; Nisenholt, M.; Wynne, K. J. PDMS-Fluorous Polyoxetane-PDMS Triblock Hybrid Elastomers: Tough and Transparent with Novel Bulk Morphologies. *Macromolecules* **2012,** *45* (19), 7900-7913.

60. Makal, U.; Fujiwara, T.; Cooke, R. S.; Wynne, K. J. Polyurethanes containing oxetane-derived poly(2,2-substituted-1,3-propylene oxide) soft blocks: copolymer effect on wetting behavior. *Langmuir* **2005,** *21* (23), 10749 -10755.

61. Yilgor, I.; Yilgor, E.; Guler, I. G.; Ward, T. C.; Wilkes, G. L. FTIR investigation of the influence of diisocyanate symmetry on the morphology development in model segmented polyurethanes. *Polymer* **2006,** *47* (11), 4105-4114.

62. Coleman, M. M.; Lee, K. H.; Skrovanek, D. J.; Painter, P. C. Hydrogen-Bonding in Polymers .4. Infrared Temperature Studies of a Simple Polyurethane. *Macromolecules* **1986,** *19* (8), 2149-2157.

63. Lamba, N. M. K.; Woodhouse, K. A.; Cooper, S. L. *Polyurethanes in Biomedical Applications*; CRC Press: Boca Raton, FL, 1998. p 15-77.

64. Harrick, N. J. *Internal Reflectance Spectroscopy*; Wiley-lnterscience: New York, 1967.

65. Skoog, D. A.; Holler, F. J.; Crouch, S. R. *Principles of Instrumental Analysis*; 6th ed.; Thompson Higher Education2007. p p 472.

66. Bergbreiter, D. E.; Srinivas, B. Surface selectivity in blending polyethylene poly(ethylene glycol) block cooligomers into high-density polyethylene. . *Macromolecules* **1992,** *25* (2), 636-643.

67. Schmidt, J. J.; Gardella, J. A.; Salvati, L. Surface studies of polymer blends. 2. An ESCA and IR study of poly(methyl methacrylate) / poly(vinyl chloride homopolymer blends. *Macromolecules* **1989,** *22* (12), 4489-4495.

68. Sato, Y.; Ootsubo, M.; Yamamoto, G.; Van Lier, G.; Terrones, M.; Hashiguchi, S.; Kimura, H.; Okubo, A.; Motomiya, K.; Jeyadevan, B.; Hashida, T.; Tohji, K. Super-robust, lightweight, conducting carbon nanotube blocks cross-linked by de-fluorination. *ACS Nano* **2008,** *2* (2), 348-356.

69. Moore, W. H.; Krimm, S. Vibrational Analysis of Peptides, Polypeptides, and Proteins. I. Polyglycine I. *Biopolymers* **1976,** *15,* 2439-2464.

70. Bar, G.; Thomann, Y.; Whangbo, M. H. Characterization of the morphologies and nanostructures of blends of poly(styrene) block-poly(ethene-co-but-1-ene)-block-poly(styrene) with isotactic and atactic polypropylenes by tapping-mode atomic force microscopy. *Langmuir* **1998,** *14* (5), 1219-1226.

71. Bar, G.; Thomann, Y.; Brandsch, R.; Cantow, H. J.; Whangbo, M. H. Factors affecting the height and phase images in tapping mode atomic force microscopy. Study of phase-separated

polymer blends of poly(ethene-co-styrene) and poly(2,6-dimethyl-1,4-phenylene oxide). *Langmuir* **1997,** *13* (14), 3807-3812.

72. Magonov, S. N.; Elings, V.; Whangbo, M. H. Phase imaging and stiffness in tapping-mode atomic force microscopy. *Surface Science* **1997,** *375* (2-3), L385-L391.

73. Garrett, J. T.; Runt, J.; Lin, J. S. Microphase separation of segmented poly(urethane urea) block copolymers. *Macromolecules* **2000,** *33* (17), 6353-6359.

74. Fujiwara, T.; Wynne, K. J. Contrasting nanoscale surface morphologies of polyurethanes containing polyoxetane soft blocks with random and block segmer sequences. *Macromolecules* **2004,** *37* (23), 8491-8494.

75. Wynne, K. J.; Makal, U.; Kurt, P.; Gamble, L. Model fluorous polyurethane surface modifiers having co-polyoxetane soft blocks with trifluoroethoxymethyl and bromomethyl side chains. *Langmuir* **2007,** *23* (21), 10573-10580.

76. Pike, J. K.; Ho, T.; Wynne, K. J. Water-induced surface rearrangements of poly(dimethylsiloxane- urea-urethane) segmented block copolymers. *Chemistry of Materials* **1996,** *8* (4), 856-860.

77. Kavanagh, C. J.; Schultz, M. P.; Swain, G. W.; Stein, J.; Truby, K.; Wood, C. D. Variation in adhesion strength of Balanus eburneus, Crassostrea virginica and Hydroides dianthus to fouling-release coatings. *Biofouling* **2001,** *17* (2), 155-167.

78. Kumar, A.; Gupta, R. K. *Fundamentals of Polymer Engineering*; Marcel Dekker: New York, 2003.

79. Xie, L. Y.; Hong, F.; He, C. X.; Liu, J. H.; Wu, C. Fouling-release Property of Water-filled Porous Elastomers. *Chinese Journal of Chemical Physics* **2012,** *25* (3), 330-334.

80. Mapkar, J. A. Effect of Elastomer Functionalized Carbon Nanofibers on the Properties of Polyimide Nanocomposite and Polydimethylsiloxane-carbon Nanofiber Sheets. Ph. D. Thesis, University of Toledo2008.

81. Kaffashi, A.; Jannesari, A.; Ranjbar, Z. Silicone fouling-release coatings: effects of the molecular weight of poly(dimethylsiloxane) and tetraethyl orthosilicate on the magnitude of pseudobarnacle adhesion strength. *Biofouling* **2012,** *28* (7), 729-741.

82. McClain, M. A.; Clements, I. P.; Shafer, R. H.; Bellamkonda, R. V.; LaPlaca, M. C.; Allen, M. G. Highly-compliant, microcable neuroelectrodes fabricated from thin-film gold and PDMS. *Biomedical Microdevices* **2011,** *13* (2), 361-373.

83. Jellinek, H. H. G.; Kachi, H.; Kittaka, S.; Lee, M.; Yokota, R. Ice releasing block-copolymer coatings. *Colloid and Polymer Science* **1978,** *256* (6), 544-51.

84. Andrews, E. H.; Majid, H. A.; Lockington, N. A. Adhesion of Ice to a Flexible Substrate. *Journal of Materials Science* **1984,** *19* (1), 73-81.

85. Croutch, V. K.; Hartley, R. A. Adhesion of ice to coatings and the performance of ice release coatings. *Journal of Coatings Technology* **1992,** *64* (815), 41-53.

86. Kulinich, S. A.; Farzaneh, M. How Wetting Hysteresis Influences Ice Adhesion Strength on Superhydrophobic Surfaces. *Langmuir* **2009,** *25* (16), 8854-8856.

87. Farhadi, S.; Farzaneh, M.; Kulinich, S. A. Anti-icing performance of superhydrophobic surfaces. *Applied Surface Science* **2011,** *257* (14), 6264-6269.

88. Yorkgitis, E. M.; Melancon, K. C.; Hine, A. M.; Giaquinto, S. M. Glaciphobic Polymeric Materials. *Journal of Adhesion Science and Technology* **2012,** *26* (4-5), 681-699.

89. Palacios, J. L.; Han, Y.; Brouwers, E. W.; Smith, E. C. Icing Environment Rotor Test Stand Liquid Water Content Measurement Procedures and Ice Shape Correlation. *Journal of the American Helicopter Society* **2012,** *57* (2).

90. Palacios, A. M.; Palacios, J. L.; Sanchez, L. Eliciting a human understandable model of ice adhesion strength for rotor blade leading edge materials from uncertain experimental data. *Expert Systems with Applications* **2012,** *39* (11), 10212-10225.

91. Andrews, E. H.; Lockington, N. A. The Cohesive and Adhesive Strength of Ice. *Journal of Materials Science* **1983,** *18* (5), 1455-1465.

92. Wynne, K. J.; Zhang, W. Fixtures for ice adhesion testing. US Patent USSN 61/775,766, March 11, 2013, 2013.

93. Boumbimba, R. M.; Ahzi, S.; Bahlouli, N.; Ruch, D.; Gracio, J. Dynamic Mechanical Properties of PMMA/Organoclay Nanocomposite: Experiments and Modeling. *Journal of Engineering Materials and Technology* **2011,** *133* (3), 030908-030908.

94. Menini, R.; Farzaneh, M. Advanced Icephobic Coatings. *Journal of Adhesion Science and Technology* **2011,** *25* (9), 971-992.

95. Dodiuk, H.; Kenig, S.; Dotan, A. Do Self-cleaning Surfaces Repel Ice? *Journal of Adhesion Science and Technology* **2012,** *26* (4-5), 701-714.

96. Raraty, L. E.; Tabor, D. The adhesion and strength properties of ice. *Proc. Roy. Soc.* **1958,** *A245*, 184-201.

97. Bascom, W. D.; Cottington, R. L.; Singleterry, C. R. Ice adhesion to hydrophilic and hydrophobic surfaces. *Journal of Adhesion* **1969,** (Oct.), 246-63.

98. Murase, H.; Nanishi, K. On the relationship of thermodynamic and physical properties of polymers with ice adhesion. *Ann. Glaciol.* **1985,** *6*, 146-9.

99. Saito, H.; Takai, K.; Yamauchi, G. Water-and ice-repellent coatings. *Surface Coatings International* **1997,** *80* (4), 168-171.

100. Petrenko, V. F.; Peng, S. Reduction of ice adhesion to metal by using self-assembling monolayers (SAMs). *Canadian Journal of Physics* **2003,** *81* (1/2), 387-393.

101. Zou, M.; Beckford, S.; Wei, R.; Ellis, C.; Hatton, G.; Miller, M. A. Effects of surface roughness and energy on ice adhesion strength. *Appl. Surf. Sci.* **2011,** *257* (8), 3786-3792.

102. Luan, B. Q.; Robbins, M. O. The breakdown of continuum models for mechanical contacts. *Nature* **2005,** *435* (7044), 929-932.

103. Persson, B. N. J.; Albohr, O.; Tartaglino, U.; Volokitin, A. I.; Tosatti, E. On the nature of surface roughness with application to contact mechanics, sealing, rubber friction and adhesion. *Journal of Physics-Condensed Matter* **2005,** *17* (1), R1-R62.

104. Mo, Y. F.; Turner, K. T.; Szlufarska, I. Friction laws at the nanoscale. *Nature* **2009,** *457* (7233), 1116-1119.

105. Tas, N.; Sonnenberg, T.; Jansen, H.; Legtenberg, R.; Elwenspoek, M. Stiction in surface micromachining. *Journal of Micromechanics and Microengineering* **1996,** *6* (4), 385-397.

106. Bruinsma, G. M.; van der Mei, H. C.; Busscher, H. J. Bacterial adhesion to surface hydrophilic and hydrophobic contact lenses. *Biomaterials* **2001,** *22* (24), 3217-3224.

107. Pang, H.; Zhou, S.; Gu, G.; Wu, L. Long-term hydrophobicity and ice adhesion strength of latex paints containing silicone oil microcapsules. *J. Adhes. Sci. Technol.* **2013,** *27* (1), 46-57.

108. Susoff, M.; Siegmann, K.; Pfaffenroth, C.; Hirayama, M. Evaluation of icephobic coatings-Screening of different coatings and influence of roughness. *Appl. Surf. Sci.* **2013,** *282,* 870-879.

109. Oner, D.; McCarthy, T. J. Ultrahydrophobic surfaces. Effects of topography length scales on wettability. *Langmuir* **2000,** *16* (20), 7777-7782.

110. Lampin, M.; WarocquierClerout, R.; Legris, C.; Degrange, M.; SigotLuizard, M. F. Correlation between substratum roughness and wettability, cell adhesion, and cell migration. *Journal of Biomedical Materials Research* **1997,** *36* (1), 99-108.

111. Jung, Y. C.; Bhushan, B. Contact angle, adhesion and friction properties of micro- and nanopatterned polymers for superhydrophobicity. *Nanotechnology* **2006,** *17* (19), 4970-4980.

112. Erbil, H. Y.; McHale, G.; Rowan, S. M.; Newton, M. I. Determination of the receding contact angle of sessile drops on polymer surfaces by evaporation. *Langmuir* **1999,** *15* (21), 7378-7385.

113. Chen, J.; Liu, J.; He, M.; Li, K.; Cui, D.; Zhang, Q.; Zeng, X.; Zhang, Y.; Wang, J.; Song, Y. Superhydrophobic surfaces cannot reduce ice adhesion. *Appl. Phys. Lett.* **2012,** *101* (11), 111603/1-111603/3.

114. Zhang, S.-t.; Wang, H.; Wang, L. Progress in Ice-phobic Coating. *Adv. Mater. Res.* **2012,** *399-401*, 2044-2048.

115. Arianpour, F.; Farzaneh, M.; Kulinich, S. A. Hydrophobic and ice-retarding properties of doped silicone rubber coatings. *Applied Surface Science* **2013,** *265*, 546-552.

116. Chung, J. Y.; Chaudhury, M. K. Soft and Hard Adhesion. *The Journal of Adhesion* **2005,** *81* (10-11), 1119.

117. Liu, Z.; Deshazer, H.; Rice, A. J.; Chen, K.; Zhou, C.; Kallenbach, N. R. Multivalent Antimicrobial Peptides from a Reactive Polymer Scaffold. *Journal of Medicinal Chemistry* **2006,** *49* (12), 3436-3439.

118. Ghatak, A.; Mahadevan, L.; Chaudhury, M. K. Measuring the work of adhesion between a soft confined film and a flexible plate. *Langmuir* **2005,** *21* (4), 1277-1281.

119. Liu, R. Y. F.; Bernal-Lara, T. E.; Hiltner, A.; Baer, E. Polymer Interphase Materials by Forced Assembly. *Macromolecules* **2005,** *38* (11), 4819-4827.

120. Croutch, V. K.; Hartley, R. A. Adhesion of ice to coatings and the performance of ice release coatings. *Journal of Coatings Technology* **1992,** *64* (815), 41-53.

121. Yorkgitis, E. M.; Melancon, K. C.; Hine, A. M.; Giaquinto, S. M. Glaciophobic polymeric materials. *Journal of Adhesion Science and Technology* **2012,** *26* (4-5), 681-699.

122. Yang, S.; Xia, Q.; Zhu, L.; Xue, J.; Wang, Q.; Chen, Q.-m. Research on the ice-phobic properties of fluoropolymer-based materials. *Applied Surface Science* **2011,** *257* (11), 4956-4962.

123. Palacios, J. L.; Han, Y.; Brouwers, E. W.; Smith, E. C. Icing Environment Rotor Test Stand Liquid Water Content Measurement Procedures and Ice Shape Correlation. *Journal of the American Helicopter Society* **2012,** *57* (2), 12.

124. Wang, C.; Zhang, W.; Siva, A.; Tiea, D.; Wynne, K. J. Laboratory Test for Ice Adhesion Strength Using Commercial Instrumentation. *Langmuir* **2014,** *30* (2), 540-547.

125. Petit, J.; Bonaccurso, E. General Frost Growth Mechanism on Solid Substrates with Different Stiffness. *Langmuir* **2014,** *30* (4), 1160-1168.

126. Kroner, E.; Maboudian, R.; Arzt, E. Adhesion Characteristics of PDMS Surfaces During Repeated Pull-Off Force Measurements. *Advanced Engineering Materials* **2010,** *12* (5), 398-404.

127. Wendt, D. E.; Kowalke, G. L.; Kim, J.; Singer, I. L. Factors that influence elastomeric coating performance: the effect of coating thickness on basal plate morphology, growth and critical removal stress of the barnacle Balanus amphitrite. *Biofouling* **2006,** *22* (1), 1-9.

128. Jiong, L.; Chaudhury, M. K.; Berry, D. H.; Seebergh, J. E.; Osborne, J. H.; Blohowiak, K. Y. Fracture behavior of an epoxy/aluminum interface reinforced by sol–gel coatings. *Journal of Adhesion Science and Technology* **2006,** *20* (4), 277-305.

129. Yang, L.; Qiu, S.; Zhang, Y.; Xu, Y. Preparation of PDMS/SiO2 nanocomposites via ultrasonical modification and miniemulsion polymerization. *Journal of Polymer Research* **2012,** *20* (1), 1-6.

130. Luo, X.; Mather, P. T. Preparation and Characterization of Shape Memory Elastomeric Composites. *Macromolecules* **2009,** *42* (19), 7251-7253.

131. Schulson, E. M. The structure and mechanical behavior of ice. *JOM* **1999,** *51* (2), 21.

132. Dotan, A.; Dodiuk, H.; Laforte, C.; Kenig, S. The Relationship between WaterWetting and Ice Adhesion. *Journal of Adhesion Science and Technology* **2009,** *23*, 1907-1915.

133. Chen, J.; Liu, J.; He, M.; Li, K. Y.; Cui, D. P.; Zhang, Q. L.; Zeng, X. P.; Zhang, Y. F.; Wang, J. J.; Song, Y. L. Superhydrophobic surfaces cannot reduce ice adhesion. *Applied Physics Letters* **2012,** *101* (11).

134. Zhang, W.; Chakrabarty, S.; Wynne, K. J. In *Ice-phobic coatings: New theory, new laboratory test, and new hybrid fluorous polyoxetane systems*, 2012; American Chemical Society, pp POLY-25.

135. Chung, J. Y.; Chaudhury, M. K. Soft and Hard Adhesion. *Journal of Adhesion* **2005,** *81* (10-11), 1119.

136. Liu, J.; Chaudhury, M. K.; Berry, D. H.; Seebergh, J. E.; Osborne, J. H.; Blohowiak, K. Y. Fracture behavior of an epoxy/aluminum interface reinforced by sol–gel coatings. *Journal of Adhesion Science and Technology* **2006,** *20* (4), 277-305.

137. Chaudhury, M. K. Adhesion and fracture at soft interfaces. *Proc. Annu. Meet. Adhes. Soc.* **2005,** *28th*, 8.

138. Liu, J.; Chaudhury, M. K.; Berry, D. H.; Seebergh, J. E.; Osborne, J. H.; Blohowiak, K. Y. Effect of surface morphology on the crack growth along aluminum-epoxy interfaces. *Proc. Annu. Meet. Adhes. Soc.* **2005,** *28th*, 387-388.

139. Eisenberg, D.; Kauzmann, W. *The Structure Properties of Water*; Oxford University Press: Oxford, 1969.

140. Reinert, F.; Lüthy, W. Thermo-optically driven adaptive mirror based on thermal expansion: preparation and resolution. *Optics Express* **2005,** *13* (26), 10749-10753.

141. Esposito, M.; Buontempo, S.; Petriccione, A.; Zarrelli, M.; Breglio, G.; Saccomanno, A.; Szillasi, Z.; Makovec, A.; Cusano, A.; Chiuchiolo, A.; Bajko, M.; Giordano, M. Fiber Bragg Grating sensors to measure the coefficient of thermal expansion of polymers at cryogenic temperatures. *Sensors and Actuators A: Physical* **2013,** *189* (0), 195-203.

142. Chernyy, S.; Järn, M.; Shimizu, K.; Swerin, A.; Pedersen, S. U.; Daasbjerg, K.; Makkonen, L.; Claesson, P.; Iruthayaraj, J. Superhydrophilic Polyelectrolyte Brush Layers with Imparted Anti-Icing Properties: Effect of Counter ions. *ACS Applied Materials & Interfaces* **2014**.

# VITA

Chenyu Wang was born on March 17, 1986 in Nanjing, China. He graduated from High School Affiliated to Nanjing Normal University, China, in 2004. He received his Bachelor of Science in Biological Engineering from Nanjing University of Science and Technology, China in 2008. He received his Master of Science in Chemical and Life Science Engineering from Virginia Commonwealth University, USA in 2011.

## Publications

1. **Wang, C.**; Zhang, W.; Siva, A.; Tiea, D.; Wynne, K. J., Laboratory Test for Ice Adhesion Strength Using Commercial Instrumentation. *Langmuir* **2014,** *30* (2), 540-547.

2. Chakrabarty, S.; **Wang, C.**; Zhang, W.; Wynne, K. J., Rigid Adherent-Resistant Elastomers (RARE): Nano-, Meso-, and Microscale Tuning of Hybrid Fluorous Polyoxetane-Polyurethane Blend Coatings. *Macromolecules* **2013,** *46* (8), 2984-2996.

3. **Wang, C.**; Zhang, W.; Wynne, K. J., Hybrid networks incorporating fluorous polyoxetane soft blocks. *Applied Organometallic Chemistry* **2013,** *27* (11), 660-665.

4. **Wang, C.**; Zhang, W.; Wynne, K. J., Nanoscale versus Microscale Gelation for Crosslinked Polyurethanes. *Macromolecular Symposia* **2013,** *325-326* (1), 168-176.

5. Zhang, W.; Henke, D.; Presnall, D.; Chakrabarty, S.; **Wang, C.**; Wynne, K. J., Liquid–Liquid Extraction of 3FOx and 5FOx Polyoxetane Diols: Impact on Polyurethane Mechanical Properties, Surface Morphology, and Wetting Behavior. *Macromolecular Chemistry and Physics* **2012,** *213* (12), 1225-1238.

## Patents.

1. Wynne, K. J.; Zhang, W.; **Wang, C.**; Chakrabarty, S. Abhesive hybrid coatings, coating compositions, their manufacture and article. WO2013016594A2, 2013.